NONLINEAR DYNAMIC RESPONSE AND STABILITY ANALYSIS OF ELECTRO-MAGNETO-ACTIVE CIRCULAR MEMBRANES

Ph.D. Thesis

By

Ankush Agrawal



DEPARTMENT OF MECHANICAL ENGINEERING
INDIAN INSTITUTE OF TECHNOLOGY INDORE
JULY 2026

NONLINEAR DYNAMIC RESPONSE AND STABILITY ANALYSIS OF ELECTRO-MAGNETO-ACTIVE CIRCULAR MEMBRANES

A THESIS

Submitted in fulfillment of the
requirements for the award of the degree
of

DOCTOR OF PHILOSOPHY

by

Ankush Agrawal

DEPARTMENT OF MECHANICAL ENGINEERING
INDIAN INSTITUTE OF TECHNOLOGY INDORE
JULY 2026

INDIAN INSTITUTE OF TECHNOLOGY INDORE

I hereby certify that the work which is being presented in the thesis entitled **"Nonlinear Dynamic Response and Stability Analysis of Electro-Magneto-Active Circular Membranes"** in partial fulfillment of the requirements for the award of the degree of **DOCTOR OF PHILOSOPHY** and submitted in the **DEPARTMENT OF MECHANICAL ENGINEERING, INDIAN INSTITUTE OF TECHNOLOGY INDORE**, is an authentic record of my own work carried out during the period from J**anuary 2024 to July 2026** under the supervision of **Dr. Aman Khurana, Assistant Professor, Department of Mechanical Engineering, Indian Institute of Technology Indore.**

The matter presented in this thesis has not been submitted by me for the award of any other degree of this or any other institute.

Ankush Agrawal
28/10/26

Signature of the Student with date:
(Ankush Agrawal)

This is to certify that the above statement made by the candidate is correct to the best of my knowledge.

28/10/26

Signature of the Thesis Supervisor with date:
(Dr. Aman Khurana)

Mr. Ankush Agrawal has successfully completed his Ph.D. oral examination held on **22nd June 2026.**

28/10/26

Signature of Thesis Supervisor with date:
(Dr. Aman Khurana)

ACKNOWLEDGEMENT

First and foremost, I would like to express my heartfelt gratitude to my thesis supervisor, **Dr. Aman Khurana**, Assistant Professor, Department of Mechanical Engineering, IIT Indore. His exceptional guidance, unwavering support, and insightful suggestions have been invaluable throughout my research journey. His encouragement and clarity of thought have greatly influenced both the direction and quality of this work. I feel truly fortunate to have had the opportunity to learn from his expertise and mentorship.

I am sincerely thankful to **Dr. Suhas S. Joshi**, Director, IIT Indore, and **Dr. Anand Parey**, Head of the Department of Mechanical Engineering, for their encouragement and for providing the academic environment and resources necessary to carry out this research.

I would also like to extend my sincere appreciation to my PSPC members, **Dr. Indrasen Singh**, Associate Professor, Department of Mechanical Engineering, and **Dr. Khushubo Devi**, Assistant Professor, MEMS Department, for their constructive feedback, thoughtful discussions, and continuous guidance, which have significantly strengthened this research.

My sincere thanks go to **Dr. S. Janakiraman**, DPGC Coordinator and Assistant Professor in the Department of Mechanical Engineering, for his consistent evaluation, valuable guidance, and generous support throughout the program.

I am grateful to **Dr. Deepak Kumar** at MANIT Bhopal, who served as an external examiner during my JRF-to-SRF conversion, for his mentorship, encouragement, and continuous support. His insights and positive guidance have contributed meaningfully to both my academic progress and personal growth.

I express my heartfelt gratitude to my esteemed Ph.D. viva-voce examiner, **Dr. Rajeev Kumar**, Professor, School of Mechanical and Materials Engineering, IIT Mandi, for his expert evaluation, thoughtful insights, and constructive feedback, which greatly enhanced the depth and quality of this research work.

I would also like to thank my fellow research scholars at IIT Indore, including

Dr. Suraj Kumar and **Mr. Keshav Purviya**, as well as **Dr. Virat Singh Chauhan** at CSIR Roorkee and **Dr. Sankalp Gour**, Postdoctoral Fellow at IIT Kharagpur, for their friendship, valuable discussions, and constant encouragement. Their companionship made this journey more enriching and motivating.

Above all, I am deeply indebted to my parents, **Mr. Naresh Kumar Agrawal** and **Mrs. Anita Agrawal**, whose sacrifices, unconditional love, and unwavering belief in me have been the true foundation of my achievements. Their support has been my greatest strength throughout this journey.

Finally, I extend my sincere thanks to everyone who has contributed, directly or indirectly, through their guidance, encouragement, and inspiration. This journey would not have been possible without the collective support of so many individuals.

Ankush Agrawal

ABSTRACT

Electro-magneto-active membranes (EMAMs) represent a promising class of soft active materials capable of undergoing large deformations in response to coupled electrical and magnetic stimuli. Their unique ability to combine flexibility with multifunctional actuation has attracted significant attention for applications in soft robotics, biomedical devices, adaptive structures, and smart actuators. Despite these advantages, a comprehensive understanding of their nonlinear dynamic behavior and stability under coupled electro-magneto-mechanical loading remains limited. This thesis addresses this challenge by developing continuum mechanics-based models within the framework of the Gent hyperelastic constitutive theory to investigate the dynamic response and stability of reinforced electro-magneto-active circular membranes.

The study first examines the influence of particle reinforcement on the dynamic behavior of EMAMs. The effects of filler volume fraction, shear modulus ratio, electric field, and magnetic field are systematically investigated under both DC and AC loading conditions. Time-history responses, phase portraits, Poincaré maps, and frequency-response analyses are employed to characterize periodic, quasi-periodic, and chaotic oscillations. The results show that increasing particle reinforcement enhances the membrane stiffness, suppresses oscillation amplitudes, shifts the resonance frequency, and significantly improves the overall dynamic stability.

The analysis is then extended by incorporating stretch-dependent electromagnetic properties through constant, linear, and nonlinear models of electrical permittivity and magnetic permeability. Unlike the conventional constant-property assumption, the nonlinear model captures the strong influence of deformation on the electromagnetic response of the membrane. The numerical investigations demonstrate that stretch-dependent material properties substantially modify the resonance characteristics, oscillation amplitudes, beating phenomena, and stability boundaries under both DC and AC excitations.

To investigate field-induced instabilities, a continuum framework based on taut domain analysis is developed for particle-reinforced membranes. The proposed model

predicts the critical conditions associated with pull-in and wrinkling instabilities and provides a systematic description of the stability regions in the principal stretch space. The results reveal that electric and magnetic fields, filler volume fraction, and reinforcement stiffness strongly influence the evolution of the taut domain and the critical actuation limits. The corresponding stress-stretch characteristics further explain the mechanisms governing local and global stability.

The final part of the thesis investigates snap-through instability and bifurcation in fiber-reinforced active membranes by incorporating isotropic and anisotropic growth together with fiber orientation effects. The combined influence of growth, anisotropy, fiber orientation, and applied electric field on equilibrium configurations, natural frequencies, and stability is examined. The results demonstrate that fiber reinforcement and anisotropic growth significantly alter the critical actuation voltage and can transform the membrane response from bistable to monostable behavior.

Overall, this thesis presents a unified continuum mechanics framework for analyzing the nonlinear dynamics and stability of reinforced electro-magneto-active circular membranes. The developed models provide new insights into the roles of particle reinforcement, stretch-dependent electromagnetic properties, taut domain evolution, and fiber-induced anisotropy in governing the mechanical response of soft active membranes. The findings contribute to the fundamental understanding of electro-magneto-active materials and offer useful design guidelines for the development of reliable soft actuators, adaptive structures, and multifunctional smart material systems.

Keywords: Constitutive modeling, Mechanics of soft materials, Soft active materials, Particle reinforcement, Fiber reinforcement, Stability, Continuum mechanics, Hyperelasticity, Isotropic and anisotropic growth, Fiber orientation, Dielectric elastomer, Electro-magneto-active membranes.

List of Publications

Publications from the Ph.D. Thesis Work

Journal Articles

J1. **Ankush Agrawal** and Aman Khurana, "Unveiling the dynamics of particle-reinforced electro-magneto-active circular membrane," ***International Journal of Non-Linear Mechanics***, Elsevier, vol. 174, pp. 105064, 2025.
DOI: https://doi.org/10.1016/j.ijnonlinmec.2025.105064

J2. **Ankush Agrawal** and Aman Khurana, "Stretch-dependent electromagnetic properties of circular membrane: A dynamic analysis," ***International Journal of Solids and Structures***, Elsevier, vol. 324, pp. 113654, 2025.
DOI: https://doi.org/10.1016/j.ijsolstr.2025.113654

J3. **Ankush Agrawal** and Aman Khurana, "Taut domains in particle-reinforced electro-magneto-active thin circular membrane," ***Journal of Applied Mechanics***, ASME, vol. 92, pp. 111002, 2025.
DOI: https://doi.org/10.1115/1.4068963

J4. **Ankush Agrawal**, Aman Khurana, and Deepak Kumar, "Dynamics of an electric field vulnerable morpho-elastic biological membranes," ***Journal of Applied Mechanics***, ASME, vol. 92, pp. 041006, 2025.
DOI: https://doi.org/10.1115/1.4067571

J5. **Ankush Agrawal**, Nitish Kumar, Pavan Kumar Kankar, and Aman Khurana, "Coupled thermo–electro–mechanical nonlinear dynamic analysis of anisotropic visco-hyperelastic DEMES actuators," ***European Journal of Mechanics - A/Solids***, vol. 120, pp. 106208, 2026.
DOI: https://doi.org/10.1016/j.euromechsol.2026.106208.

Conference Proceedings (Scopus-indexed)

C1. **Ankush Agrawal**, Keshav Purviya, Umesh Kumar Singh, Shailesh Kundalwal, and Aman Khurana, "Electro-magneto-elastic dynamics of anisotropic circular membrane," ***ICAMCFD 2026***, Paper ID: 87, 2026.

Table of Contents

Abstract **i**

List of Figures **ix**

List of Tables **xiii**

List of Symbols **xv**

List of Abbreviations **xvii**

1 Introduction **1**

1.1 Elastomers 1

1.2 Soft active materials: electroactive, magnetoactive, and electro-magneto-active materials 2

1.3 Hyperelasticity 5

1.3.1 Deformation gradient tensor 7

1.3.2 Significance of stretch invariants 8

1.3.3 Strain energy density function 9

1.3.4 Stresses 11

1.4 Reinforcement in elastomers 14

1.4.1 Particle reinforcement 14

1.4.2 Fiber reinforcement 15

1.4.3 Impact of reinforcement on failure modeling of elastomers . . . 16

1.5 Stretch-dependent electromagnetic effects 18

1.6 Taut domains and field-induced instabilities 20
1.7 Stability issues: pull-in, snap-through, bifurcation, and dynamic instability 22
1.8 Motivation of the thesis 24
1.9 Organization of the thesis 26

2 Literature Survey **29**
2.1 Literature review 29
2.1.1 Dynamics of particle-reinforced EMAMs 30
2.1.2 Stretch-dependent electromagnetic properties and dynamic response 30
2.1.3 Taut domain formation in particle-reinforced EMAMs 32
2.1.4 Stability and field-induced instabilities in biological membranes 33
2.2 Literature gap 34
2.2.1 Dynamics of particle-reinforced EMAMs 34
2.2.2 Stretch-dependent electromagnetic properties and dynamic response 36
2.2.3 Taut domain formation in particle-reinforced EMAMs 36
2.2.4 Stability and field-induced instabilities in biological membranes 37
2.3 Research objectives 37

3 Dynamics of Particle-Reinforced Circular EMAMs **39**
3.1 Introduction 39
3.2 Mathematical formulation 41
3.2.1 Assumptions 41
3.3 Governing equation 44
3.3.1 Numerical solution procedure 48
3.4 DC dynamic response 49
3.5 Chaotic behavior on enhancing field and particle content 53
3.6 Summary 58

4 Stretch-Dependent Electromagnetic Properties and Dynamic Response 60

4.1 Introduction . . . 60

4.2 Mathematical formulation . . . 61

4.3 Governing equation . . . 64

4.3.1 Governing equation of the stretch-dependent electric permittivity 66

4.3.2 Governing equation of the stretch-dependent magnetic permeability . . . 71

4.3.3 Numerical solution procedure . . . 74

4.4 DC dynamic response of different models of permittivity and permeability . . . 75

4.5 AC dynamic response of different models of permittivity and permeability 78

4.6 Summary . . . 83

5 Taut Domain Formation in Particle-Reinforced EMAMs 85

5.1 Introduction . . . 85

5.2 Mathematical formulation . . . 86

5.3 Governing equation . . . 89

5.4 Taut domains in a smart circular membrane . . . 92

5.5 Results and discussion . . . 93

5.5.1 Effect of electric and magnetic fields on the taut domain . . . 93

5.5.2 Effect of filler volume fraction and shear modulus ratio on the taut domain . . . 96

5.6 Summary . . . 99

6 Stability and Field-Induced Instabilities in Biological Membranes 101

6.1 Introduction . . . 101

6.2 Mathematical formulation . . . 102

6.3 Governing equation . . . 106

6.4 Snap-through instability and bifurcation criterion for isotropic and anisotropic growth . . . 109

6.5 Limitations of the biological membrane model 115
6.6 Summary 116

7 Conclusion and Future Scope **118**

7.1 Conclusion 118
7.2 Future scope 120

A **121**

A.1 AC dynamic response 121

List of Figures

1.1 A schematic representation of an electro-magneto-active filler-reinforced elastomeric material undergoing deformation. 15
1.2 A schematic representation of the taut and wrinkled region [1]. 21

3.1 Schematic representation of the circular membrane: (a) Initial or reference state, (b) Deformed or actuated state caused by a radial load P and a uniformly applied transverse pressure P_t, and (c) Equivalent deformed state as in (b), achieved due to the application of a radial load, along with transverse electric and magnetic fields. 42
3.2 DC dynamic responses of the membrane with (a-b) time evolution diagrams, and (c-d) phase diagrams for the different amounts of filler (Φ), and shear modulus ratio (μ_f/μ_m). 50
3.3 DC dynamic responses of the membrane with (a) time evolution diagrams, and (b) phase diagrams for different levels of normalized stress (S). 51
3.4 DC dynamic responses of the membrane with (a–b) time evolution diagrams, and (c-d) phase diagrams for different levels of applied dimensionless voltage (V), and magnetic flux (M). 52
3.5 AC dynamic responses of the membrane with (a–b) phase diagrams merged with Poincaré plots, and (c-d) time-history plots at the excitation frequency, $\omega = 0.50$ for different voltages at V = 0.4 and 0.6. 55

3.6 AC dynamic chaotic responses of the membrane with (a–b) phase diagrams merged with Poincaré plots, and (c-d) time evolution diagrams corresponding to the excitation frequency, $\omega = 0.50$ and voltage, $V = 0.4$ for different amounts of filler at $\Phi = 0.2$ to 0.01. 56

4.1 Schematic representation of the circular membrane: (a) Initial or reference state, (b) Deformed or actuated state caused by a radial load P and a uniformly applied transverse pressure P_t, and (c) Equivalent deformed state as in (b), achieved due to the application of a radial load, along with transverse electric and magnetic fields. 62

4.2 DC dynamic responses of the membrane with (a–b) time evolution diagrams, (c-d) phase diagrams for different models (constant, linear, and nonlinear) of permittivity and permeability at $V = M = 0.25$ with $J_m = 20$ and $S = 1$. 76

4.3 DC dynamic responses of the membrane with (a–b) time evolution diagrams, (c-d) phase diagrams for different models (constant, linear, and nonlinear) of permittivity at $V = 1$, $M = 0.25$ and permeability at $V = 0.25$, $M = 1$. . 77

4.4 Variation of stretch amplitude with the applied excitation frequency for different models of (a, b) electric permittivity at $V = 0.25$ and 1.0 and (c, d) magnetic permeability at $M = 0.25$ and 1.0. 79

4.5 AC dynamic responses of the membrane with (a–c) phase diagrams merged with Poincaré plots, (d–f) time evolution diagrams corresponding to the resonant excitation frequencies for different models of electric permittivity. 80

4.6 AC dynamic responses of the membrane with (a–c) phase diagrams merged with Poincaré plots, (d–f) time evolution diagrams corresponding to the resonant excitation frequencies for different models of magnetic permeability. 82

5.1 Schematic representation of the circular membrane: (a) Initial or reference state, (b) Deformed or actuated state caused by a uniformly applied transverse pressure P_t, and (c) Equivalent deformed state as in (b), achieved due to the transverse electric and magnetic fields. 87

5.2 A schematic representation of the natural strain curves of the tensile stretch region. 92

5.3 Taut domains of the smart circular membrane for (a) varying electric field V at $M = 0.25$, and (b) varying magnetic field M at $V = 0.50$, with $\Phi = 0.05$, $\mu_f/\mu_m = 10$ and $J_m = 97.2$. Empty circles indicate equibiaxial equilibrium solutions that satisfy the stability criterion (Eq. 5.16), while blue-filled circles denote solutions that fail to meet this criterion. 95

5.4 Stress-stretch plots of the smart circular membrane for (a) varying electric field V at $M = 0.25$, and (b) varying magnetic field M at $V = 0.50$, with $\Phi = 0.05$, $\mu_f/\mu_m = 10$ and $J_m = 97.2$. 95

5.5 Taut domains of the smart circular membrane for (a) varying amounts of filler Φ, and (b) varying shear modulus ratio μ_f/μ_m under electromagnetic loading conditions ($V = 0.50$, $M = 0.50$) with $J_m = 97.2$. . . 96

5.6 Critical normalized voltage $V_{critical}$ of the smart circular membrane for varying amounts of fillers Φ, and varying shear modulus ratio μ_f/μ_m excited by a magnetic flux of $M = 0.50$ with $J_m = 97.2$. 98

5.7 Stress-stretch plots of the smart circular membrane for (a) varying amounts of filler Φ at $\mu_f/\mu_m = 10$, and (b) varying shear modulus ratio μ_f/μ_m at $\Phi = 0.05$ under electromagnetic loading conditions ($V = 0.50$, $M = 0.50$) with $J_m = 97.2$. 98

6.1 (a) Actual structure of the biological organs and schematic representation of the biological membrane: (b) Initial state, (c) Deformed state caused by a radial load P and a uniformly applied transverse pressure P_t, and (d) Equivalent deformed state achieved due to the application of a radial load, along with the transverse electric field. 104

6.2 Schematic representation of the multiplicative decomposition of the deformation gradient $\mathbf{F}$ into the growth component $\mathbf{F}_g$, which defines a naturally grown state, and the elastic component $\mathbf{F}_e$, which restores the compatibility of the deformation. 105

6.3 Variation of equilibrium stretch (λ_{eq}) and dimensionless natural frequency (ω_n) as a function of normalized voltage (V) for (a) $S = 1$ and (b) $S = 5$. . 111

6.4 Variation of equilibrium stretch (λ_{eq}) and dimensionless natural frequency (ω_n) as a function of normalized voltage (V) for different (a) levels of the anisotropy parameter (ξ_1) and (b) fiber orientation angle (θ_f) for isotropic growth ($g_r = g_z = 1$). 113

6.5 Variation of (a) equilibrium stretch (λ_{eq}) and (b) dimensionless natural frequency (ω_n) as a function of normalized voltage (V) for different levels of anisotropic growth. 114

List of Tables

1.1 Comparison of Different Soft Active Materials 6
1.2 Comparison of existing literature and present work. 27
2.1 Comparative summary of previous studies and the present thesis 35
4.1 Electromagnetic models with different considered parameters 73

List of Symbols and Notations

$\mathbf{F}$	Deformation gradient
$\mathbf{F_e}$	Elastic component of deformation
$\mathbf{F_g}$	Growth component of deformation
$\mathbf{B}$	Left Cauchy–Green deformation tensor
$\mathbf{E}$	Electric field at current configuration
$\mathbf{H}$	Magnetic field at current configuration
$\mathbf{D_e}$	Electric displacement field at current configuration
$\mathbf{D_m}$	Magnetic displacement field at current configuration
$\mathbf{T}$	Total Cauchy stress tensor
$\mathbf{I}$	Identity tensor
P	Mechanical load
λ	Stretch
I_i	Tensor invariants ($i = 1, 2, ...$)
J_m	limiting chain extensibility
ε	Electrical permittivity
α	Magnetic permeability
Φ	Amount of filler particles
S	Normalized prestress
μ	Shear modulus
μ_e	Effective shear modulus
U	Normalized effective shear modulus
μ_f	Shear modulus of filler

μ_m	Shear modulus of matrix
W	Energy density function
$S^\star$	PK-1 stress component
υ	Voltage
V	Normalized voltage
Ψ	Flux
M	Normalized flux
g	Principal growth rate
p	Lagrange multiplier
ξ	Degree of anisotropy
ρ	Density
$\mathbf{a}_0$	Undeformed fiber vector
$\mathbf{a}$	Deformed fiber vector
θ_f	Fiber orientation angle

List of Abbreviations

SEDF	Strain energy density function
EAPs	Electroactive polymers
MAPs	Magnetoactive polymers
EMAMs	Electro-magneto-active membranes
DEs	Dielectric elastomers
ESAMs	Electromagnetic soft active materials

Chapter 1

Introduction

Preface

Soft active materials have attracted considerable interest due to their ability to undergo large deformations under external electrical and magnetic fields. Understanding their behavior requires a strong foundation in continuum mechanics and hyperelasticity. This chapter introduces the fundamental concepts of elastomers, soft active materials, constitutive modeling, deformation kinematics, and instability phenomena. It also outlines the motivation, research gaps, objectives, and organization of the thesis.

1.1 Elastomers

Elastomers are a class of soft materials best known for their rubber-like behavior and exceptional ability to deform under mechanical loading. Unlike most conventional engineering materials, which experience only small strains before yielding or failing, elastomers can undergo very large deformations and still return to their original shape once the load is removed. This ability to recover after substantial stretching or compression is a defining characteristic of elastomeric materials.

From a mechanical perspective, elastomers exhibit a fundamentally different stress–strain response compared to traditional solids. While metals and other engineering materials typically display a linear relationship between stress and strain at low deformation levels, elastomers respond in a nonlinear manner from the very

beginning of loading. This nonlinear elastic behavior, commonly referred to as hyperelasticity, allows elastomers to sustain large, fully reversible strains without permanent damage or loss of functionality.

The origin of this remarkable mechanical response lies in the polymeric nature of elastomers. Their structure consists of long, flexible molecular chains that are lightly interconnected through covalent cross-links, forming a three-dimensional network. These cross-links serve to maintain the overall integrity of the material during deformation, preventing irreversible chain slippage while still permitting significant molecular rearrangement. As a result, elastomers combine high flexibility with mechanical robustness, exhibiting good tensile strength, toughness, and resistance to permanent deformation under repeated loading.

Because of these properties, elastomers are used extensively in a wide range of engineering applications. In biomedical contexts, they are commonly employed in soft tissue substitutes, prosthetic components, and wearable devices, where their compliance closely resembles that of natural tissues, improving comfort and performance. In the automotive and aerospace industries, elastomers play a crucial role in components such as tires, seals, and vibration-damping elements, where durability and energy dissipation are essential. They are also widely used in consumer products, including protective and sports equipment, where impact absorption and user comfort are important considerations. More recently, elastomers have become a key enabling material in soft robotics, where their large deformability and resilience allow the development of compliant actuators and grippers capable of safe interaction with complex and delicate environments.

1.2 Soft active materials: electroactive, magnetoactive, and electro-magneto-active materials

Soft active materials constitute a class of deformable solids capable of undergoing significant, reversible mechanical responses under external stimuli. Unlike con-

ventional rigid actuators, these materials combine mechanical compliance with field-induced actuation, enabling muscle-like behavior, large strains, and safe interaction with uncertain environments. Owing to these characteristics, soft active materials have attracted considerable attention in fields such as soft robotics, biomedical engineering, adaptive structures, and smart materials. Among the various subclasses of soft active materials, electroactive materials, magnetoactive materials, and electro-magneto-active hybrid materials are of particular interest due to their strong electromechanical and magneto-mechanical coupling mechanisms.

Electroactive materials are soft materials that deform in response to an applied electric field. In soft matter systems, this category is predominantly represented by electroactive polymers (EAPs), which exhibit large elastic deformations and low elastic moduli comparable to those of biological tissues. Electroactive polymers are commonly divided into two major groups: dielectric electroactive polymers and ionic electroactive polymers. Dielectric elastomers consist of an insulating elastomeric layer sandwiched between compliant electrodes. When subjected to an electric field, electrostatic (Maxwell) stresses induce in-plane expansion and thickness contraction, resulting in large, rapid deformations. Dielectric elastomers are notable for their high energy density, fast response time, and large actuation strains; however, their operation typically requires high driving voltages. In contrast, ionic electroactive polymers, such as ionic polymer–metal composites, rely on ion migration within the polymer matrix to produce bending or swelling deformations. These materials operate at relatively low voltages but generally exhibit slower response times and sensitivity to environmental conditions such as humidity and temperature. Electroactive materials are widely investigated for applications including artificial muscles, soft actuators, haptic interfaces, and micro-scale fluidic devices. From a modeling perspective, their behavior is often described using nonlinear electro-elasticity frameworks that couple large deformation mechanics with electrostatics.

Magnetoactive materials are soft composites whose mechanical properties or deformation states change in response to an applied magnetic field. A representative class within this category is magnetoactive polymers, also referred to as magnetorheological

elastomers. These materials typically consist of an elastomeric matrix embedded with ferromagnetic or ferrimagnetic particles. When exposed to a magnetic field, magnetic forces and torques acting on the embedded particles induce changes in stiffness, damping, or macroscopic shape. Depending on particle distribution and field configuration, magnetoactive materials can exhibit field-dependent anisotropy, tunable elastic moduli, and controlled deformation. Compared to electroactive materials, magnetoactive systems enable wireless and remote actuation, which is particularly advantageous in sealed, submerged, or biomedical environments. Despite these advantages, magnetoactive materials often produce smaller strains than dielectric electroactive polymers and require external magnetic field sources, which may limit portability. Constitutive modeling of magnetoactive materials generally relies on nonlinear magneto-elasticity, accounting for strong coupling between magnetic fields and mechanical deformation. Applications of magnetoactive materials include soft robotic locomotion, adaptive vibration isolation systems, tunable stiffness devices, and minimally invasive medical microrobots.

Electro-magneto-active materials are an emerging class of multifunctional soft materials that respond mechanically to both electric and magnetic fields. By integrating the actuation mechanisms of electroactive and magnetoactive systems within a single material platform, EMA materials are able to exhibit controlled deformation, stiffness variation, and tunable mechanical behavior under independently or simultaneously applied stimuli. This dual responsiveness provides a level of control and adaptability that is difficult to achieve using single-field active materials.

From a structural standpoint, EMA materials are commonly realized as hybrid elastomeric composites. In these systems, a soft elastomer matrix serves as the load-bearing and deformable phase, while electroactive components—such as dielectric elastomers or conductive polymer networks—and magnetically responsive particles are embedded within the matrix. The elastomer ensures large, recoverable deformations, whereas the functional inclusions enable field-driven actuation. By adjusting factors such as particle concentration, spatial distribution, and polymer network properties, the mechanical response of EMA materials can be tailored in terms of deformation

magnitude, response time, and actuation direction under applied electric or magnetic fields.

The coexistence of electric and magnetic actuation mechanisms significantly expands the functional scope of these materials. In soft robotics, EMA materials enable actuators and grippers capable of complex, multi-axis motions and reconfigurable behavior, offering enhanced precision and versatility. In adaptive structures and sensing applications, EMA materials can dynamically alter their stiffness or shape in response to changing operating conditions. In biomedical contexts, their ability to respond to multiple stimuli makes them promising candidates for minimally invasive devices that can be remotely guided and reshaped within the body. Similarly, in aerospace and advanced mechanical systems, EMA materials offer opportunities for vibration control, adaptive load management, and morphing structures.

A particularly attractive feature of EMA materials is their programmable and reversible response. The combination of electroactive and magnetoactive functionalities enables actuation modes that are not accessible in single-stimulus materials, including sequential or multi-stage deformation, directional control through field coupling, and simultaneous tuning of shape and mechanical properties. As a result, EMA materials represent a promising pathway toward the development of next-generation smart materials that unite flexibility, adaptability, and multi-functionality within a single, integrated system. A systematic comparison of the aforementioned materials is presented in Table 1.1.

The actuation behavior of soft active materials is closely linked to the large deformation capability of their elastomeric matrix. Since these materials often experience finite strains, their mechanical response is best described using hyperelasticity. The fundamental concepts of hyperelasticity are therefore introduced in the next section.

1.3 Hyperelasticity

Hyperelasticity is a fundamental principle in analyzing materials capable of undergoing substantial elastic deformations, such as rubber elastomers. Unlike linear

Table 1.1: Comparison of Different Soft Active Materials

S.No.	**Aspect**	**Electroactive Materials**	**Magnetoactive Materials**	**Electro-Magneto-Active Materials**
1	External stimulus	Electric field	Magnetic field	Electric and magnetic fields
2	Actuation mechanism	Electrostatic forces and polarization	Magnetic forces and particle interactions	Combined electro-mechanical and magneto-mechanical coupling
3	Typical material composition	Elastomers with compliant electrodes or ionic constituents	Elastomers embedded with magnetic particles	Hybrid elastomers containing electroactive and magnetic components
4	Response speed	Fast	Moderate to fast	Tunable depending on field interaction
5	Actuation strain	High	Moderate	Moderate to high
6	Control capability	Precise electrical control	Wireless and remote control	Multi-field and adaptive control
7	Key advantage	Large deformation and high energy density	Remote actuation and tunable stiffness	Enhanced versatility and multifunctionality
8	Main limitation	High operating voltage may be required	Dependence on external magnetic field sources	Increased material and modeling complexity
9	Typical applications	Artificial muscles, soft actuators, wearable devices	Soft robotics, vibration control, medical microrobots	Smart actuators, adaptive structures, biomedical systems

elasticity, which assumes small deformations and linear stress-strain relationships, hyperelasticity accounts for the nonlinear behavior observed in materials under significant strains. A comprehensive overview of the fundamental concepts and mathematical formulations associated with hyperelasticity is presented in this section, which is essential for understanding the deformation and failure modeling of rubber elastomers.

1.3.1 Deformation gradient tensor

The deformation gradient tensor is the primary kinematic quantity used to describe finite deformations in continuum mechanics. It characterizes how an infinitesimal material element transforms as the body moves from its reference configuration to its current configuration, thereby capturing the full local deformation at each material point. Let $\mathbf{X}$ denote the position vector of a material point in the reference configuration, and $\mathbf{x}$ its position in the current configuration. The motion of the body is described by the mapping χ:

$$\mathbf{x} = \chi(\mathbf{X},\, \mathbf{t}). \tag{1.1}$$

The deformation gradient tensor F is then defined as:

$$\mathbf{F} = \frac{\partial \mathbf{x}}{\partial \mathbf{X}}. \tag{1.2}$$

$\mathbf{F}$ contains complete information about local stretching, shearing, and rigid-body rotation.

Although the deformation gradient itself is not a strain measure, it serves as the foundation for defining objective strain tensors that eliminate rigid-body motion. The inverse deformation gradient, $\mathbf{F}^{-1}$, maps the current configuration back to its original state, allowing for the analysis of deformation reversal. Two commonly used measures are the right and left Cauchy–Green deformation tensors, defined respectively as:

$$\mathbf{C} = \mathbf{F}^T\mathbf{F}, \quad \mathbf{B} = \mathbf{F}\mathbf{F}^T. \tag{1.3}$$

A key physical quantity associated with the deformation gradient is its determinant,

$$J = det\mathbf{F}, \tag{1.4}$$

which represents the local ratio of deformed volume to reference volume. Values of $J > 1$ indicate local volume expansion, $J < 1$ correspond to volume compression, and $J = 1$ denotes volume-preserving deformation. This property is of particular importance in the modeling of incompressible or nearly incompressible materials. Overall, the deformation gradient tensor provides a comprehensive framework for analyzing finite deformations and is essential for understanding the mechanical behavior of materials under large strains.

1.3.2 Significance of stretch invariants

In the analysis of finite deformations, invariants provide a powerful and intuitive way to describe material deformation without dependence on coordinate systems or observer orientation. Rather than working directly with tensor quantities, which can be difficult to interpret physically, invariants reduce complex deformation states to a small set of scalar measures that remain unchanged under rigid-body motions. This objectivity makes invariants particularly well suited for the formulation of constitutive models in continuum mechanics.

For isotropic materials, the mechanical response depends only on the extent of deformation and not on its direction. In such cases, the deformation can be fully characterized using invariants derived from the Cauchy–Green deformation tensors. These invariants condense the essential information contained in the deformation gradient into quantities that directly reflect stretching, shearing, and volumetric changes within the material.

The first invariant (I_1) is primarily associated with overall stretching and is often interpreted as a measure of the average deformation experienced by the material. It plays a dominant role in many hyperelastic models and is particularly effective in capturing distortional deformation. The second invariant (I_2) accounts for interactions between the principal stretches and is sensitive to shear effects, becoming important in more complex deformation states. The third invariant (I_3) is directly related to volume change and therefore governs the compressibility of the material. For elastomers and other nearly incompressible materials, this invariant is typically constrained, reflecting

their strong resistance to volumetric deformation.

Expressing constitutive relations in terms of invariants offers several advantages. It ensures that material models are frame-indifferent and automatically satisfy the requirement of isotropy. Invariant-based formulations also allow a clear separation between volumetric and deviatoric contributions to the strain energy, which is essential when modeling materials that deform easily in shear but resist changes in volume. Moreover, working with scalar invariants simplifies both analytical derivations and numerical implementations, particularly in finite element simulations.

In the context of active and multifunctional materials, the concept of invariants extends naturally beyond purely mechanical deformation. For electroactive, magnetoactive, and electro-magneto-active materials, additional invariants involving electric and magnetic field quantities can be introduced to describe coupled field–mechanical interactions in a consistent and objective manner. These extended invariants provide a unified framework for capturing complex multiphysics behavior while preserving the fundamental principles of continuum mechanics.

Therefore, invariants offer a physically meaningful and mathematically robust way to describe deformation and material response. Their use is central to modern theories of finite elasticity and plays a key role in the development of reliable constitutive models for both passive elastomers and advanced active materials. The first, second, and third invariants of the left Cauchy–Green tensor are given below:

$$I_1 = \mathrm{tr}(\mathbf{B}), \quad I_2 = \frac{1}{2}\left((\mathrm{tr}(\mathbf{B}))^2 - \mathrm{tr}(\mathbf{B}^2)\right), \quad I_3 = \det(\mathbf{B}). \tag{1.5}$$

1.3.3 Strain energy density function

The strain energy density function (SEDF), denoted by $\mathbf{W}$, is a scalar quantity that represents the elastic energy stored per unit reference volume of a material undergoing deformation. In finite deformation theory, $\mathbf{W}$ is governed by the deformation gradient $\mathbf{F}$ and may equivalently be expressed in terms of the invariants of the right Cauchy–Green deformation tensor $\mathbf{C}$, ensuring objectivity and coordinate independence. By characterizing the stored elastic energy, the strain energy density function

provides the basis for stress computation and enables prediction of material response under various strain states. Furthermore, **W** represents the internal energy associated with deformation, thereby establishing a direct link between deformation kinematics and the resulting stress state. The accurate modeling of hyperelastic materials, such as rubber, under diverse loading conditions relies critically on the appropriate formulation of the strain energy density function. In hyperelasticity, **W** is inherently expressed as a function of invariants derived from the deformation gradient. Some commonly used strain energy density functions are discussed below:

1. ***Neo-Hookean Material Model:*** The Neo-Hookean model is the simplest hyperelastic model and is often used for moderate strains. It assumes that the strain energy density is a function of the first invariant of the deformation tensor. Despite its simplicity, it provides a reasonable approximation for many rubber-like materials under uniaxial or biaxial loading, particularly at small to moderate deformations.

$$W = \frac{\mu}{2}(I_1 - 3) + \frac{\kappa}{2}(J-1)^2, \tag{1.6}$$

where μ is the shear modulus and κ is the bulk modulus.

2. ***Mooney-Rivlin Material Model:*** The Mooney-Rivlin model extends the Neo-Hookean formulation by incorporating two material constants and allowing the strain energy density to depend on both the first and second invariants of the deformation tensor. This model more accurately captures the nonlinear stress–strain response of elastomers over a wider range of deformations and is widely used in engineering simulations.

$$W = C_1(I_1 - 3) + C_2(I_2 - 3) + \frac{\kappa}{2}(J-1)^2, \tag{1.7}$$

where C_1 and C_2 are material constants.

3. ***Gent Material Model:*** The Gent model is designed to capture the strain-stiffening behavior of elastomers at very large stretches. It introduces a limiting chain extensibility parameter, which reflects the finite extensibility of polymer chains. This model is particularly useful when modeling elastomers that exhibit a sharp increase

in stress as the material approaches its maximum elongation.

$$W = -\frac{\mu J_m}{2} \ln\left(1 - \frac{I_1 - 3}{J_m}\right) + \frac{\kappa}{2}(J-1)^2, \tag{1.8}$$

here, μ denotes the shear modulus, while J_m is a material parameter that specifies the limiting value of $(I_1 - 3)$. The invariants I_1 and I_2 are derived from the deformation tensor and characterize the material response associated with distortional deformation. The determinant of the deformation gradient tensor, denoted by J, quantifies the volumetric change during deformation and is defined as the ratio of the deformed volume to the reference volume. The contribution of the volumetric strain energy is expressed as

$$W_{\text{vol}} = \frac{\kappa}{2}(J-1)^2. \tag{1.9}$$

Elastomers, renowned for their exceptional flexibility and elastic properties, find extensive applications across diverse fields. However, their unique properties also present distinct challenges regarding their failure mechanisms.

Investigating these failure modes is critical for designing durable and reliable elastomer-based products. Engineers can improve elastomer performance and lifespan by addressing factors such as deformation instability, fatigue, tear and crack propagation, thermal degradation, creep, and environmental and electrical influences such as electrical breakdown, leakage currents, and electrical degradation in electroactive elastomers. A deep grasp of these failure modes is vital for advancing continuum mechanics and developing innovative elastomeric materials.

While hyperelastic models describe the behavior of elastomers under large deformation, many practical applications require enhanced mechanical performance. This is commonly achieved through reinforcement, making it important to understand the role of particles and fibers in modifying elastomer response.

1.3.4 Stresses

Stress is a fundamental quantity in continuum mechanics that describes the internal forces developed within a material when it is subjected to external loading. For

materials undergoing small deformations, a single stress measure is generally sufficient to characterize the mechanical response. However, hyperelastic materials such as elastomers often experience very large deformations and rotations, making it necessary to define stress with respect to either the undeformed (reference) configuration or the deformed (current) configuration. Consequently, several stress measures have been developed in finite deformation theory, each serving a specific purpose in constitutive modeling, theoretical analysis, and numerical implementation. The most widely used stress tensors are the Cauchy stress, the First Piola–Kirchhoff (PK-1) stress, and the Second Piola–Kirchhoff (PK-2) stress.

1. ***Cauchy Stress Tensor:*** The Cauchy stress tensor, denoted by $\boldsymbol{T}$, represents the true physical stress acting within the material in its deformed configuration. It is defined as the force acting per unit area of the current configuration and therefore corresponds directly to the stress that can be measured experimentally. Since the Cauchy stress is evaluated after deformation has occurred, it provides the actual state of stress experienced by the material during loading. In the absence of body couples, the Cauchy stress tensor is symmetric and is commonly employed in equilibrium equations formulated in the spatial description. The relationship between the Cauchy stress and the First Piola–Kirchhoff stress is expressed as:

$$\boldsymbol{T} = \frac{1}{J}\mathbf{S}^{*}\mathbf{F}^{T}, \tag{1.10}$$

where $J = \det(F)$ represents the local volume ratio associated with the deformation.

2. ***PK-1 Stress Tensor:*** The First Piola–Kirchhoff stress tensor, represented by $\mathbf{S}^{*}$, relates forces in the current configuration to areas measured in the reference configuration. Since it connects quantities defined in two different configurations, it is generally non-symmetric and is therefore referred to as a two-point tensor. Despite this characteristic, the PK-1 stress plays an important role in finite deformation mechanics because it naturally appears in the principle of virtual work, weak formulations, and finite element implementations. For hyperelastic materials, the First Piola–Kirchhoff stress is obtained directly from the strain energy density function by differentiating

the energy with respect to the deformation gradient,

$$\mathbf{S}^{*} = \frac{\partial W}{\partial \mathbf{F}}, \tag{1.11}$$

where W denotes the strain energy density function. This relationship establishes a direct connection between the constitutive model and the material deformation.

3. ***PK-2 Stress Tensor:*** The Second Piola–Kirchhoff stress tensor, denoted by $\mathbf{S}^{**}$, is entirely defined in the reference configuration and is energetically conjugate to the Green–Lagrange strain tensor. Unlike the PK-1 stress, the PK-2 stress is symmetric because it is independent of rigid-body rotations. This property makes it particularly attractive for constitutive modeling and theoretical developments in nonlinear elasticity. Since both stress and strain are expressed with respect to the reference configuration, the PK-2 stress provides a convenient framework for deriving material constitutive laws. It is defined as:

$$\mathbf{S}^{**} = 2\frac{\partial W}{\partial \mathbf{C}}, \tag{1.12}$$

where $\mathbf{C} = \mathbf{F}^{T}\mathbf{F}$ is the right Cauchy–Green deformation tensor.

Although these three stress measures describe the same physical state of stress, they differ in their mathematical formulation and practical applications. The Cauchy stress provides the actual stress acting in the deformed body and is primarily used for interpreting the physical response of the material. The First Piola–Kirchhoff stress is particularly useful in variational formulations and finite element analysis because it directly relates to the deformation gradient. In contrast, the Second Piola–Kirchhoff stress is widely adopted in constitutive modeling due to its symmetry and reference-configuration formulation. Together, these stress measures provide a comprehensive framework for analyzing finite deformation problems and form the basis of modern hyperelastic constitutive theories used for elastomers and electro-magneto-active materials.

1.4 Reinforcement in elastomers

Elastomers are widely used in soft engineering applications due to their ability to undergo large, reversible deformations. However, their inherent softness and low stiffness often limit their load-carrying capacity, durability, and resistance to instability or failure. To overcome these limitations, reinforcement strategies are commonly employed to enhance the mechanical performance of elastomers while preserving their desirable flexibility. Reinforcement modifies the material response by altering stiffness, strength, anisotropy, and energy dissipation characteristics, thereby enabling elastomers to meet the demands of advanced engineering applications. Reinforcement in elastomers is generally achieved through the incorporation of particles or fibers into the polymer matrix. Each reinforcement mechanism influences the mechanical and electromechanical behavior of elastomers in distinct ways, and their effects become particularly significant under large deformation and dynamic loading conditions.

1.4.1 Particle reinforcement

Particle reinforcement is one of the most widely used methods for improving the mechanical properties of elastomers. In this approach, rigid or semi-rigid particles—such as carbon black, silica, ferrites, or metallic particles—are dispersed within a soft polymer matrix. These fillers enhance the effective stiffness and strength of the elastomer by restricting polymer chain mobility and increasing resistance to deformation as shown in Fig. 1.1. From a mechanical standpoint, particle reinforcement leads to an increase in the effective shear modulus, tensile strength, and fatigue resistance of elastomers. The overall material response depends strongly on factors such as particle volume fraction, size, shape, and matrix–filler interaction. At moderate filler concentrations, particles act as load-bearing inclusions that transfer stress from the matrix, while at higher concentrations, filler–filler interactions can significantly alter the nonlinear stress–strain behavior. In smart elastomers, particle reinforcement plays an additional functional role. Magnetic or electrically active particles introduce field-dependent mechanical behavior, enabling actuation and tunability under

external electric or magnetic fields. In electro-magneto-active elastomers, particle reinforcement directly affects electromagnetic coupling, dynamic stiffness, vibration characteristics, and stability boundaries. Consequently, particle-reinforced elastomers are extensively used in applications requiring controllable dynamic response, such as soft actuators, sensors, and adaptive membranes.

1.4.2 Fiber reinforcement

Fiber reinforcement introduces a fundamentally different reinforcement mechanism by imparting directional stiffness and anisotropy to elastomers. Fibers embedded within a soft matrix can be aligned in specific orientations, allowing the mechanical response of the material to vary with direction. This feature is particularly advantageous for controlling deformation modes, enhancing load-bearing capacity, and sup-

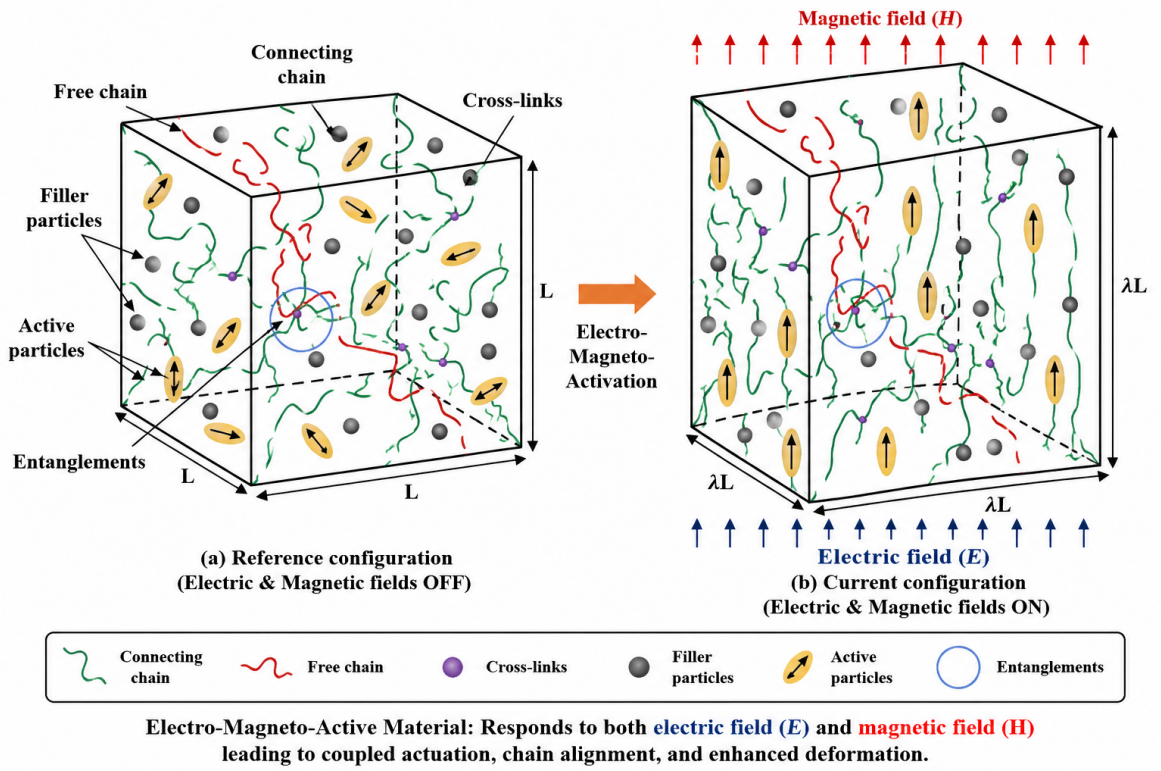


Figure 1.1: A schematic representation of an electro-magneto-active filler-reinforced elastomeric material undergoing deformation.

pressing undesired instabilities. Fiber-reinforced elastomers are strongly inspired by biological tissues, where collagen or muscle fibers play a dominant role in governing mechanical behavior. In engineered systems, fibers may be continuous or discontinuous and can be arranged in single or multiple families to achieve tailored mechanical responses. The stiffness, orientation, and volume fraction of fibers directly influence the stress distribution, stretch limits, and energy storage capability of the elastomer. Under large deformation and dynamic loading, fiber reinforcement significantly affects the nonlinear behavior. Fibers resist stretching along their orientation while allowing compliant deformation in transverse directions. This anisotropic response becomes particularly important in membrane structures, where fiber architecture can delay instability, modify vibration characteristics, and regulate nonlinear oscillatory behavior. In smart elastomers subjected to electric and magnetic fields, fiber reinforcement further interacts with field-induced stresses, making it a critical design parameter in advanced actuator and membrane applications.

1.4.3 Impact of reinforcement on failure modeling of elastomers

Failure in elastomers is not a single event but a progressive process that develops as deformation, loading rate, and environmental effects increase. In unreinforced elastomers, failure is typically governed by excessive chain stretch, leading to molecular scission and eventual rupture. The deformation is usually homogeneous, and failure occurs once a critical stretch limit is reached.

When reinforcement is introduced, the failure process becomes more complex due to material heterogeneity. Reinforcements alter local stress and strain fields, which leads to the initiation of damage at specific locations before global failure occurs.

In **particle-reinforced elastomers**, failure often begins at the particle–matrix interface. Under large deformation, stress concentrations develop around rigid inclusions, which can trigger interfacial de-bonding, micro-void formation, or cavitation within the matrix. These micro-defects grow and coalesce under continued loading,

eventually forming macroscopic cracks. While particle reinforcement can delay overall failure by increasing stiffness and energy dissipation, high filler concentrations may accelerate damage localization and reduce stretchability.

In **fiber-reinforced elastomers**, failure mechanisms are strongly influenced by fiber orientation and loading direction. Fibers restrict deformation along their alignment, which helps suppress excessive stretch and delay rupture. However, when critical stresses are exceeded, failure may occur through fiber fracture, fiber pull-out, or fiber–matrix de-bonding. Damage tends to initiate in regions of high anisotropic stress, and crack propagation often follows fiber directions, resulting in direction-dependent failure behavior.

Under **dynamic or cyclic loading**, damage accumulates progressively through fatigue mechanisms. Repeated loading promotes interface degradation, micro-crack growth, and loss of stiffness, eventually leading to catastrophic failure at stress levels well below the static strength.

In **electro-magneto-active elastomers**, additional failure modes arise due to electromagnetic actuation. Electric fields can induce electrostatic thinning and pull-in instability, while magnetic fields may lead to localized stress amplification. Reinforcement modifies these field-induced stresses, influencing the onset of electrical breakdown, instability, or mechanical rupture.

Overall, failure in reinforced elastomers results from the interaction between large deformations, material nonlinearity, reinforcement-induced stress concentrations, and multi-field coupling. Capturing these mechanisms in failure models is essential for predicting durability and defining safe operating limits in advanced elastomer-based systems.

Besides influencing mechanical behavior, reinforcement also affects the interaction of elastomers with electric and magnetic fields. This makes it important to understand the deformation-dependent electromagnetic properties of these materials.

1.5 Stretch-dependent electromagnetic effects

Electric permittivity and magnetic permeability are fundamental properties of electromagnetic materials that describe how a medium responds to electric and magnetic fields, respectively. Electric permittivity, denoted by ε, characterizes the ability of a material to polarize under an applied electric field and governs the relationship between the electric field $\mathbf{E}$ and the electric displacement field $\mathbf{D}$, commonly expressed as:

$$\mathbf{D} = \varepsilon \mathbf{E}. \tag{1.13}$$

Magnetic permeability, denoted by α, quantifies the extent to which a material can be magnetized in response to an applied magnetic field and relates the magnetic field intensity $\mathbf{H}$ to the magnetic flux density $\mathbf{B}$ as:

$$\mathbf{B} = \alpha \mathbf{H}. \tag{1.14}$$

In classical electromagnetic theory, both permittivity and permeability are often treated as intrinsic constants of the material. However, this assumption becomes inadequate for soft elastomeric materials undergoing finite deformation. Due to the highly compliant nature of their polymeric networks, elastomers experience pronounced micro-structural rearrangements when subjected to mechanical stretching. These deformation-induced changes directly influence the polarization and magnetization mechanisms, leading to electromagnetic properties that evolve with the mechanical state of the material. At the micro-structural level, mechanical stretch promotes alignment of polymer chains along the principal deformation directions, reducing configurational entropy and introducing anisotropy. Electric dipoles associated with the polymer backbone or side groups tend to reorient under the combined action of mechanical deformation and externally applied electric fields. In nearly incompressible elastomers, in-plane stretching is accompanied by a reduction in thickness, which modifies the local electric field distribution within the material. These effects collectively alter the effective dipole density and polarization efficiency, resulting in a stretch-dependent electric permittivity. This behavior is commonly referred to as

electrostriction in soft polymeric systems. In magnetoactive and electro–magneto-active elastomers, deformation also affects magnetic permeability through additional mechanisms. Such materials typically contain magnetic particles dispersed within a soft elastomeric matrix. Mechanical deformation changes the relative spacing, orientation, and interaction of these particles, thereby modifying magnetic dipole–dipole interactions and magnetic flux pathways. As a result, the magnetization response of the material becomes deformation-dependent, leading to a stretch-dependent magnetic permeability associated with magnetostrictive effects and particle rearrangement. From a continuum mechanics perspective, the deformation dependence of permittivity and permeability arises naturally within an energy-based constitutive framework. The total free energy density $\mathbf{W}$ of a soft electromagnetic material can be expressed as a function of the deformation gradient $\mathbf{F}$, the electric field $\mathbf{E}$, and the magnetic field $\mathbf{H}$,

$$\mathbf{W} = \mathbf{W}(\mathbf{F}, \mathbf{E}, \mathbf{H}). \tag{1.15}$$

Since polarization and magnetization energies are influenced by deformation-induced microstructural changes, the constitutive relations take the form

$$\mathbf{D} = \varepsilon(\mathbf{F})\mathbf{E}, \quad \mathbf{B} = \alpha(\mathbf{F})\mathbf{H}. \tag{1.16}$$

or equivalently, for isotropic materials, as functions of stretch or strain invariants. Thus, permittivity and permeability are introduced as deformation-dependent material functions rather than fixed constants.

This deformation dependence has important implications for the mechanical response of soft active materials. Electromagnetic body forces and stresses, commonly represented through Maxwell-type stress tensors, depend explicitly on permittivity and permeability. When these properties vary with deformation, the resulting electromagnetic stresses become strongly coupled to the mechanical state of the material. This coupling significantly influences equilibrium configurations, stability behavior, and dynamic responses, particularly under large strains and field-driven actuation. Therefore, for a physically accurate and thermodynamically consistent description of soft active materials undergoing finite deformation, it is essential to incorporate

stretch-dependent permittivity and permeability into constitutive models. Neglecting this dependence can lead to significant errors in predicting actuation forces, instability thresholds, and nonlinear response characteristics, especially in regimes dominated by large deformations.

The coupling between mechanical deformation and electromagnetic fields has a direct impact on the stability of soft active materials. Under combined loading conditions, membranes may develop regions that remain stretched and stable, while others become susceptible to deformation. This behavior leads to the concept of taut domains, which plays a significant role in understanding the stability and performance of soft active systems.

1.6 Taut domains and field-induced instabilities

A domain is said to be taut when it is maintained in a state of tensile pre-stress through stretching or boundary constraints as shown in Fig. 1.2. In soft elastomeric materials, tautness plays a central role in governing mechanical stability. The presence of tensile stress results in stored elastic energy, making deviations from the equilibrium configuration energetically unfavorable. Consequently, small perturbations are suppressed, and the system remains in a stable, smooth configuration under modest loading conditions.

In the absence of external fields, a taut soft domain typically represents a stable equilibrium state. The elastic resistance associated with tension inhibits out-of-plane deformation, buckling, and wrinkling, and the mechanical response to small disturbances remains linear. However, this stability is conditional and can be altered by the application of external stimuli. When electric or magnetic fields are applied, additional energetic contributions arise through polarization and magnetization of the material. These field–matter interactions generate internal body forces and Maxwell-type stresses that act in conjunction with the mechanical stresses induced by tension. At low field intensities, the contribution of electromagnetic forces is small relative to the elastic energy stored in the taut configuration, and the stabilizing effect of tension

remains dominant. As the field intensity increases, the electromagnetic contribution to the total free energy becomes increasingly significant. Beyond a critical field threshold, the stabilizing influence of tension may be insufficient to counteract the field-induced forces. Under such conditions, the taut equilibrium state loses stability, and the system undergoes a field-induced instability. This transition corresponds to the emergence of a new deformation mode that reduces the total energy under combined mechanical and field loading.

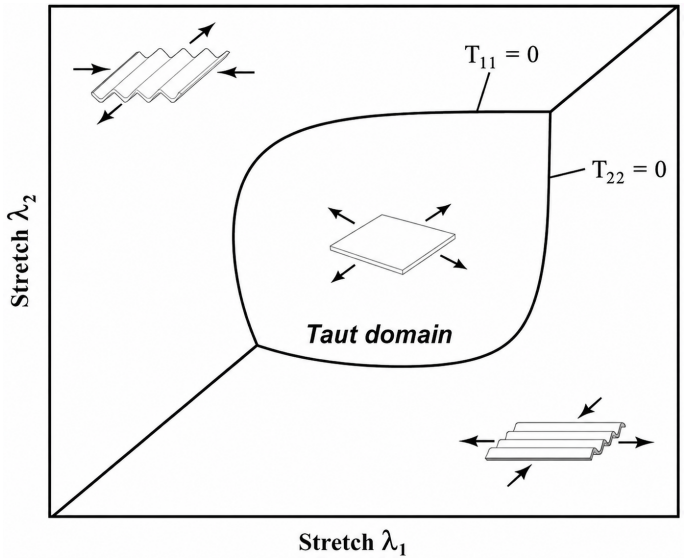


Figure 1.2: A schematic representation of the taut and wrinkled region [1].

Field-induced instabilities in soft domains typically manifest as buckling, wrinkling, folding, or the formation of spatially periodic deformation patterns. From a theoretical perspective, the onset of instability is characterized by a loss of stability of the equilibrium solution and is commonly identified by the vanishing of the second variation of the total energy or by the appearance of zero or negative eigenvalues in the linearized stability problem. The instability marks a bifurcation point beyond which multiple equilibrium configurations may exist. The critical conditions for instability and the post-bifurcation behavior depend on several interacting factors, including the level of pre-stretch, the geometry and thickness of the domain, boundary conditions, and the constitutive response of the material. In electroactive, magnetoactive, and electro-magneto-active elastomers, deformation-dependent electric permittivity

and magnetic permeability further influence the instability behavior by modifying the magnitude and distribution of electromagnetic stresses during deformation.

A rigorous understanding of taut domains and field-induced instabilities is essential for the accurate modeling of soft active materials. Such understanding underpins the prediction of stability limits and deformation patterns in soft actuators, adaptive structures, and multifunctional smart material systems, where instabilities may be exploited for controlled shape transformation or suppressed to ensure structural reliability.

The behavior of taut domains provides valuable insight into the stability of soft active materials. Under varying mechanical and electromagnetic loading, these materials may experience different forms of instability that significantly influence their deformation and performance. Therefore, an understanding of common stability phenomena is essential for the analyses presented in the next section.

1.7 Stability issues: pull-in, snap-through, bifurcation, and dynamic instability

Structural stability refers to the ability of a system to maintain equilibrium under external disturbances. In nonlinear systems, stability loss may occur through several distinct mechanisms, including pull-in instability, snap-through instability, bifurcation instability, and dynamic instability. These phenomena are characterized by sudden changes in equilibrium configuration, deformation mode, or dynamic response, and play a critical role in the design of structures ranging from macro-scale shells to micro and nano electromechanical systems.

1. ***Pull-in Instability:*** Pull-in instability is a form of static instability commonly observed in systems where an attractive force increases nonlinearly with displacement. It is particularly prominent in electrostatically actuated micro and nano-scale structures. As the control parameter (e.g., voltage) increases, the equilibrium between the restoring elastic force and the attractive force is maintained only up

to a critical value. Beyond this point, no stable equilibrium exists, and the structure collapses abruptly onto the counter-electrode. Mathematically, pull-in instability corresponds to the disappearance of equilibrium solutions, often associated with a saddle–node (fold) bifurcation in the force–displacement curve.

2. ***Snap-through Instability:*** Snap-through instability occurs in structures possessing multiple stable equilibrium configurations, such as shallow arches, shells, and bistable mechanisms. Unlike pull-in instability, snap-through does not involve collapse, but rather a sudden transition between distant equilibrium states. As loading increases, the primary equilibrium path becomes unstable, causing the structure to rapidly transition to an alternative stable configuration. This phenomenon is associated with a non-convex potential energy landscape containing multiple local minima. Snap-through is typically reversible, though it may exhibit hysteresis depending on the loading path.

3. ***Bifurcation Instability:*** Bifurcation instability arises when a system loses stability by developing new equilibrium paths that branch from the original solution. This type of instability is common in symmetric structures subjected to compressive loads. The classical example is the Euler buckling of a straight column. At the critical load, the trivial (straight) equilibrium becomes unstable, and two symmetric buckled configurations emerge. The system selects one branch, often influenced by imperfections or external disturbances. From a mathematical perspective, bifurcation instability is identified by the vanishing of a critical eigenvalue of the system stiffness matrix.

4. ***Dynamic Instability:*** Dynamic instability involves time-dependent effects and cannot be captured through static equilibrium analysis alone. In these systems, instability manifests as oscillations whose amplitudes grow with time due to insufficient damping or continuous energy input. Common forms of dynamic instability include flutter, parametric resonance, and self-excited oscillations. Even when the static configuration is stable, inertial effects may destabilize the system under dynamic loading conditions. Dynamic instability is generally analyzed through linearized equations of motion, with stability determined by the sign of the real parts of system eigenvalues.

Instability phenomena such as **pull-in, snap-through, bifurcation, and dynamic instability** represent fundamental nonlinear behaviors in structural systems. Although often associated with failure, these mechanisms can also be exploited for functional purposes, including sensing, actuation, and energy harvesting. Accurate modeling and stability analysis are, therefore, critical components of modern structural design.

1.8 Motivation of the thesis

The growing demand for soft, adaptive, and multifunctional systems has shifted engineering research toward smart elastomeric materials capable of large, controllable deformations. Elastomeric membranes, in particular, have attracted significant attention due to their lightweight nature, geometric simplicity, and ability to undergo substantial deformation under relatively low actuation energy. These features make them ideal candidates for applications such as soft actuators, artificial muscles, biomedical devices, and adaptive structures. Electro-magneto-active elastomers represent an advanced class of smart materials that can respond simultaneously to electric and magnetic fields, offering greater actuation flexibility and tunability compared to single-field systems. In real operating conditions, such membranes are typically driven by time-varying electric and magnetic fields, resulting in inherently nonlinear dynamic behavior. This includes phenomena such as nonlinear oscillations, bi-stability, resonance, and instability, which directly affect device performance, efficiency, and reliability. A clear understanding of these nonlinear dynamic responses is therefore essential for the rational design of electro-magneto-active membrane-based systems.

The material architecture plays a crucial role in the regulation of the response of such membranes. Particle reinforcement is widely used to enhance the stiffness and strength of soft elastomers while maintaining their compliance. The inclusion of filler particles modifies the effective shear modulus of the membrane and significantly influences its dynamic characteristics, including vibration amplitude, natural frequency, and stability limits. Despite its practical importance, the role of particle reinforcement

in the nonlinear dynamic response of electro-magneto-active membranes has been addressed only in a limited and fragmented manner in existing studies. In addition to particle reinforcement, fiber reinforcement introduces anisotropy, allowing the mechanical response of the membrane to depend on direction. Fiber-reinforced membranes are particularly relevant from a bio-inspired perspective, as many biological tissues and membranes exhibit organized fiber architectures that regulate deformation, growth, and stability. In engineered elastomeric membranes, fiber orientation and stiffness can be strategically designed to control deformation modes, delay instability, and improve load-bearing capacity. However, most existing models of electro- and magneto-active membranes assume isotropic material behavior and therefore overlook the influence of fiber-induced anisotropy, especially under dynamic electro-magneto-mechanical loading.

Another important aspect that remains insufficiently explored is the coupling between reinforcement mechanisms and electromagnetic actuation. The simultaneous presence of large deformations, nonlinear material behavior, particle- and fiber-induced stiffness variations, and coupled electric and magnetic fields leads to highly complex system dynamics. Current theoretical frameworks often treat these effects in isolation, which limits their ability to accurately predict stability boundaries, resonance behavior, and energy exchange in realistic membrane actuators.

Motivated by these limitations, this Ph.D. research focuses on developing a continuum-mechanics-based analytical framework to study the nonlinear static and dynamic behavior of particle- and fiber-reinforced electro-magneto-active circular membranes. The research systematically examines how reinforcement parameters—such as filler content, shear modulus ratio, fiber orientation, and anisotropy—interact with electro-magneto-mechanical loading to influence equilibrium states, stability, nonlinear vibrations, and dynamic response characteristics. By combining advanced constitutive modeling with nonlinear dynamical analysis tools, this work aims to bridge the gap between material design and system-level performance. The outcomes of this research are expected to provide physically grounded insights and practical design guidelines for developing stable, tunable, and high-performance smart membrane actuators, with

applications in soft robotics, biomedical engineering, and adaptive intelligent structures. The comparison of the findings of the existing studies with the present work is shown in Table 1.2.

1.9 Organization of the thesis

This thesis is organized into seven chapters, each addressing a specific aspect of the mechanics, dynamics, and stability of soft active elastomeric materials under electric and magnetic fields.

- **Chapter 1** introduces the fundamental concepts required for the present study. It discusses elastomers and soft active materials, including electroactive, magnetoactive, and electro–magneto-active systems. Key notions of finite deformation, hyperelasticity, invariants, and reinforcement effects are presented. The chapter also introduces stretch-dependent electromagnetic properties, taut domains, and field-induced instabilities, and concludes with the objectives of the thesis.

- **Chapter 2** reviews the relevant literature on soft active materials, reinforced elastomers, and coupled field–mechanical behavior. Existing theoretical, experimental, and numerical studies are critically assessed, leading to the identification of research gaps and the formulation of the thesis objectives.

- **Chapter 3** investigates the dynamics of particle-reinforced electro–magneto-active circular membranes. A theoretical model is developed, governing equations are derived, and the DC dynamic response is analyzed, with particular emphasis on nonlinear and chaotic behavior.

- **Chapter 4** examines the role of stretch-dependent electric permittivity and magnetic permeability in the dynamic response of soft active materials. Both DC and AC excitations are considered, and the influence of different constitutive models on system behavior is analyzed.

Table 1.2: Comparison of existing literature and present work.

S.No.	Study	Area	Key Findings	Research Gap	Present Work
1	Behera et al. (2023)	Nonlinear electroactive membrane dynamics	Resonance, bifurcation, and chaos	Limited reinforcement studies	Effects of filler content and modulus ratio on dynamics.
2	Kuhl et al. (2014)	Growth in biological membranes	Reinforcement and viscous effects	Combined growth, reinforcement, and electric loading unexplored	Snap-through and bifurcation in fiber-reinforced membranes.
3	Khurana et al. (2022)	Instability and taut domains in DE membranes	Instability analysis	Limited studies on reinforced EMA membranes	Taut domains and stability under coupled loading.
4	Joglekar et al. (2021)	Particle-reinforced electro-magneto-active actuators	Reinforcement and viscous effects	Circular geometry not considered	Field coupling and reinforcement in circular membranes.
5	Li et al. (2021)	Instability with stretch-dependent permittivity	Pull-in instability	Stretch-dependent permeability neglected	Stretch-dependent electromagnetic properties.
6	Patra et al. (2024)	Electro-magneto-active membrane dynamics	Periodicity and stability	Circular geometry not considered	Field coupling and reinforcement in circular membranes.

- **Chapter 5** focuses on the formation and stability of taut domains in particle-reinforced EMAMs. The effects of electric and magnetic fields, particle volume fraction, and material shear modulus ratio are systematically studied.

- **Chapter 6** extends the analysis to biological membranes. Snap-through instabilities and bifurcation behavior are investigated for isotropic and anisotropic growth, including membranes reinforced with fibers.

- **Chapter 7** summarizes the main findings of the thesis and highlights their significance. The chapter concludes with suggestions for future research and possible extensions of the present work.

Chapter 2

Literature Survey

Preface

A clear understanding of existing research is essential for identifying unresolved challenges. This chapter reviews the literature on electro-magneto-active membranes, including particle reinforcement, stretch-dependent electromagnetic properties, taut domain analysis, and field-induced instabilities. The limitations of current studies are discussed, leading to the research objectives addressed in this thesis.

2.1 Literature review

The current trend in technology shows a gradual shift from hard, single-purpose devices to soft, multifunctional alternatives. This transition has sparked an increase in interest in innovative engineering materials for the next generation of electronic devices, particularly soft active polymers, commonly referred to as smart elastomers [2–8]. The most commonly used soft active materials include electroactive polymers [9–11], magnetoactive polymers [12–14], and electro-magneto-active polymers [15–17]. Specifically, electro-magneto-active polymers are advanced materials with the unique ability to simultaneously address multiple functional requirements in the design of intelligent systems.

2.1.1 Dynamics of particle-reinforced EMAMs

Significant advancements in polymer technology have enabled the incorporation of reinforcement into rubber-like matrices [18, 19], resulting in materials capable of large nonlinear deformations and enhanced properties such as light weight, cost-effectiveness, and rapid response times. Fillers play a pivotal role in optimizing the functional properties of these smart polymers while simultaneously reducing the overall cost of their composites. Extensive experimental research [20–22] has examined the mechanical behavior of rubber elastomers with varying filler volume fractions. These studies demonstrate that the mechanical properties of polymers can be precisely tailored by modifying the volume fraction, shape, and size of the filler particles.

In practical applications, smart elastomer-based devices exhibit transient motion as an integral part of their operation. Hence, for an efficient design of such devices, it is very important to analyze the dynamic response of the elastomers. In this regard, the energy-based technique (such as Euler-Lagrange and Hamiltonian techniques) [23–25] and the direct equilibrium equation approach (DEEA) [26,27] are two distinct methods used for analyzing the dynamic response of systems, including elastomeric membranes.

Specifically, under dynamic loading conditions, elastomeric materials display nonlinear vibrations. Nonlinear dynamical assessments are conducted by several researchers on a range of structures, including planar, spherical, and cylindrical ones [28, 29]. Pre-stretch and bi-stability effects are mainly considered in the dynamical analysis. Studies on dielectric elastomer materials have documented dynamical features such as chaos, quasi-periodicity, and the change in the quasi-periodic route to chaos [30, 31]. Moreover, the dynamics due to an applied AC voltage alter the membrane capacitance.

2.1.2 Stretch-dependent electromagnetic properties and dynamic response

In their study, Wissler and Mazza [32] conducted electrostriction experiments on a VHB 4910 dielectric elastomer. They discovered the electrostrictive effect, which is de-

fined as the field-dependent electromechanical pressure and the deformation-dependent electric permittivity [32]. Zhao discovered that voltage-induced deformation can only be explained by the Maxwell stress tensor in smart materials where the electric permittivity is independent of deformation for very small deformation but restricted for a large deformation case [33]. Similarly to the analysis of the electrostriction phenomenon, the magnetostriction phenomenon has been studied to understand how smart materials respond to an external magnetic field. The theoretical foundation for magneto-sensitive elastomers was established by [34–36] through the application of nonlinear magneto-elasticity principles. Their work provided a comprehensive framework for understanding the complex interactions between magnetic fields and the mechanical behavior of elastomers, laying the foundation for further advancements in the field.

Incorporating stretch-dependent electric permittivity and magnetic permeability in electromagnetic soft active materials (ESAMs) is essential for accurately predicting and optimizing their performance in applications such as soft robotics, flexible electronics, and tunable metamaterials. These materials, including dielectric elastomers (DEs) and magnetorheological elastomers (MREs), exhibit significant coupling between mechanical deformation and electromagnetic properties. As ESAMs undergo deformation, their internal structures reconfigure, leading to variations in their dielectric and magnetic responses. Neglecting these dependencies can result in substantial discrepancies between theoretical models and experimental outcomes, thereby limiting the effectiveness of these materials in practical applications. Recent studies have underscored the importance of accounting for these stretch-dependent properties. Electric permittivity is a key factor in accurately modeling the nonlinear electromechanical behavior of dielectric elastomers. This effect is especially significant in materials like VHB, where permittivity changes with deformation [37, 38]. Empirical studies by Srivastava and Basu [39] demonstrate that permittivity increases with stretch, while dielectric breakdown strength shows a nonlinear dependence on deformation. For instance, Moucka et al. [40] investigated the dielectric properties of MREs with different microstructures, demonstrating that the alignment of magnetic particles under

an external magnetic field significantly influences the material's permittivity. Similarly, Isaev et al. [41] conducted numerical simulations on the magnetodielectric effect in MREs, revealing that mechanical deformation and particle displacement within the elastomer matrix lead to notable changes in effective permittivity. Additionally, Snarskii et al. [42] investigated the effect of magnetic-field-induced restructuring on the elastic properties of magnetoactive elastomers, demonstrating that mechanical deformation can lead to significant changes in both magnetic permeability and dielectric permittivity.

2.1.3 Taut domain formation in particle-reinforced EMAMs

In recent years, taut domain analysis has emerged as a powerful tool for investigating a wide range of instabilities in smart elastomers, significantly advancing the understanding of their actuation behavior and operational limits [43–45]. Within the context of smart polymer membranes, taut states describe the in-plane stretch conditions that arise when the membrane is under mechanical tension. These states are characterized by positive principal stretches—either in both directions, indicating a fully taut configuration, or in only one direction, representing a partially taut or wrinkled state [46]. Conversely, regions where neither principal stretch is tensile are classified as bounded or balanced zones. In these zones, the membrane is not in a taut state, and while they do not immediately trigger localized instabilities, they mark areas where mechanical support is lost, potentially compromising the functional reliability of the device. Unlike regions within the taut domain, these zones are less prone to sudden instabilities such as wrinkling or buckling, but their presence can still influence the overall electromechanical performance. Identifying and mapping taut domains within a smart elastomeric membrane is therefore critical for predicting critical operating conditions, avoiding instability-induced failure, and guiding the design and material selection processes.

Several previous studies have investigated the formation of taut domains and their relationship with instability phenomena in dielectric elastomer-based actuators [7, 43, 44, 47]. These studies primarily focus on failure mechanisms induced by applied

electric fields, which are important for understanding the performance limitations of such actuators. However, dissipative effects in elastomer-based actuators have received comparatively less attention, despite their significant influence on the overall system response [48–50]. Furthermore, various instabilities, including pinnacle vibrations [51], dynamic snap-through [52], and pull-in instability [24], present considerable challenges to the reliable performance of these actuators [33].

Motivated by these studies, the present work investigates the formation of taut domains in particle-reinforced electro-magneto-active thin circular membranes. These membranes offer potential applications in the development of reinforced smart actuators for advanced engineering systems. To the best of our knowledge, this study is the first to specifically investigate taut domain formation in such particle-reinforced electro-magneto-active membrane systems.

2.1.4 Stability and field-induced instabilities in biological membranes

Biological membranes deform, alter their shape, and change permeability in response to variations in electro-mechanical field forces. Morpho-elasticity is the term typically used to describe such phenomena by physically coupling the morphological changes of the membrane (such as stretching, bending, folding, and growth) with the electro-mechanical field responses of the material [53]. During growth, biological membranes undergo changes in size, shape, and composition. The intricate signaling pathways and electro-mechanical signals that control these activities heavily rely on the morpho-elastic characteristics of the membrane [54]. Many applications, such as innovative drug delivery, elucidating biological mechanics, and developing customized biomimetic materials, nanotechnology, biophysics, and bioengineering, require investigating these morphoelastic phenomena. Numerous studies [55–58] confirmed that the emergence of biological membranes is triggered by differential volumetric growth. The unique morphological dynamics of human pluripotent stem cell cysts have also been studied in recent publications [59, 60], showing that elasticity and anisotropic growth

control this process.

Only few existing studies [61–66] have explored how electric fields affect the behavior of biological membranes. Previous studies on such membranes, except a recent one [26], neglected to take biological membranes' nonlinear dynamics into account in response to electro-mechanical stimuli. In particular, Behera et al. [26] examined the nonlinear dynamics of a biological circular membrane under electrically induced mechanical loading conditions. The study [26] forecasted the dynamic response of the membrane subjected to electro-mechanical loads using a continuum physics-based analytical modeling framework. The parametric studies explored varying sinusoidal voltages to assess multi-frequency resonance behavior and stability parameters.

Despite these advances, certain important aspects of biological membrane mechanics remain insufficiently explored. In particular, differential volumetric growth can drive membrane formation, while elasticity and anisotropic growth play crucial roles in governing stem cell cyst dynamics. Moreover, biological structures such as liposomes and micelles may exhibit fiber-reinforced characteristics that can significantly influence their mechanical response. However, these growth-related effects and fiber reinforcement have not been systematically incorporated into existing membrane models, particularly in studies addressing their nonlinear dynamic behavior. Table 2.1 compares representative studies in terms of their modeling frameworks, loading conditions, reinforcement mechanisms, analyses, and remaining research gaps.

2.2 Literature gap

Several potential research directions that should be explored to enrich the research area are identified based on the literature:

2.2.1 Dynamics of particle-reinforced EMAMs

It is observed that, first, relatively few researchers have investigated the effect of particle reinforcement on the dynamic behavior of elastomers, and only for planar geometries. Second, a handful of studies pertaining to the dynamic response of

Table 2.1: Comparative summary of previous studies and the present thesis

Study	**Geometry and model**	**Loading and reinforcement**	**Analysis**	**Research Gap/contribution**
Behera et al. [26]	Biological circular membrane; nonlinear model	Mechanical and electric; no reinforcement	Dynamic response	Combined fields and particle reinforcement
Khurana et al. [1]	Thin active membrane; continuum model	Electric and magnetic; material anisotropy	Taut domains	Effect of particle reinforcement on taut domains
Patra et al. [16]	Active membrane; nonlinear model	Electric and magnetic; electrode effects	Dynamic response	Particle-reinforced circular membrane dynamics
Li et al. [67]	Soft dielectric; variable permittivity	Electric; no reinforcement	Instability	Combined variation of permittivity and permeability
Joglekar et al. [68]	Particle-reinforced active actuator	Electric and magnetic; particles	Nonlinear oscillations	Dynamics and stability of circular membranes
Present thesis	Circular membrane; Gent-based models	Mechanical, electric and magnetic; particles and fibers	Dynamics and stability	Combined effects investigated across Chapters 3–6

the elastomer subjected to electro-magneto-mechanical loadings have been reported. Third, the effect of filler particles on the nonlinear dynamic response of the smart elastomer-based actuators has not hitherto been addressed in the literature. This gap in knowledge underscores the need for further investigation into how these complex stimuli due to particle reinforcement influence membrane behavior. Additionally, the current literature lacks a robust mathematical model that adequately captures the intricate dynamics of the system, highlighting a significant opportunity for advancements in theoretical frameworks. In this research, we aim to utilize a mathematical framework to describe the nonlinear dynamics of a particle-reinforced circular membrane using the direct equilibrium equation approach. The study integrates the membrane's electrical, magnetic, and mechanical control modes to explore their synergistic design features.

2.2.2 Stretch-dependent electromagnetic properties and dynamic response

Existing studies on active membranes have largely considered electrical permittivity and magnetic permeability as constant material properties. However, these properties may vary with deformation in soft active materials undergoing large stretches. The influence of such stretch-dependent electromagnetic properties on the nonlinear dynamic response, resonance characteristics, and stability of electro-magneto-active circular membranes remains insufficiently explored. In particular, systematic comparisons of constant, linear, and nonlinear stretch-dependent electromagnetic models under both electric and magnetic loading are limited in the existing literature. This forms an important research gap addressed in the present thesis.

2.2.3 Taut domain formation in particle-reinforced EMAMs

Previous studies on taut-domain formation and membrane instability have mainly focused on homogeneous electroactive membranes. The combined influence of particle reinforcement and simultaneous electric and magnetic loading on the formation

and evolution of taut domains remains insufficiently investigated. In particular, the effects of filler volume fraction and filler-to-matrix shear modulus ratio on the stable taut region and critical actuation conditions of electro-magneto-active circular membranes have not been systematically examined. This represents a significant gap in understanding the stability limits of reinforced active membranes.

2.2.4 Stability and field-induced instabilities in biological membranes

The present study examines the combined effects of growth and fiber reinforcement on the dynamic behavior of biological membranes, which were not considered by Behera et al. [26]. Specifically, this work aims to explore the effects of such external coupling fields in the present contribution. Biological membranes, such as cell membranes, muscle cell membranes, and bilayer lipid membranes, may be represented as circular membranes, assuming certain geometrical properties. The current work uses the same methodology to suggest a dynamic model for circular biological membranes based on continuum physics considering growing instability.

2.3 Research objectives

The following research objectives are proposed to address the identified research gap and contribute significantly to the field of materials engineering:

- An analytical framework, employing the rule of mixtures to determine the effective shear modulus. This framework is utilized to analyze the impact of particle reinforcement on the nonlinear dynamic behavior of an electro-magneto-active circular membrane, with the dynamic equation formulated using the classical continuum mechanics approach.

- A framework to analyze the dynamics of deformation-dependent (linear and nonlinear) and independent (constant) permittivity and permeability on the

electromagnetic behavior of the circular membrane, with the dynamic equation formulated using the classical continuum mechanics approach.

- A framework based on the classical continuum mechanics approach that conducts a detailed parametric study to reveal the influence of particle reinforcement and shear modulus ratio on the taut domains of a smart thin circular membrane under electromagnetic loading.

- A framework for investigating the effect of isotropic and anisotropic growth, fiber reinforcement, and electric loading on the stability of biological membranes.

Chapter 3

Dynamics of Particle-Reinforced Circular EMAMs

Preface

Particle reinforcement plays a key role in improving the mechanical and dynamic performance of electro-magneto-active membranes. This chapter investigates the nonlinear dynamic response of particle-reinforced circular membranes under electrical and magnetic loading. The influence of reinforcement parameters on resonance, oscillations, chaos, and dynamic stability is examined using a continuum mechanics framework.

3.1 Introduction

EMAMs represent an important class of soft active materials that can undergo large and reversible deformations under the combined influence of electric and magnetic fields. Owing to their coupled field–mechanical response, these membranes exhibit highly nonlinear behavior, particularly under dynamic loading conditions. Such behavior includes large-amplitude oscillations, changes in excitation frequency, and transitions in stability. Understanding these nonlinear dynamic characteristics is essential for the effective design of smart devices such as soft actuators, adaptive membranes, and sensing systems.

Despite the growing interest in this area, most of the existing studies on the dynamic response of EMAMs have been limited to homogeneous or unreinforced material systems. The effect of particle reinforcement, which is commonly used in practical applications to enhance material performance, has not been sufficiently explored in the context of dynamic analysis. In particular, the influence of filler content and the stiffness contrast between filler and matrix on oscillatory behavior, frequency response, and stability characteristics remains largely unexplored. Furthermore, the combined effect of particle reinforcement and coupled electro–magneto-mechanical loading has not been systematically addressed in the literature.

In view of these limitations, the present chapter develops a continuum-based framework to study the nonlinear dynamic response of particle-reinforced EMAMs. The formulation explicitly accounts for key reinforcement parameters, such as filler volume fraction and shear modulus ratio, and examines their influence under combined electric and magnetic fields. Unlike earlier works, this study provides a detailed analysis of both time-domain and phase-space responses, enabling a clearer understanding of nonlinear oscillations and the conditions under which complex behaviors, including chaotic response, may arise.

Particle reinforcement plays a significant role in governing the dynamic behavior of elastomeric membranes. The presence of filler particles increases the effective stiffness of the material and restricts the mobility of polymer chains, thereby altering the deformation characteristics. As a result, important dynamic quantities such as vibration amplitude, natural frequency, and stability limits are directly affected. In electro–magneto-active systems, these particles also influence the interaction between the material and external fields, further modifying the overall response. Therefore, incorporating the effects of particle reinforcement is essential for a realistic and accurate analysis of EMAM dynamics. The specific objectives of this chapter are as follows:

- To develop a nonlinear dynamic model for particle-reinforced electro–magneto-active circular membranes.

- To examine the influence of filler volume fraction and shear modulus ratio on

the time-history and phase-space response.

- To investigate the effects of coupled electro–magneto-mechanical loading on nonlinear oscillations and stability behavior.

3.2 Mathematical formulation

Membranes exhibit inherently nonlinear elastic behavior when subjected to compressive transverse loading. The mechanical effects of such loading can be closely replicated by externally applied electric and magnetic fields, which generate Maxwell-type stresses acting through the membrane thickness and effectively mimic transverse pressure. This analogy allows electromagnetic fields to be treated as equivalent transverse loads in membrane models. Accordingly, this study formulates the nonlinear dynamics of an elastic, incompressible, particle-reinforced circular membrane subjected to transverse electric and magnetic fields, providing a unified framework for analyzing its coupled electromechanical and magnetomechanical response.

3.2.1 Assumptions

The formulation is developed based on the following assumptions:

- The membrane is modeled using membrane theory, and bending effects are neglected due to its small thickness.
- The material is assumed to be incompressible, such that the volume remains constant during deformation.
- The deformation is axisymmetric, and all field variables depend only on the radial coordinate and time.
- The applied electric field (V) and magnetic field (M) are uniform across the membrane thickness.

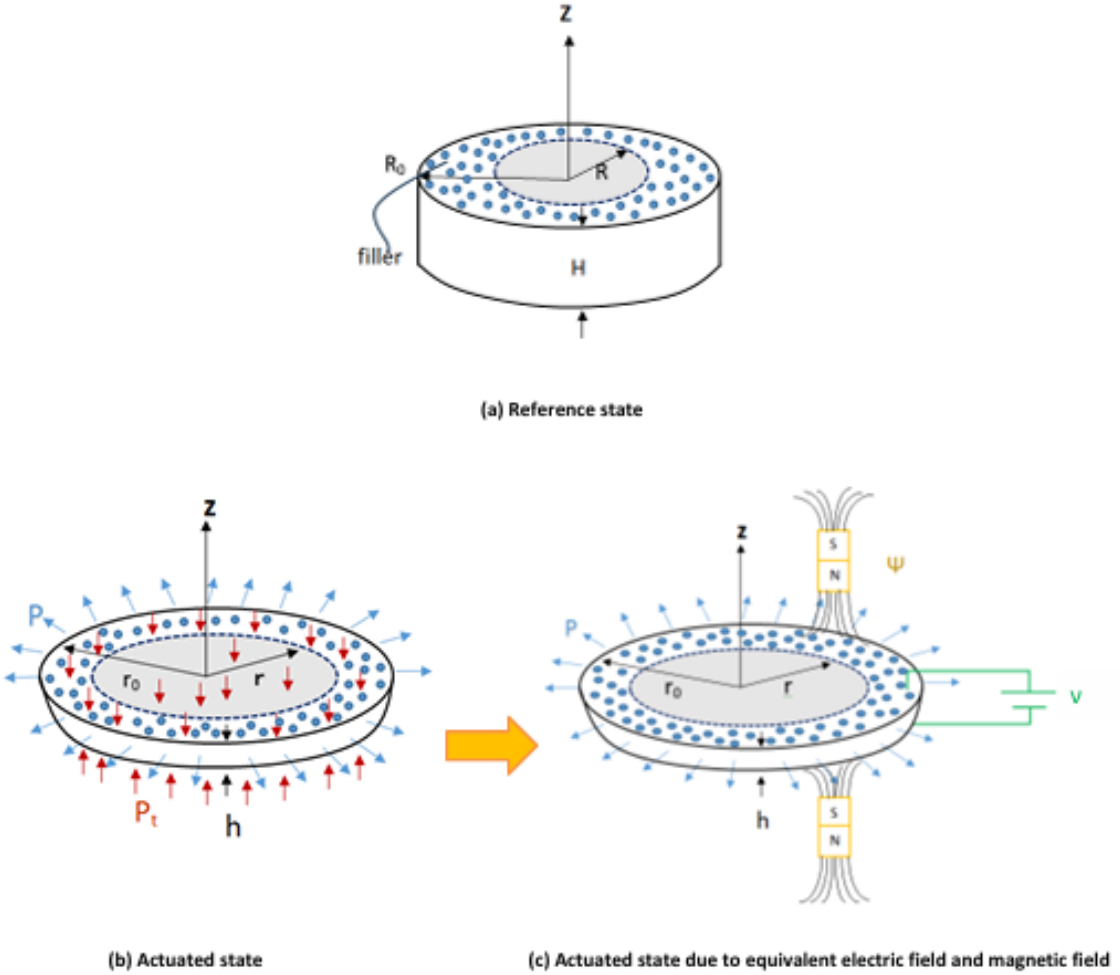


Figure 3.1: Schematic representation of the circular membrane: (a) Initial or reference state, (b) Deformed or actuated state caused by a radial load P and a uniformly applied transverse pressure P_t, and (c) Equivalent deformed state as in (b), achieved due to the application of a radial load, along with transverse electric and magnetic fields.

- The particle-reinforced material is treated as an effective homogeneous medium, where reinforcement effects are incorporated through the parameters Φ and μ_f/μ_m.

In this study, we consider a circular membrane with the coordinate systems (R, Θ, Z) in the reference state Ω_0 and (r, θ, z) in the current state Ω, respectively. Here, (R, r) denotes the radial coordinate, (Θ, θ) represents the circumferential direction, and (Z, z) corresponds to the thickness direction.

Under no-loading conditions, the membrane has an undeformed radius R_0 with a thickness H and is assumed to be axisymmetric and incompressible, with reinforcing particles as shown in Fig. 3.1(a). Under the applied load (electro-magneto field and tensile radial mechanical field), the membrane undergoes radial expansion and thickness contraction, resulting in a deformed radius r_0 and thickness h, as illustrated in Fig. 3.1(b). To finalize the framework, we impose a uniform external pressure P_t along the thickness direction. As previously mentioned, transverse pressure is commonly observed in many membranes. This pressure can be effectively substituted with electric and magnetic fields, which simulate a similar outcome by inducing electro-magneto-static pressure, as depicted in Fig. 3.1(c). The mapping χ identifies the electro-magneto-elastic deformation of the membrane, which is defined as:

$$\mathbf{x} = \chi(\mathbf{X}), \quad \chi : \Omega_0(R, \Theta, Z) \longrightarrow \Omega(r, \theta, z), \tag{3.1}$$

where the position vectors in the reference Ω_0 and the current Ω configurations are represented by $\mathbf{X}$ and $\mathbf{x}$, respectively. As a result, the corresponding deformation map for the membrane relating the deformed and undeformed variables is defined as:

$$r = \chi(R, t), \quad \theta = \Theta, \quad z = \chi(Z, t). \tag{3.2}$$

The deformation gradient tensor $\mathbf{F}$, the left Cauchy–Green deformation tensor $\mathbf{B}$, the electric field vector $\mathbf{E}$, and the magnetic field vector $\mathbf{H}$ for the given deformation map (3.1) are defined as:

$$\mathbf{F} = \begin{bmatrix} \lambda_r & 0 & 0 \\ 0 & \lambda_\theta & 0 \\ 0 & 0 & \lambda_z \end{bmatrix}, \quad \mathbf{B} = \mathbf{F}\mathbf{F}^T, \quad \mathbf{E} = \begin{bmatrix} 0 \\ 0 \\ E_0 \end{bmatrix}, \quad \mathbf{H} = \begin{bmatrix} 0 \\ 0 \\ H_0 \end{bmatrix}, \tag{3.3}$$

where E_0 and H_0 are the applied electric and magnetic field intensities on the membrane. λ_r, λ_θ, and λ_z are the principal stretch ratios in the radial, circumferential, and thickness directions, respectively. These are defined as:

- λ_r: ratio of deformed radial length to initial radial length,
- λ_θ: ratio of deformed circumferential length to initial circumferential length,

- λ_z: ratio of deformed thickness to initial thickness.

The principal stretches of an incompressible ($\lambda_r\lambda_\theta\lambda_z$=1) circular membrane experiencing equi-biaxial deformation are defined as:

$$\lambda_r = \lambda, \quad \lambda_\theta = \lambda, \quad \lambda_z = \frac{1}{\lambda^2}, \tag{3.4}$$

where $\lambda = \dfrac{r}{R}$ and $\lambda_z = \dfrac{h}{H}$, respectively. The invariants associated with the left Cauchy–Green deformation tensor $\mathbf{B}$, the electrical field-based pseudo structural tensor ($\mathbf{E}^l \otimes \mathbf{E}^l$), and the magnetic field-based pseudo structural tensor ($\mathbf{H}^l \otimes \mathbf{H}^l$) for an isotropic, incompressible, and electro-magneto-elastic deformation are defined as [69, 70]:

$$\begin{aligned} I_1 = \text{tr } \mathbf{B} = 2\lambda^2 + \frac{1}{\lambda^4}, \quad I_2 = \frac{1}{2}\left[(\text{tr } \mathbf{B})^2 - \text{tr } \mathbf{B}^2\right] = \lambda^4 + \frac{2}{\lambda^2}, \\ I_3 = \det \mathbf{B} = 1, \quad I_4 = \left[\mathbf{E}^l \otimes \mathbf{E}^l\right] : \mathbf{I} = \lambda^{-4}{E_0}^2, \quad I_5 = \left[\mathbf{E}^l \otimes \mathbf{E}^l\right] : \mathbf{B}^{-1} = {E_0}^2, \\ I_6 = \left[\mathbf{E}^l \otimes \mathbf{E}^l\right] : \mathbf{B}^{-2} = \lambda^4{E_0}^2, \quad I_7 = \left[\mathbf{H}^l \otimes \mathbf{H}^l\right] : \mathbf{I} = \lambda^{-4}{H_0}^2, \\ I_8 = \left[\mathbf{H}^l \otimes \mathbf{H}^l\right] : \mathbf{B}^{-1} = {H_0}^2, \quad I_9 = \left[\mathbf{H}^l \otimes \mathbf{H}^l\right] : \mathbf{B}^{-2} = \lambda^4{H_0}^2, \end{aligned} \tag{3.5}$$

where $\mathbf{E}^l = \mathbf{F}^T\mathbf{E}$, and $\mathbf{H}^l = \mathbf{F}^T\mathbf{H}$ represent the Lagrangian electric and magnetic field vectors in the reference configuration. In general, circular smart membranes exhibit limiting extensibility. For instance, the maximum stretch achievable in biaxial deformation is less than that in uniaxial deformation. Consequently, phenomenological models of such membranes account for their limited extensibility. The most popular model to replicate such materials is the Gent model [71].

3.3 Governing equation

In this work, we use the following Gent type of total strain energy density function W defined in terms of the above invariants I_1, I_5, and I_8 as:

$$W = -\frac{\mu_e}{2}J_m \log\left(1 - \frac{I_1 - 3}{J_m}\right) - \frac{\varepsilon_0}{2}(C_1 I_5) - \frac{\alpha_0}{2}(C_2 I_8), \tag{3.6}$$

where μ_e is the effective shear modulus defined as [68]: $\mu_e = \mu_m \left[1 + \frac{\Phi(\frac{\mu_f}{\mu_m} - 1)}{1 + \kappa(1-\Phi)(\frac{\mu_f}{\mu_m} - 1)} \right]$, J_m represents the chain extensibility parameter of the membrane material, C_1 and C_2 are the constant material parameters of the membrane, ε_0 and α_0 denote the electric permittivity and magnetic permeability of the free space. In the above-mentioned expression of effective shear modulus, Φ indicates the amount of fillers, μ_f and μ_m represent the associated shear moduli of the filler and matrix of the membrane, and κ denotes the parameter associated with the membrane Poisson's ratio. When referring to an incompressible elastomeric membrane, the value of κ is often taken to be 0.4 [20]. By following the theory of electro-magneto-elasticity [72], we may express the total Cauchy stress tensor $\mathbf{T}$, the electric displacement field $\mathbf{D}_e$, and the magnetic displacement field $\mathbf{D}_m$ for an incompressible and isotropic circular membrane, as follows:

$$\begin{aligned}\mathbf{T} = & -p\mathbf{I} + 2W_1\mathbf{B} + 2W_2\left(I_1\mathbf{B} - \mathbf{B}^2\right) - 2W_5\mathbf{E}\otimes\mathbf{E} - 2W_6\left(\mathbf{B}^{-1}\mathbf{E}\otimes\mathbf{E} + \mathbf{E}\otimes\mathbf{B}^{-1}\mathbf{E}\right) \\ & + 2W_8\left(\mathbf{BH}\otimes\mathbf{BH}\right) + 2W_9\left(\mathbf{BH}\otimes\mathbf{B}^2\mathbf{H} + \mathbf{B}^2\mathbf{H}\otimes\mathbf{BH}\right), \end{aligned} \tag{3.7a}$$

$$\mathbf{D}_e = -2\left(W_4\mathbf{B} + W_5\mathbf{I} + W_6\mathbf{B}^{-1}\right)\mathbf{E}, \tag{3.7b}$$

$$\mathbf{D}_m = -2\left(W_7\mathbf{B} + W_8\mathbf{B}^2 + W_9\mathbf{B}^3\right)\mathbf{H}. \tag{3.7c}$$

where p is a Lagrange multiplier to be obtained from the boundary conditions of incompressibility constraint and W_i is defined as $\frac{\partial W}{\partial I_i}$ for $i = 1, 2...9$. Substituting (3.6) in (3.7) with the use of (3.3), (3.4), and (3.5), we obtain the principal stress, electric displacement, and magnetic displacement components as:

$$T_{rr} = T_{\theta\theta} = -p + \frac{J_m\mu_e\lambda^2}{J_m - I_1 + 3}, \tag{3.8a}$$

$$T_{zz} = -p + \frac{J_m\mu_e\lambda^{-4}}{J_m - I_1 + 3} + C_1\varepsilon_0E_0^2 - C_2\alpha_0\lambda^{-8}H_0^2, \tag{3.8b}$$

$$D_{e3} = C_1\varepsilon_0E_0, \tag{3.8c}$$

$$D_{m3} = C_2\alpha_0\lambda^{-8}H_0. \tag{3.8d}$$

In Eqs. 3.8(c-d), $C_1 = \varepsilon_r$ denotes the relative electric permittivity and $C_2 = \alpha_r$ represents the relative magnetic permeability of the membrane. By implementing the

specified traction-free boundary condition $T_{zz} = 0$ in Eq. 3.8(b), we obtain the radial and hoop stress components from Eq. 3.8(a) as:

$$T_{rr} = T_{\theta\theta} = \frac{\mu_e J_m \left(\lambda^2 - \lambda^{-4}\right)}{J_m - I_1 + 3} - \varepsilon_r \varepsilon_0 E_0^2 + \alpha_r \alpha_0 \lambda^{-8} H_0^2. \tag{3.9}$$

In the absence of electric and magnetic fields, the stress tensor can be derived from relation (3.7) and is given by:

$$\mathbf{T} = -pI + 2W_1\mathbf{B} + 2W_2[I_1\mathbf{B} - \mathbf{B}^2]. \tag{3.10}$$

To express the principal stress components for this case, we can derive them directly from Eq. 3.10 as follows:

$$T_{rr} = T_{\theta\theta} = -p + \frac{J_m \mu_e \lambda^2}{J_m - I_1 + 3}, \tag{3.11a}$$

$$T_{zz} = -p + \frac{J_m \mu_e \lambda^{-4}}{J_m - I_1 + 3}. \tag{3.11b}$$

It is important to note that $\mathbf{T}$ here excludes the electro-magneto-mechanical stress. Given the uniform transverse stress at the boundary, $T_{zz} = -P_t$, the Lagrange multiplier p can be determined as:

$$p = P_t + \frac{J_m \mu_e \lambda^{-4}}{J_m - I_1 + 3}. \tag{3.12}$$

Upon invoking the above expression of p in Eq. 3.11(a), we obtain the radial and hoop stress components as:

$$T_{rr} = T_{\theta\theta} = \frac{\mu_e J_m \left(\lambda^2 - \lambda^{-4}\right)}{J_m - I_1 + 3} - P_t \tag{3.13}$$

By comparing the stress expressions from Eqs. (3.9) and (3.13), we can conclude that: $P_t = \left|P_{t_{elect.}} + P_{t_{mag.}}\right| = \varepsilon_r \varepsilon_0 E_0^2 - \alpha_r \alpha_0 H_0^2$. Here, $E_0 = (\frac{\upsilon}{h}) = \lambda^2(\frac{\upsilon}{H})$ and $H_0 = (\frac{\Psi}{h}) = \lambda^2(\frac{\Psi}{H})$, where υ and Ψ are the applied voltage and magnetic flux. Therefore, $P_T = \left|P_{T_{elect.}} + P_{T_{mag.}}\right|$, and $P_t = \lambda^4 P_T$.

The equilibrium equation of motion for an axisymmetric deformation in incompressible and isotropic elastic circular membrane is given as:

$$\frac{dT_{rr}}{dr} + \frac{T_{rr} - T_{\theta\theta}}{r} + \rho b_f = \rho \frac{d^2 r}{dt^2}, \tag{3.14}$$

where $\nabla.(.)$, ρ, and b_f represent the divergence operator, density of the membrane material, and the body force per unit volume. For a given boundary condition $T_{rr}(r = r_0) = \frac{P}{2\pi r_0 h}$ with no body force $b_f = 0$, we may radially balance the equilibrium equation (3.14) with the use of (3.9) as:

$$\frac{P}{2\pi r_0 h} - T_{rr} = \int_0^{r_0} \rho \frac{d^2 r}{dt^2}\, dr \Rightarrow \frac{d^2\lambda}{dt^2} + \frac{2T_{rr}}{\lambda\rho R_0^2} - \frac{P}{\pi r_0 h \lambda \rho R_0^2} = 0. \tag{3.15}$$

Substituting T_{rr} from Eq. (3.9) in Eq. (3.15), we obtain the governing equation of the membrane as:

$$\frac{d^2\lambda}{d\tau^2} + \frac{J_m U(\lambda - \lambda^{-5})}{\left(J_m - 2\lambda^2 - \frac{1}{\lambda^4} + 3\right)} - \lambda^3 V^2 + \lambda^{-5} M^2 - S = 0, \tag{3.16}$$

where $U = \left[1 + \frac{\Phi(\frac{\mu_f}{\mu_m} - 1)}{1 + \kappa(1-\Phi)(\frac{\mu_f}{\mu_m} - 1)}\right]$ represents the normalized effective shear modulus, $\tau = \frac{\sqrt{2}t}{R_0\sqrt{\frac{\rho}{\mu_m}}}$ is the dimensionless time, $S = \frac{P}{2\pi\mu_m R_0 H}$ is the nominal equal-biaxial normalized stress at the boundary, $V = \frac{v}{H\sqrt{\frac{\mu_m}{\varepsilon_0\varepsilon_r}}} = \sqrt{\frac{P_{Telec.}}{\mu_m}}$ is the normalized voltage, $M = \frac{\Psi}{H\sqrt{\frac{\mu_m}{\alpha_0\alpha_r}}} = \sqrt{\frac{P_{Tmag.}}{\mu_m}}$ is the normalized flux.

Eq. 3.16 is a fully non-dimensional form, which allows the combined effects of mechanical loading, electric field, magnetic field, and material parameters to be analyzed in a unified manner. Physical interpretation of each term in the above equation is expressed as follows:

- Inertia term $\left(\frac{d^2\lambda}{d\tau^2}\right)$: It represents the dynamic response of the system and governs time-dependent oscillations.
- Elastic contribution $\left(\frac{J_m U(\lambda - \lambda^{-5})}{J_m - 2\lambda^2 - \frac{1}{\lambda^4} + 3}\right)$: This term arises from the Gent strain energy model and captures nonlinear elasticity. It acts as a restoring force and is significantly influenced by particle reinforcement.

- Electric force term ($\lambda^3 V^2$): It represents the effect of the applied electric field. It tends to expand the membrane in-plane due to Maxwell stress.
- Magnetic force term ($\lambda^{-5} M^2$): It accounts for magnetic field-induced stresses, which modify the deformation depending on field strength.
- External loading term (S): It corresponds to the normalized mechanical stress applied at the boundary.

Based on the findings of [73], we reaffirm that the normalized voltage V and magnetic flux M can effectively be substituted with normalized transverse pressure to achieve an equivalent impact on the dynamical system. This equivalence allows us to treat normalized voltage and flux as normalized transverse pressure, as illustrated in Fig. 3.1(c). Therefore, the normalized voltage and flux are interchangeable with normalized transverse pressure, providing a consistent approach for analyzing the dynamical system's behavior. The dynamic behavior of the membrane undergoing equi-biaxial electro-magneto-elastic deformation is elucidated by the ensuing governing equation:

$$\frac{d^2\lambda}{d\tau^2} + g(\lambda; U, V, M, S) = 0, \tag{3.17}$$

where $g(\lambda; U, V, M, S) = \dfrac{J_m U(\lambda - \lambda^{-5})}{(J_m - 2\lambda^2 - \lambda^{-4} + 3)} - \lambda^3 V^2 + \lambda^{-5} M^2 - S.$

3.3.1 Numerical solution procedure

The nonlinear governing equation is solved numerically in MATLAB using the `ode45` solver, which employs an adaptive Runge–Kutta (4, 5) scheme. The simulations are performed using the initial conditions as:

$$\lambda(0) = 1, \qquad \dot{\lambda}(0) = 0. \tag{3.18}$$

Since `ode45` automatically adjusts the integration step according to the response of the system, a fixed time increment is not prescribed. The computed solution is evaluated at 10,000 equally spaced time points for plotting and post-processing. A dimensionless

simulation time of $\tau = 20$ is used for the regular dynamic responses and phase trajectories. For the chaotic response and Poincaré analysis, the simulation is extended to $\tau = 400$ to examine the long-term response of the membrane.

For the frequency-response analysis, the normalized excitation frequency is varied from 0 to 2 with an increment of 0.1. At each frequency, the oscillation amplitude is evaluated as:

$$A = \frac{\lambda_{\max} - \lambda_{\min}}{2}. \tag{3.19}$$

The Poincaré section is constructed by sampling the stretch λ and stretch rate $\dot{\lambda}$ once during each excitation period,

$$T = \frac{2\pi}{\omega}. \tag{3.20}$$

No separate transient-removal procedure is applied in the present numerical implementation; instead, the longer simulation duration is used to examine the long-term nonlinear response. No user-defined solver tolerances are specified, and therefore the standard adaptive error-control settings of `ode45` are used.

3.4 DC dynamic response

In this section, the DC dynamic characteristics of the membrane are evaluated. Specifically, in the governing Eq. (3.17), there are two state variables λ and $\frac{d\lambda}{d\tau}$ and the corresponding initial conditions of these state variables at $\tau = 0$ are given as: $(\lambda)_{\tau=0} = 1$; $\left(\frac{d\lambda}{d\tau}\right)_{\tau=0} = 0$. A parametric study is carried out utilizing the time-independent normalized voltage, denoted as V, to evaluate the effect of the amount of filler ($\Phi = 0.01$, 0.05, 0.10 and 0.20), shear modulus ratio ($\mu_f/\mu_m = 1$, 10, and 100), normalized stress ($S = 1$, 3, and 5), applied normalized voltage ($V = 0.25$, 0.50, and 0.75) and magnetic flux ($M = 0.25$, 0.50, and 0.75) on the nonlinear dynamic response of the membrane.

First, we plotted the time-history plots and phase diagrams to investigate the effects of the amount of filler Φ (Figs. 3.2(a, c)) and shear modulus ratio μ_f/μ_m (Figs. 3.2(b, d)) on the nonlinear oscillatory behavior of the membrane. The time-history

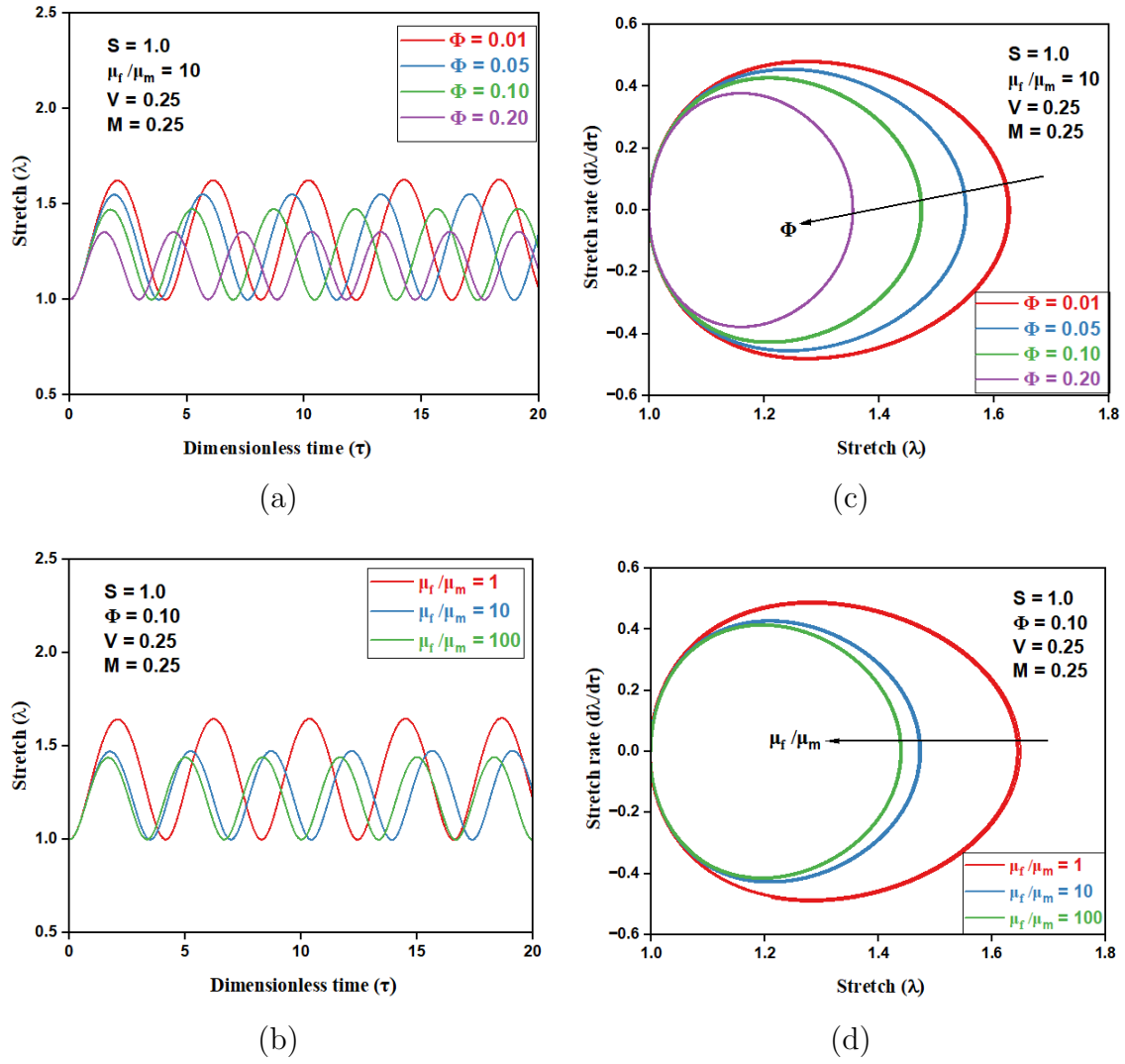
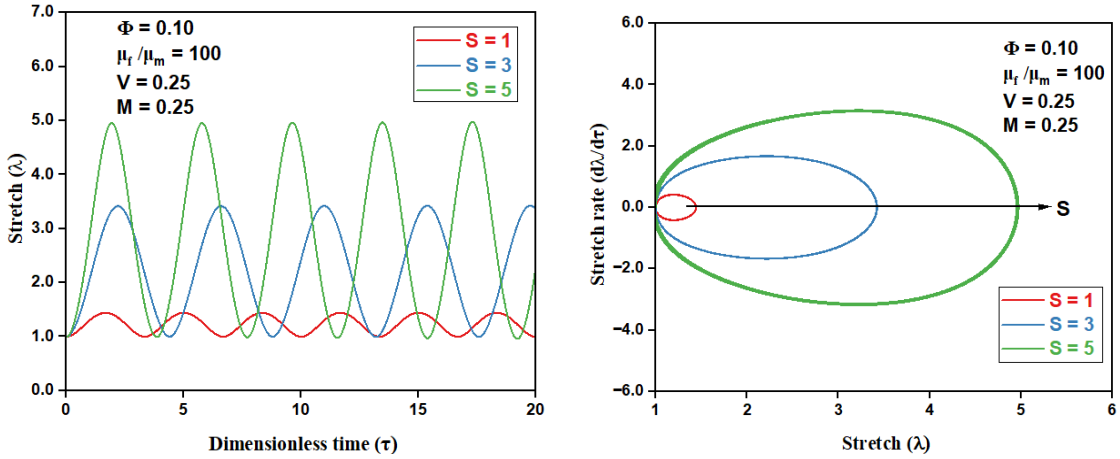


Figure 3.2: DC dynamic responses of the membrane with (a-b) time evolution diagrams, and (c-d) phase diagrams for the different amounts of filler (Φ), and shear modulus ratio (μ_f/μ_m).

data reveal that the system consistently exhibits stable oscillations around a steady equilibrium stretch for all the considered levels of filler and shear modulus ratio (Figs. 3.2a-b). Furthermore, the amplitude of these steady oscillations decreases as Φ and μ_f/μ_m increase. From Figs. 3.2(c-d), it is observed that the trajectories in a phase portrait decrease with an increase in the amount of filler and shear modulus ratio. This indicates that the membrane is undergoing smaller deformations or strains with the increase in values of Φ and μ_f/μ_m. This behavior is attributed to the fact that the



(a) (b)

Figure 3.3: DC dynamic responses of the membrane with (a) time evolution diagrams, and (b) phase diagrams for different levels of normalized stress (S).

particle reinforcement acts like supporting columns, thereby preventing membrane thinning and reducing overall deformation. Additionally, an increase in the shear modulus ratio strengthens the membrane, further minimizing thinning and overall deformation.

Next, Fig. 3.3 shows the effect of normalized stress S utilizing the time-history and phase-portrait diagrams. Fig. 3.3(a) signifies that the membrane shows stable oscillations around a steady equilibrium stretch for all the considered levels of normalized stress. The amplitude of these steady oscillations increases with an increase in normalized stress value. The phase trajectory in Fig. 3.3(b) becomes larger as the normalized stress S increases. This corresponds to a greater range of stretch and a higher stretch rate during the simulated response. The time histories in Fig. 3.3(a) show the same increase in the oscillation amplitude.

Finally, Fig. 3.4 shows the evaluated effects of applied normalized magnetic flux M and voltage V on the nonlinear dynamic behavior of the membrane. Figs. 3.4 (a, c) show that increasing the normalized magnetic loading M reduces the oscillation amplitude and the extent of the phase trajectory for the parameters considered. In the present model, the magnetic loading modifies the magneto-mechanical restoring response and the effective stiffness of the coupled membrane system, thereby reducing

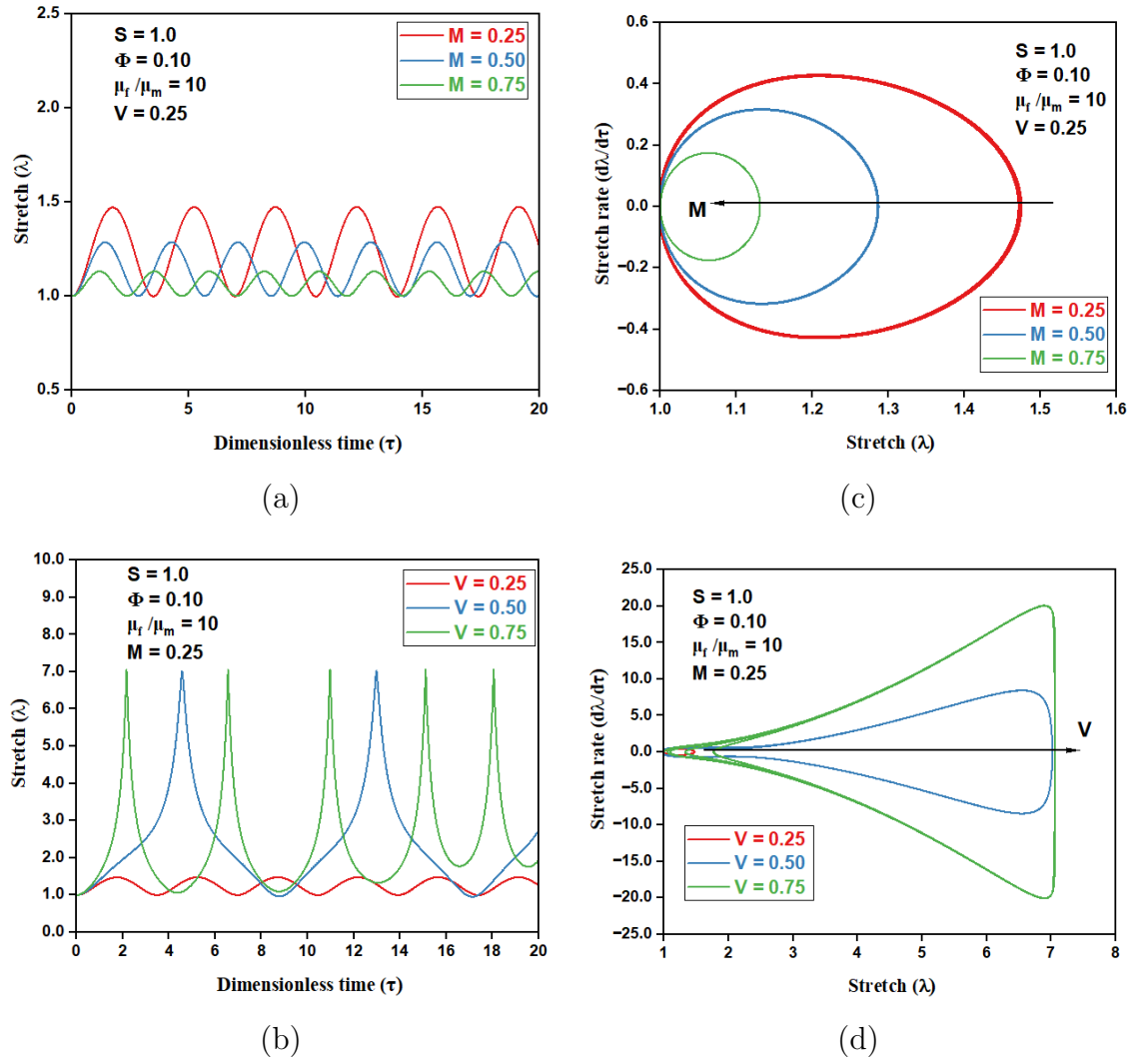


Figure 3.4: DC dynamic responses of the membrane with (a–b) time evolution diagrams, and (c-d) phase diagrams for different levels of applied dimensionless voltage (V), and magnetic flux (M).

the oscillation amplitude for the considered parameters.

Figs. 3.4(b, d) show that increasing the normalized voltage V increases the oscillation amplitude and the range of stretch and stretch rate. This trend is consistent with the larger electric contribution in the governing equation, leading to more significant deformation and dynamic behavior. Interpretation and trend patterns of the parameters are illustrated as follows:

- Effect of filler volume fraction (Φ): From Figs. 3.2(a, c), it can be clearly seen

that as Φ increases, the amplitude of oscillations decreases. This behavior is expected because adding more filler particles makes the material stiffer. The particles restrict the movement of polymer chains, which reduces the ability of the membrane to deform freely. As a result, the oscillations become smaller. The phase diagrams also reflect this trend, where the loops become tighter with increasing Φ, indicating reduced motion and improved stability.

- Effect of shear modulus ratio (μ_f/μ_m): From Figs. 3.2(b, d), similar to the filler fraction, increasing μ_f/μ_m reduces the oscillation amplitude. This is because a higher modulus ratio means the filler particles are much stiffer compared to the matrix. As a result, the overall material becomes more rigid and resists deformation more strongly. This behavior is consistent with what is generally observed in reinforced composite materials.

- Effect of magnetic field (M): From Figs. 3.4(a, c), the results indicate that the magnetic field interacts with the material and changes its effective stiffness and reduces the oscillation.

- Effect of electric field (V): From Figs. 3.4(b, d), as the voltage increases, the oscillation amplitude also increases. This can be understood from the fact that the electric field generates Maxwell stress, which actively deforms the membrane. In other words, the electric field supplies energy to the system, leading to larger oscillations.

3.5 Chaotic behavior on enhancing field and particle content

The electro–magneto-active circular membrane exhibits complex nonlinear dynamics under combined mechanical, electrical, and magnetic loading. Among these responses, chaotic behavior arises due to the strong nonlinear nature of the system and the interaction between multiple coupled physical fields.

The complexity of analyzing a circular membrane increases significantly when the applied voltage fluctuates over time. A system's changing dynamics could display unpredictable chaos, leading to the examination of the membrane. This complexity encourages a detailed investigation of membrane dynamics, taking into account time-dependent voltage. Specifically, the membrane is excited by time-dependent AC electric voltage of a harmonic nature given by [74, 75]:

$$V = v_a \sin(\omega\tau), \tag{3.21}$$

where the term V represents the normalized voltage, v_a denotes the magnitude of the applied AC voltage, ω denotes the dimensionless angular excitation frequency and is given by $\omega = \frac{2\pi}{\tau}$, where τ is the dimensionless time period of oscillation. Thus, the governing equation (3.17) for the applied AC voltage may be rewritten as:

$$\frac{d^2\lambda}{d\tau^2} + \frac{J_m U(\lambda - \lambda^{-5})}{(J_m - 2\lambda^2 - \lambda^{-4} + 3)} - \lambda^3 (v_a \sin(\omega\tau))^2 + \lambda^{-5} M^2 - S = 0. \tag{3.22}$$

Chaos in the present system is primarily caused by the following factors:

i. Material nonlinearity: The membrane is modeled using the Gent hyperelastic model, which introduces strong nonlinear stiffness, especially at large stretches. This leads to non-proportional restoring forces.

ii. Geometric nonlinearity: Large deformation of the membrane results in nonlinear strain–displacement relations, further contributing to system nonlinearity.

iii. Electro–magneto–mechanical coupling: The applied electric and magnetic fields generate Maxwell-type stresses that depend on deformation. As deformation evolves, the electromagnetic forces also change, creating a bidirectional nonlinear coupling between fields and mechanics.

iv. Particle reinforcement effects: The presence of filler particles modifies the effective stiffness and enhances nonlinear interactions, influencing energy transfer within the system.

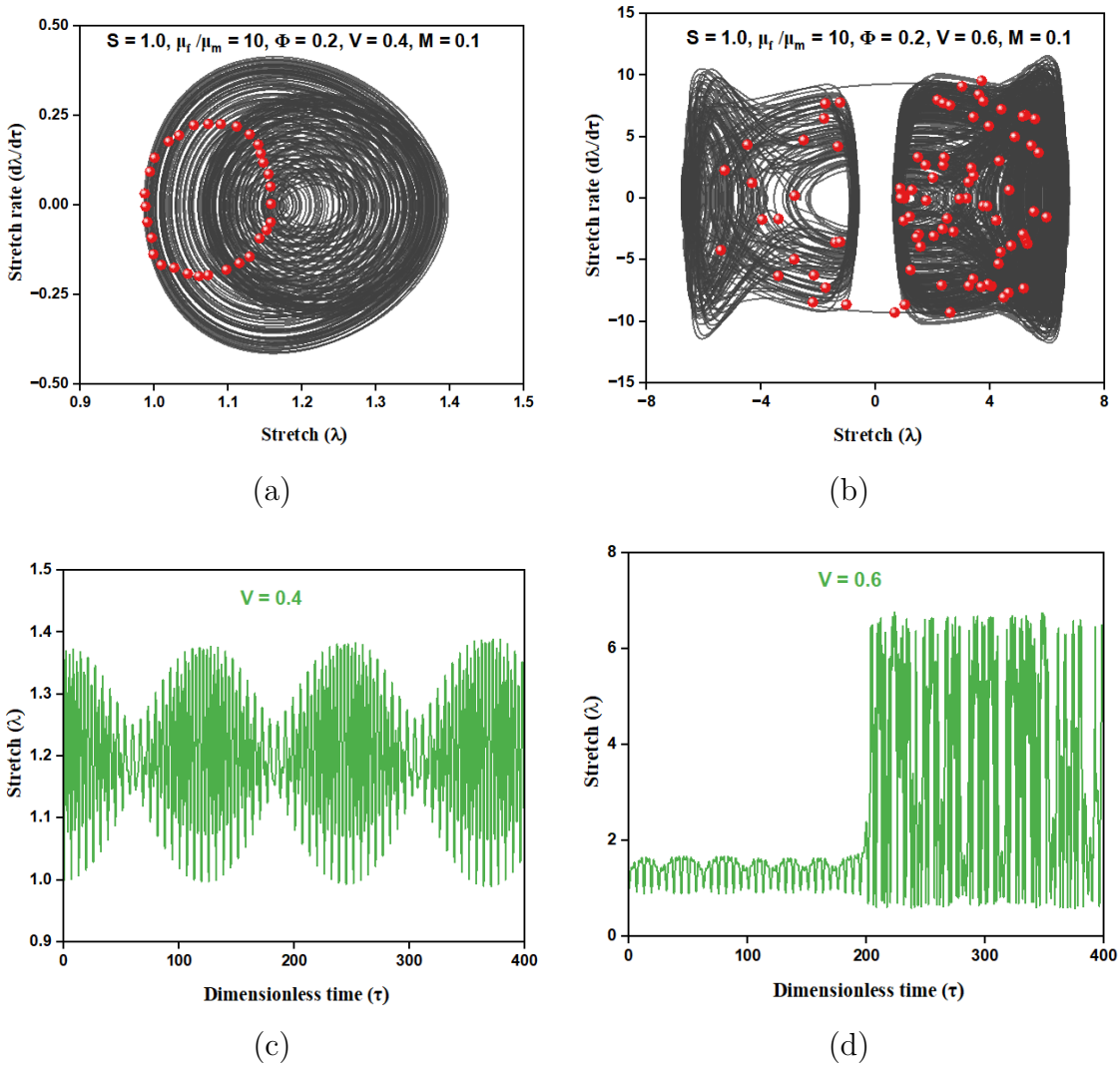


Figure 3.5: AC dynamic responses of the membrane with (a–b) phase diagrams merged with Poincaré plots, and (c-d) time-history plots at the excitation frequency, $\omega = 0.50$ for different voltages at V = 0.4 and 0.6.

The system is subjected to time-dependent (AC) excitation, which continuously supplies energy to the membrane. Because of the nonlinear coupling in the system, the deformation of the membrane changes its electromagnetic properties, such as permittivity and permeability, and these altered properties, in turn, affect the forces acting on the membrane. This creates a continuous feedback loop where deformation and electromagnetic forces influence each other. At certain excitation frequencies and amplitudes, this interaction leads to resonance, a gradual loss of regular oscillation

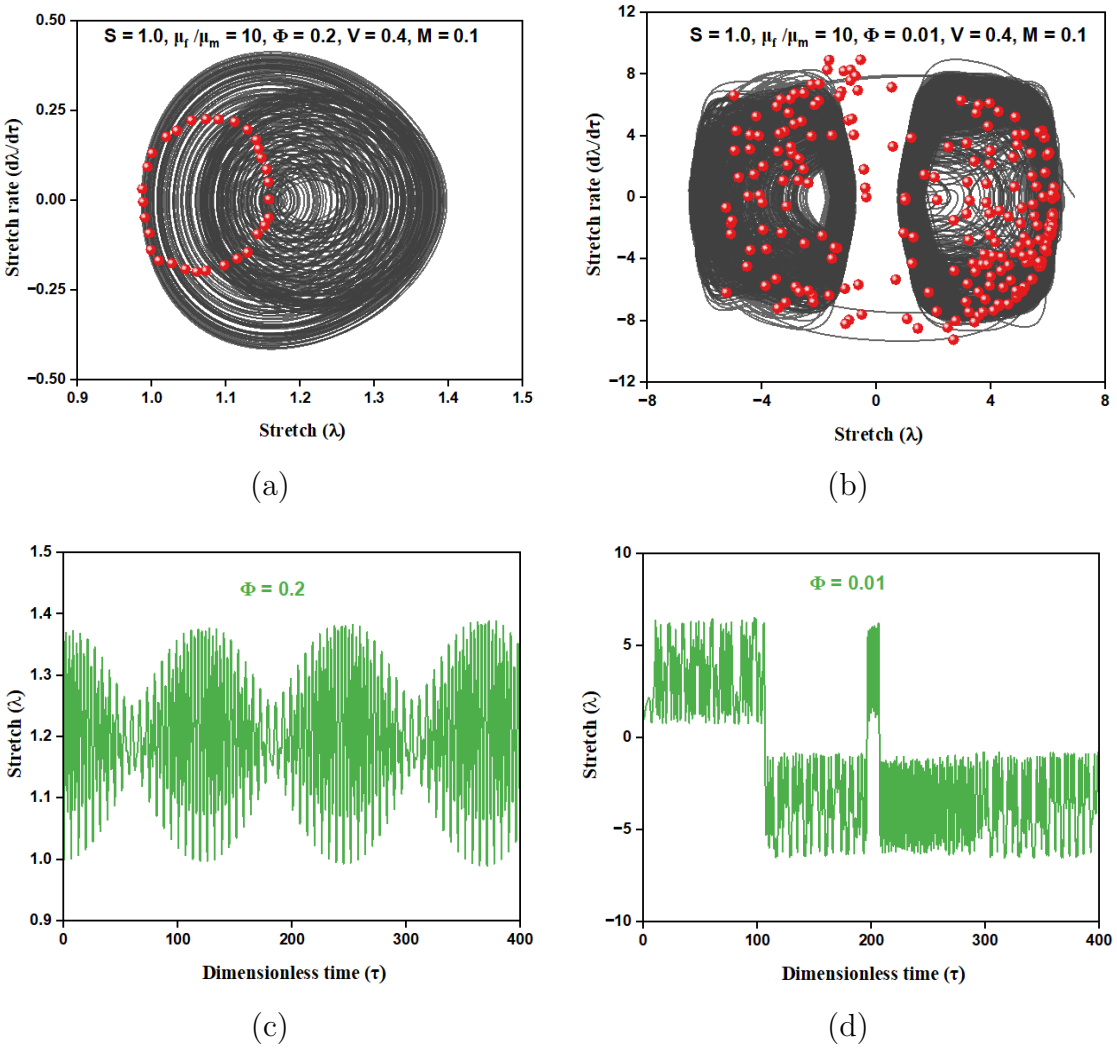


Figure 3.6: AC dynamic chaotic responses of the membrane with (a–b) phase diagrams merged with Poincaré plots, and (c-d) time evolution diagrams corresponding to the excitation frequency, $\omega = 0.50$ and voltage, $V = 0.4$ for different amounts of filler at $\Phi = 0.2$ to 0.01.

patterns, and eventually irregular motion. As a result, the system moves from a predictable and stable response to a highly sensitive and non-repeating behavior, which is typical of chaotic systems.

As system parameters such as applied voltage or particle content are varied, the dynamic response evolves through distinct stages:

- Periodic Response: At low excitation levels, the system oscillates with a single

dominant frequency. The motion is regular and repeatable, and phase trajectories appear as a single point or a set of finite points.

- Quasi-Periodic Response: With an increase in excitation or nonlinear effects, multiple incommensurate frequencies emerge. The motion becomes more complex, and phase trajectories form a closed curve.

- Chaotic Response: Beyond a critical threshold, the interaction of nonlinearities and excitation leads to a breakdown of regular motion. The system exhibits sensitive dependence on initial conditions, and phase trajectories become irregular and non-repeating, indicating chaos.

It is important to distinguish these dynamic responses from bounded oscillation and static stability. A bounded oscillation simply means that the stretch remains within a finite range with time and does not necessarily imply periodic motion. Static stability, on the other hand, refers to the stability of an equilibrium configuration and is different from the periodic, quasi-periodic, or chaotic nature of the time-dependent response.

We have investigated the effect of the applied electric field (Fig. 3.5) and filler (Fig. 3.6) on the chaotic behavior of the membrane. The parameters under consideration are $\Phi = 0.2$, $\omega = 0.50$, and $S = 1$. When the voltage parameter V is set to 0.4, the system exhibits quasi-periodic behavior, as evidenced by the closed nature of the Poincaré curve (Fig. 3.5a). This is further supported by the distinct appearance of beat patterns in the time-history response (Fig. 3.5c). However, as V increases from 0.4 to 0.6 at the same excitation frequency, the Poincaré plot (Fig. 3.5b) displays an uncountable number of points, indicating the onset of chaotic oscillations. Additionally, the time-history response (Fig. 3.5d) reveals irregular behavior, further confirming the presence of chaos. Reducing the filler volume fraction from $\Phi = 0.2$ to 0.01 produces a larger oscillation amplitude and a more dispersed set of Poincaré points for the parameters shown in Fig. 3.6. These observations describe a change in the simulated motion; they do not provide a direct measure of the membrane's energy.

It is essential to highlight that these phenomena are specific to the values considered

in this analysis and are significantly influenced by other system parameters, such as the shear modulus ratio μ_f/μ_m, the normalized stress S, and the level of normalized magnetic flux M.

3.6 Summary

This chapter presents a continuum-mechanics-based modeling framework to explore the intricate nonlinear behavior of a circular membrane excited by a combination of electro-magneto-mechanical loadings. To facilitate a qualitative examination of this system, the traditional approach of applying transverse pressure on the membrane is substituted with the corresponding electric and magnetic fields. The investigation focuses on a nonlinear differential equation that describes the radial axisymmetric motion of the circular membrane. From this equation, several key insights are derived, shedding light on the complex interplay of forces and the dynamic behavior of the membrane. The following are the key inferences obtained from the present study:

i. In DC dynamics, the amplitude of steady oscillations decreases with an increase in the amount of fillers and shear modulus ratio. This is due to the fact that the particle reinforcement acts like supporting columns, thereby preventing membrane thinning and reducing overall deformation. Additionally, an increase in the shear modulus ratio strengthens the membrane, further minimizing thinning and overall deformation.

ii. In DC dynamics, the amplitude of steady oscillations decreases on enhancement in magnetic flux while there is an increase in trend on increasing pre-stress and normalized voltage from the time history plot. The energy of the system decreases on increasing flux and increases on enhancing pre-stress and normalized voltage which affects the stability of membrane.

iii. In AC dynamics, it has been observed that when the voltage increases from 0.4 to 0.6 and the amount of fillers is reduced from 0.2 to 0.01 at the excitation frequency, the Poincaré plot displays an uncountable number of points, indicating

the onset of chaotic oscillations with irregular behavior in time history.

The results show that as the filler content and shear modulus ratio increase, the membrane becomes stiffer, which naturally reduces its deformation. At the same time, applying higher electric and magnetic fields improves the actuation response, but it also makes the system more prone to instability. As the level of excitation increases, the membrane response gradually shifts from a regular, periodic motion to a more complex and chaotic behavior. Overall, the system response is mainly controlled by the nonlinear interaction between the mechanical deformation and the applied electromagnetic forces.

These results are useful from a practical design point of view, as they show that adding reinforcement can help control vibrations and make the membrane more stable. At the same time, electric and magnetic fields offer a simple way to adjust and control the response of the system when needed. Understanding how the membrane behaves at different frequencies also helps in avoiding resonance, which could otherwise lead to large deformations or failure. Overall, these insights can be directly applied in the design of smart membranes, soft actuators, and other adaptive systems where a controlled and reliable response is important.

In this chapter, the focus was on understanding how particle reinforcement and external electric and magnetic fields influence the dynamic response of the membrane. However, throughout the analysis, the electromagnetic properties were assumed to remain constant. In reality, this is not always the case. As the membrane deforms, properties such as electric permittivity and magnetic permeability can change with stretch, which in turn affects the overall system behavior. To account for this, the next chapter builds on the present work by incorporating stretch-dependent electromagnetic properties into the model. Different representations, namely constant, linear, and nonlinear models, are considered to examine how these variations influence the response of the membrane. The analysis is carried out under both DC and AC loading conditions, with particular attention to changes in deformation, energy response, resonance behavior, and stability. This provides a more realistic understanding of the coupled electro–magneto–mechanical behavior of the system.

Chapter 4

Stretch-Dependent Electromagnetic Properties and Dynamic Response

Preface

The electromagnetic properties of soft active materials often vary with deformation, affecting their overall response. This chapter incorporates stretch-dependent electrical permittivity and magnetic permeability into the constitutive model. The influence of different material models on the dynamic behavior, resonance characteristics, and stability of electro-magneto-active membranes is systematically investigated.

4.1 Introduction

The dynamic response of soft active materials is governed by strong coupling between mechanical deformation and electromagnetic fields. While electric permittivity and magnetic permeability are often treated as constants, this assumption becomes inadequate for soft elastomers undergoing large deformations, where microstructural reorganization leads to deformation-dependent electromagnetic properties.

Although considerable research has been carried out on electroactive and magnetoactive soft materials, most existing studies assume that electric permittivity and magnetic permeability remain constant during deformation. In reality, these properties change with stretch because of the internal rearrangement of the polymer network

and embedded particles. Ignoring these deformation-dependent effects can lead to inaccurate predictions of the dynamic response and stability of soft active membranes, especially under large deformation and time-dependent loading. In addition, only limited studies have examined the combined influence of stretch-dependent electric and magnetic properties on the behavior of electro-magneto-active circular membranes under both DC and AC excitations.

The main novelty of this chapter is the development of a continuum-based model that incorporates stretch-dependent electric permittivity and magnetic permeability into the dynamic analysis of electro-magneto-active circular membranes. Unlike conventional studies that consider constant electromagnetic properties, this work investigates constant, linear, and nonlinear models and compares their influence on the membrane response, resonance behavior, and stability characteristics. The main objectives of this chapter are as follows:

- To develop governing equations considering stretch-dependent electric permittivity and magnetic permeability.
- To study the effect of constant, linear, and nonlinear electromagnetic models on the DC and AC dynamic response of the membrane.
- To examine the influence of stretch-dependent electromagnetic properties on resonance behavior and stability characteristics of the system.

An energy-based constitutive framework is adopted in which electromagnetic properties are introduced as explicit functions of stretch, allowing consistent coupling between elastic deformation and field-induced Maxwell stresses.

4.2 Mathematical formulation

This section formulates the dynamics of an elastic, incompressible circular membrane considering constant and stretch-dependent (linear and nonlinear) variations of the permittivity and permeability.

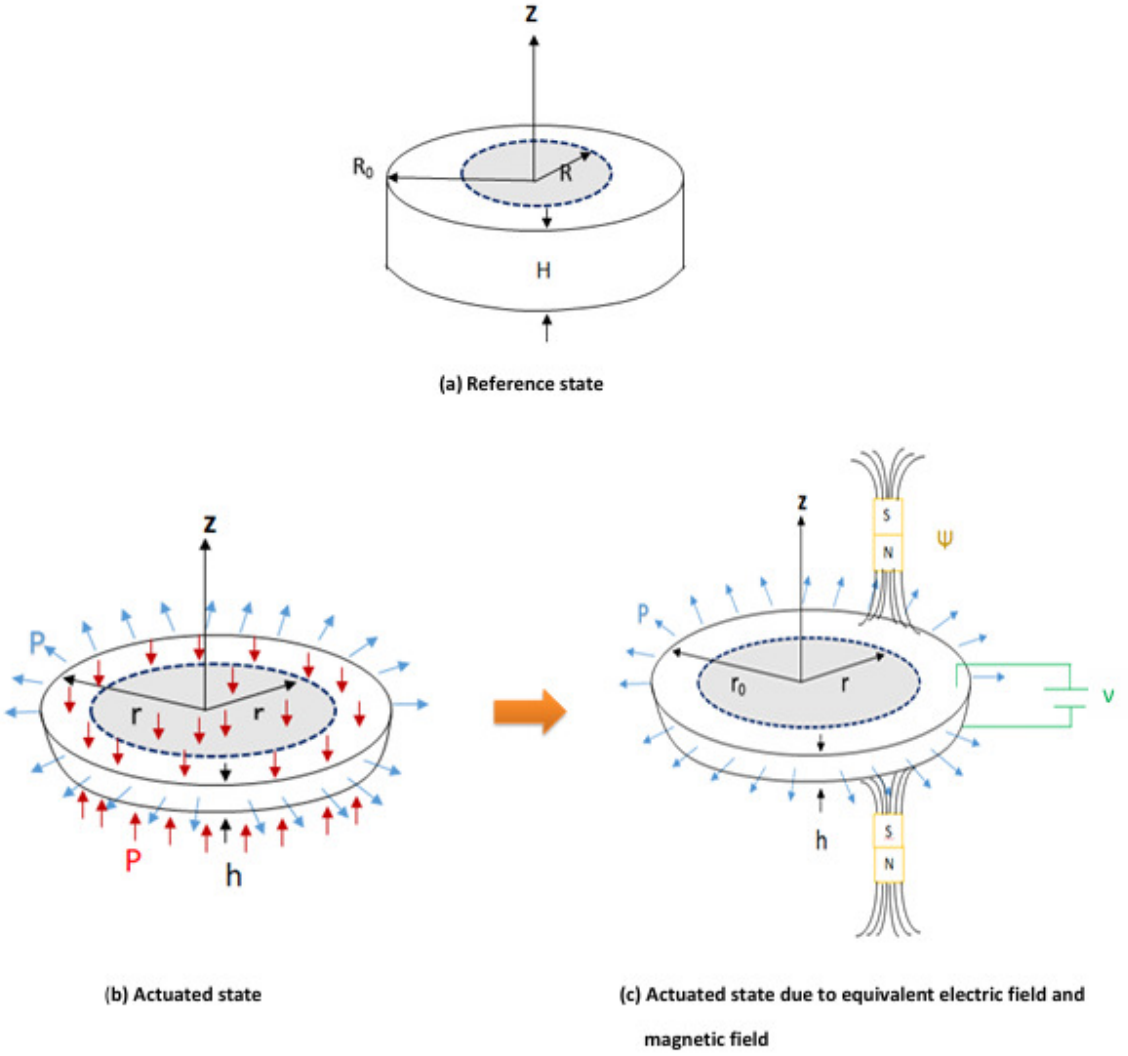


Figure 4.1: Schematic representation of the circular membrane: (a) Initial or reference state, (b) Deformed or actuated state caused by a radial load P and a uniformly applied transverse pressure P_t, and (c) Equivalent deformed state as in (b), achieved due to the application of a radial load, along with transverse electric and magnetic fields.

The present model assumes that the electro-magneto-active circular membrane is homogeneous, isotropic, and hyperelastic in nature. The membrane undergoes large elastic deformation and is considered incompressible. Since the membrane thickness is very small compared to its in-plane dimensions, bending effects are neglected. Uni-

form electric and magnetic fields are applied across the membrane thickness, and the deformation is assumed to be axisymmetric. Stretch-dependent electric permittivity and magnetic permeability are incorporated in the formulation, while thermal effects, body forces, and material damping are neglected.

In this study, we examine a circular membrane using two coordinate systems: (R, Θ, Z) for the reference state, β_0, and (r, θ, z) for the deformed state, β. The membrane has an initial radius R_0 and thickness H, and is assumed to be axisymmetric and incompressible, as shown in Fig. 4.1(a). When subjected to external forces, the membrane expands radially while its thickness reduces, resulting in a new radius r_0 and a thinner profile h, as illustrated in Fig. 4.1(b). To complete the model, we apply a uniform external pressure, P_t, along the membrane's thickness. This type of transverse pressure is frequently encountered in membranes, and it can be substituted by external fields, which create a similar effect by generating electro-magneto-static pressure, as shown in Fig. 4.1(c). The mapping ζ characterizes the electro-magneto-elastic deformation of the membrane, defined as:

$$\mathbf{x} = \zeta(\mathbf{X}), \quad \zeta : \beta_0(R, \Theta, Z) \longrightarrow \beta(r, \theta, z), \tag{4.1}$$

Here, the position vectors for the reference configuration β_0 and the current configuration β are denoted by $\mathbf{X}$ and $\mathbf{x}$, respectively. Consequently, the deformation mapping that links the undeformed and deformed states of the membrane can be expressed as follows:

$$r = \zeta(R, t), \quad \theta = \Theta, \quad z = \zeta(Z, t). \tag{4.2}$$

The deformation gradient tensor $\mathbf{F}$, the left Cauchy–Green deformation tensor $\mathbf{B}$, the electric field vector $\mathbf{E}$, and the magnetic field vector $\mathbf{H}$ for the given deformation map (4.1) are defined as:

$$\mathbf{F} = \begin{bmatrix} \lambda_r & 0 & 0 \\ 0 & \lambda_\theta & 0 \\ 0 & 0 & \lambda_z \end{bmatrix}, \quad \mathbf{B} = \mathbf{F}\mathbf{F}^T, \quad \mathbf{E} = \begin{bmatrix} 0 \\ 0 \\ E_0 \end{bmatrix}, \quad \mathbf{H} = \begin{bmatrix} 0 \\ 0 \\ H_0 \end{bmatrix}, \tag{4.3}$$

where λ_r, λ_θ, and λ_z are the principal stretches; E_0 and H_0 are the applied electric and magnetic field intensities on the membrane. The principal stretches of an incompressible ($\lambda_r\lambda_\theta\lambda_z$=1), isotropic circular membrane experiencing equi-biaxial deformation are defined as:

$$\lambda_r = \lambda, \quad \lambda_\theta = \lambda, \quad \lambda_z = \frac{1}{\lambda^2}, \tag{4.4}$$

where $\lambda = \dfrac{r}{R}$ and $\lambda_z = \dfrac{h}{H}$, respectively. The set of invariants of the left Cauchy–Green deformation tensor $\mathbf{B}$, the electrical field-based pseudo structural tensor ($\mathbf{E}^l \otimes \mathbf{E}^l$), and the magnetic field-based pseudo structural tensor ($\mathbf{H}^l \otimes \mathbf{H}^l$) for an incompressible, isotropic, and electro-magneto-elastic material deformation is given by [69]:

$$\begin{aligned} I_1 = \text{tr } \mathbf{B} = 2\lambda^2 + \frac{1}{\lambda^4}, \quad I_2 = \frac{1}{2}\left[(\text{tr } \mathbf{B})^2 - \text{tr } \mathbf{B}^2\right] = \lambda^4 + \frac{2}{\lambda^2}, \\ I_3 = \det \mathbf{B} = 1, \quad I_4 = \left[\mathbf{E}^l \otimes \mathbf{E}^l\right] : \mathbf{I} = \lambda^{-4}{E_0}^2, \quad I_5 = \left[\mathbf{E}^l \otimes \mathbf{E}^l\right] : \mathbf{B}^{-1} = {E_0}^2, \\ I_6 = \left[\mathbf{E}^l \otimes \mathbf{E}^l\right] : \mathbf{B}^{-2} = \lambda^4{E_0}^2, \quad I_7 = \left[\mathbf{H}^l \otimes \mathbf{H}^l\right] : \mathbf{I} = \lambda^{-4}{H_0}^2, \\ I_8 = \left[\mathbf{H}^l \otimes \mathbf{H}^l\right] : \mathbf{B}^{-1} = {H_0}^2, \quad I_9 = \left[\mathbf{H}^l \otimes \mathbf{H}^l\right] : \mathbf{B}^{-2} = \lambda^4{H_0}^2, \end{aligned} \tag{4.5}$$

where $\mathbf{E}^l = \mathbf{F}^T\mathbf{E}$, and $\mathbf{H}^l = \mathbf{F}^T\mathbf{H}$ represent the Lagrangian electric and magnetic field vectors in the reference configuration. In general, these membranes exhibit limiting extensibility. For example, the limiting stretch in biaxial deformation will be less than in uniaxial deformation. Thus, the phenomenological modeling of such membranes is based on limited extensibility. The most popular model to replicate such soft materials is the Gent model [71].

4.3 Governing equation

In this work, we use the following Gent type of total strain energy density function W defined in terms of the above invariants I_1, I_5, and I_8 as:

$$W = -\frac{\mu}{2}J_m \log\left(1 - \frac{I_1 - 3}{J_m}\right) - \frac{\varepsilon_0}{2}(C_1 I_5) - \frac{\alpha_0}{2}(C_2 I_8), \tag{4.6}$$

where ε_0 is the permittivity of the free space, α_0 is the permeability of the free space, μ is the shear modulus and J_m represents the strain stiffening parameter of

the membrane material. By following the theory of electro-magneto-elasticity [72], we may express the total Cauchy stress tensor $\mathbf{T}$, the electric displacement field $\mathbf{D}_e$ and the magnetic displacement field $\mathbf{D}_m$ for an incompressible and isotropic circular membrane, as follows:

$$\begin{aligned}\mathbf{T} = & -p\mathbf{I} + 2W_1\mathbf{B} + 2W_2\left(I_1\mathbf{B} - \mathbf{B}^2\right) - 2W_5\mathbf{E}\otimes\mathbf{E} - 2W_6\left(\mathbf{B}^{-1}\mathbf{E}\otimes\mathbf{E} + \mathbf{E}\otimes\mathbf{B}^{-1}\mathbf{E}\right) \\ & + 2W_8\left(\mathbf{BH}\otimes\mathbf{BH}\right) + 2W_9\left(\mathbf{BH}\otimes\mathbf{B}^2\mathbf{H} + \mathbf{B}^2\mathbf{H}\otimes\mathbf{BH}\right), \end{aligned} \tag{4.7a}$$

$$\mathbf{D_e} = -2\left(W_4\mathbf{B} + W_5\mathbf{I} + W_6\mathbf{B}^{-1}\right)\mathbf{E}, \tag{4.7b}$$

$$\mathbf{D_m} = -2\left(W_7\mathbf{B} + W_8\mathbf{B}^2 + W_9\mathbf{B}^3\right)\mathbf{H}. \tag{4.7c}$$

where p is a Lagrange multiplier to be obtained from the boundary conditions of incompressibility constraint and W_i is defined as $\dfrac{\partial W}{\partial I_i}$ for $i = 1, 2...9$. Substituting (4.6) in (4.7) with the use of (4.3), (4.4), and (4.5), we obtain the principal stress components as:

$$T_{rr} = T_{\theta\theta} = -p + \frac{J_m\mu\lambda^2}{J_m - I_1 + 3} \quad , \tag{4.8a}$$

$$T_{zz} = -p + \frac{J_m\mu\lambda^{-4}}{J_m - I_1 + 3} + C_1\varepsilon_0E_0^2 - C_2\alpha_0\lambda^{-8}H_0^2, \tag{4.8b}$$

$$D_{e3} = C_1\varepsilon_0E_0, \tag{4.8c}$$

$$D_{m3} = C_2\alpha_0\lambda^{-8}H_0. \tag{4.8d}$$

In Eqs. 4.8(c-d), $C_1 = \varepsilon_r$ denotes the relative electric permittivity and $C_2 = \alpha_r$ represents the relative magnetic permeability of the membrane. By applying the given traction-free boundary condition $T_{zz} = 0$ in Eq. 4.8(b), we obtain the hydrostatic pressure p as:

$$p = \frac{J_m\mu\lambda^{-4}}{J_m - I_1 + 3} + \varepsilon_r\varepsilon_0E_0^2 - \alpha_r\alpha_0\lambda^{-8}H_0^2. \tag{4.9}$$

Upon invoking the above expression of p in Eq. 4.8(a), we obtain the radial and hoop stress components as:

$$T_{rr} = T_{\theta\theta} = \frac{\mu J_m\left(\lambda^2 - \lambda^{-4}\right)}{J_m - I_1 + 3} - \varepsilon_r\varepsilon_0E_0^2 + \alpha_r\alpha_0\lambda^{-8}H_0^2, \tag{4.10a}$$

$$T_{rr} = T_{\theta\theta} = \frac{\mu J_m\left(\lambda^2 - \lambda^{-4}\right)}{J_m - I_1 + 3} - \varepsilon E_0^2 + \alpha\lambda^{-8}H_0^2. \tag{4.10b}$$

In the absence of electric and magnetic fields, the stress tensor can be derived from relation (Eq. 4.7) and is given as:

$$\mathbf{T} = -p\mathbf{I} + 2W_1\mathbf{B} + 2W_2[I_1\mathbf{B} - \mathbf{B}^2]. \tag{4.11}$$

To express the principal stress components for this case, we can derive them directly from Eq. 4.11 as follows:

$$T_{rr} = T_{\theta\theta} = -p + \frac{J_m \mu \lambda^2}{J_m - I_1 + 3} \quad , \tag{4.12a}$$

$$T_{zz} = -p + \frac{J_m \mu \lambda^{-4}}{J_m - I_1 + 3} \quad . \tag{4.12b}$$

It is important to note that $\mathbf{T}$ here excludes the electro-magneto-mechanical stress. Given the uniform transverse stress at the boundary, $T_{zz} = -P_t$, the Lagrange multiplier p can be determined as:

$$p = P_t + \frac{J_m \mu \lambda^{-4}}{J_m - I_1 + 3} \quad . \tag{4.13}$$

Upon invoking the above expression of p in Eq. 4.12(a), we obtain the radial and hoop stress components as:

$$T_{rr} = T_{\theta\theta} = \frac{\mu J_m \left(\lambda^2 - \lambda^{-4}\right)}{J_m - I_1 + 3} - P_t. \tag{4.14}$$

By comparing the radial stress expressions from Eqs. (4.10) and (4.14), we can conclude that: $P_t = \left|P_{t_{elect.}} + P_{t_{mag.}}\right| = \varepsilon_r \varepsilon_0 E_0^2 - \alpha_r \alpha_0 H_0^2 = \varepsilon E_0^2 - \alpha H_0^2$. Here, ε is electrical permittivity of material, α is magnetic permeability of material, $E_0 = (\frac{\upsilon}{h}) = \lambda^2(\frac{\upsilon}{H})$ and $H_0 = (\frac{\Psi}{h}) = \lambda^2(\frac{\Psi}{H})$ where υ is the applied voltage and Ψ is magnetic flux. Therefore, $P_T = \varepsilon_0 \varepsilon_r (\frac{\upsilon}{H})^2 - \alpha_r \alpha_0 (\frac{\Psi}{H})^2$ and $P_t = \lambda^4 P_T$.

4.3.1 Governing equation of the stretch-dependent electric permittivity

The permittivity of the elastomer ε exhibits a significant dependence on finite deformation [37,38,46,67]. Hence, it becomes essential to explore the effect of stretch-dependent permittivity on the dynamic behavior of the proposed membrane. In this

regard, Li et al. [67] suggested a phenomenological model to explain the significant electrostriction of these materials. Their approach describes the through-thickness permittivity of the thin dielectric elastomer as a linear function of the in-plane stretch ratios λ_1 and λ_2. Following [67], we express the stretch-dependent linear model of electric permittivity utilized in this study as:

$$\varepsilon\left(\lambda_1, \lambda_2\right) = \bar{\varepsilon}\left[1 + c\left(\lambda_1 + \lambda_2 - 2\right)\right], \tag{4.15a}$$

$$\varepsilon\left(\lambda\right) = \bar{\varepsilon}\left[1 + 2c\left(\lambda - 1\right)\right]. \tag{4.15b}$$

A nonlinear model intended to capture effectively the stretch-dependent permittivity phenomena in an elastomeric membrane was presented by Jiménez and McMeeking [38], which is expressed as:

$$\varepsilon\left(\lambda_1, \lambda_2\right) = \bar{\varepsilon} + c_0\left[2\lambda_1^{-2}\lambda_2^{-2} - \lambda_2^2 - \lambda_1^2\right], \tag{4.16a}$$

$$\varepsilon\left(\lambda\right) = \bar{\varepsilon} - 2c_0(\lambda^2 - \lambda^{-4}), \tag{4.16b}$$

here, the unique electrostrictive coefficient of the elastomer is symbolized by the symbol c_0, while the isotropic component of the permittivity tensor is represented by $\bar{\varepsilon}$. In particular, the values of these parameters, $\bar{\varepsilon}$ and c_0, vary between elastomers due to many variables such as the volume density of chain molecules, the polarizability of the intrinsic links and the number of links in a chain [38]. The stretch-dependent permittivity models used in this study are based on experimentally supported phenomenological formulations. The linear model [67] assumes that permittivity varies linearly with in-plane stretch, capturing first-order electrostrictive effects observed under moderate deformations. The nonlinear model [38] incorporates inverse and quadratic stretch terms derived from thermodynamic principles, offering greater accuracy at large deformations. These models reflect the physical mechanisms of chain alignment and volumetric constraints, and are employed here to assess the influence of stretch-dependent dielectric behavior on the membrane's dynamic response. As noted by Jiménez and McMeeking (see Equation (6) in [38]), the linear model (4.15) and the nonlinear model (4.16) are equivalent in the small deformation regime, i.e., when $\lambda_1, \lambda_2 \to 1$. We aim to use the parameters of the linear model (4.15) to characterize

those of the nonlinear model (4.16), since the parameters $\tilde{\varepsilon}$ and c_0 remain constant regardless of the deformation magnitude. For small deformations, the stretches can be expressed as $\lambda_1 = 1 + \delta_1$ and $\lambda_2 = 1 + \delta_2$, where $\delta_1, \delta_2 \ll 1$. Substituting into the nonlinear model (4.16), the permittivity becomes: $\varepsilon = \tilde{\varepsilon} - 6c_0(\delta_1 + \delta_2)$, whereas in the linear model (4.15), the permittivity is given by: $\varepsilon = \bar{\varepsilon} + \bar{\varepsilon}c(\delta_1 + \delta_2)$. A direct comparison of the two expressions yields the relationships: $\tilde{\varepsilon} = \bar{\varepsilon}$, and $c_0 = -\frac{\bar{\varepsilon}c}{6}$. Using the above expressions of $\tilde{\varepsilon}$ and c_0 in Eq. (4.16b), and considering equi-biaxial deformation, the linear and nonlinear models for the stretch-dependent permittivity of the membrane are expressed as follows [67]:

$$\varepsilon(\lambda) = \begin{cases} \varepsilon_l(\lambda) = \bar{\varepsilon}\left[1 + 2c(\lambda - 1)\right] & \text{(Linear)} \\ \varepsilon_{nl}(\lambda) = \bar{\varepsilon}\left[1 + \dfrac{c}{3}(\lambda^2 - \lambda^{-4})\right] & \text{(Nonlinear)} \end{cases}. \tag{4.17}$$

In the present study, $c = -0.053$ and $\bar{\varepsilon} = 4.68\varepsilon_0$ [32]. Eq. 4.10b is rewritten to accommodate both the linear and nonlinear models of stretch-dependent permittivity as:

$$\left[\begin{array}{c} \left\{T_{rr} = T_{\theta\theta} = \dfrac{\mu J_m\left(\lambda^2 - \lambda^{-4}\right)}{J_m - I_1 + 3} - \bar{\varepsilon}E_0^2 + \alpha\lambda^{-8}H_0^2\right\} \\ (\textit{Stretch independent permittivity or constant model}) \\ \left\{T_{rr} = T_{\theta\theta} = \dfrac{\mu J_m\left(\lambda^2 - \lambda^{-4}\right)}{J_m - I_1 + 3} - \bar{\varepsilon}[1 - 0.106(\lambda - 1)]E_0^2 + \alpha\lambda^{-8}H_0^2\right\} (\textit{Linear model}) \\ \left\{T_{rr} = T_{\theta\theta} = \dfrac{\mu J_m\left(\lambda^2 - \lambda^{-4}\right)}{J_m - I_1 + 3} - \bar{\varepsilon}[1 - 0.01768(\lambda^2 - \lambda^{-4})]E_0^2 + \alpha\lambda^{-8}H_0^2\right\} \\ (\textit{Nonlinear model}) \end{array}\right]. \tag{4.18}$$

The equation governing the equilibrium of an incompressible, isotropic elastic circular membrane undergoing axisymmetric deformation can be expressed as follows:

$$\frac{dT_{rr}}{dr} + \frac{T_{rr} - T_{\theta\theta}}{r} + \rho b_f = \rho\frac{d^2r}{dt^2}, \tag{4.19}$$

In the above expression, ρ, and b_f denote the material density of the membrane, and the body force per unit volume, respectively. Under the boundary condition $T_{rr}(r = r_0) = \frac{P}{2\pi r_0 h}$ and assuming the absence of a body force $b_f = 0$, the radial equilibrium equation (Eq. 4.19) can be balanced using (Eq. 4.18) as:

$$\frac{P}{2\pi r_0 h} - T_{rr} = \int_0^{r_0} \rho\frac{d^2r}{dt^2}\, dr \Rightarrow \frac{d^2\lambda}{dt^2} + \frac{2T_{rr}}{\lambda\rho R_0^2} - \frac{P}{\pi r_0 h\lambda\rho R_0^2} = 0. \tag{4.20}$$

Upon invoking the expression of T_{rr} for different model from Eq. (4.18) in Eq.

(4.20), we obtain

$$\left[\begin{array}{l} \left\{\dfrac{d^2\lambda}{d\tau^2}+\dfrac{J_m(\lambda-\lambda^{-5})}{\left(J_m-2\lambda^2-\frac{1}{\lambda^4}+3\right)}-\lambda^3V^2+\lambda^{-5}M^2-S=0\right\}(Constant\ model) \\ \\ \left\{\dfrac{d^2\lambda}{d\tau^2}+\dfrac{J_m(\lambda-\lambda^{-5})}{\left(J_m-2\lambda^2-\frac{1}{\lambda^4}+3\right)}-(1.106\lambda^3-0.106\lambda^4)V^2+\lambda^{-5}M^2-S=0\right\}(Linear\ model) \\ \\ \left\{\dfrac{d^2\lambda}{d\tau^2}+\dfrac{J_m(\lambda-\lambda^{-5})}{\left(J_m-2\lambda^2-\frac{1}{\lambda^4}+3\right)}-(\lambda^3-0.01748\lambda^5+0.01768\lambda^{-1})V^2+\lambda^{-5}M^2-S=0\right\} \\ \\ (Nonlinear\ model) \end{array}\right], \tag{4.21}$$

where $\tau = \dfrac{\sqrt{2}t}{R_0\sqrt{\dfrac{\rho}{\mu}}}$ is the dimensionless time, $S = \dfrac{P}{2\pi\mu R_0 H}$ is the nominal equal-biaxial normalized stress at the boundary, $V = \dfrac{\upsilon}{H\sqrt{\dfrac{\mu}{\varepsilon}}}$ is the normalized voltage, $M = \dfrac{\Psi}{H\sqrt{\dfrac{\mu}{\alpha}}}$ is the normalized flux.

Essentially, we reiterate that normalized transverse pressure may successfully replace normalized voltage V and magnetic flux M to provide an analogous effect on the dynamical system, as shown by the results of [73]. This equivalency enables us to treat normalized voltage and flux as normalized transverse pressure. The behavior of the dynamical system may be consistently analyzed by using the normalized voltage and flux in place of the normalized transverse pressure. The governing equation that provides insight into the dynamic behavior of a circular membrane experiencing

equi-biaxial electro-magneto-elastic deformation is written as:

$$\frac{d^2\lambda}{d\tau^2} + g(\lambda; J_m, V, M, S) = 0, \tag{4.22}$$

where $g(\lambda; J_m, V, M, S) =$

$$\left[\begin{array}{ll} \left\{\dfrac{J_m(\lambda-\lambda^{-5})}{J_m-2\lambda^2-\lambda^{-4}+3} - \lambda^3V^2 + \lambda^{-5}M^2 - S\right\} & \text{(Constant model)} \\ \\ \left\{\dfrac{J_m(\lambda-\lambda^{-5})}{J_m-2\lambda^2-\lambda^{-4}+3} - \left(1.106\lambda^3 - 0.106\lambda^4\right)V^2 + \lambda^{-5}M^2 - S\right\} & \text{(Linear model)} \\ \\ \left\{\begin{array}{c}\dfrac{J_m(\lambda-\lambda^{-5})}{J_m-2\lambda^2-\lambda^{-4}+3} - \left(\lambda^3 - 0.01748\lambda^5 + 0.01768\lambda^{-1}\right)V^2 \\ + \lambda^{-5}M^2 - S\end{array}\right\} & \text{(Nonlinear model)} \end{array}\right]. \tag{4.23}$$

4.3.2 Governing equation of the stretch-dependent magnetic permeability

By assuming the same variation as that of electric permittivity, the permeability of material in terms of principal stretch for linear and nonlinear model is written as:

$$\alpha(\lambda) = \left\{\begin{array}{l} \alpha_l(\lambda) = \bar{\alpha}\left[1 + 2\kappa(\lambda - 1)\right] \quad (Linear) \\ \alpha_{nl}(\lambda) = \bar{\alpha}\left[1 + \dfrac{\kappa}{3}(\lambda^2 - \lambda^{-4})\right] (Nonlinear) \end{array}\right\}, \tag{4.24}$$

where κ is the magnetostrictive coefficient unique to the elastomer and $\bar{\alpha}$ denotes the isotropic component of the permeability. We consider $\bar{\alpha} = 3.45\alpha_0$ by calibrating with the experimental results reported by Vatandoost et al. [76] and $\kappa = -0.053$ [32]. Eq. 4.10b is rewritten to accommodate both the linear and nonlinear models of stretch-

dependent permeability as:

$$\left[\begin{array}{l}\left\{T_{rr} = T_{\theta\theta} = \dfrac{\mu J_m\left(\lambda^2 - \lambda^{-4}\right)}{J_m - I_1 + 3} - \varepsilon E_0^2 + \bar{\alpha}\lambda^{-8}H_0^2\right\} \\ \qquad\qquad\qquad\qquad \text{(Stretch-independent permeability or constant model)} \\ \\ \left\{T_{rr} = T_{\theta\theta} = \dfrac{\mu J_m\left(\lambda^2 - \lambda^{-4}\right)}{J_m - I_1 + 3} - \varepsilon E_0^2 + \bar{\alpha}\left[1 - 0.106(\lambda - 1)\right]\lambda^{-8}H_0^2\right\} \quad \text{(Linear model)} \\ \\ \left\{T_{rr} = T_{\theta\theta} = \dfrac{\mu J_m\left(\lambda^2 - \lambda^{-4}\right)}{J_m - I_1 + 3} - \varepsilon E_0^2 + \bar{\alpha}\left[1 - 0.01768(\lambda^2 - \lambda^{-4})\right]\lambda^{-8}H_0^2\right\} \quad \text{(Nonlinear model)}\end{array}\right]. \tag{4.25}$$

Upon invoking the expression of T_{rr} from Eq. (4.25) in Eq. (4.20), we obtain

$$\left[\begin{array}{l}\left\{\dfrac{d^2\lambda}{d\tau^2} + \dfrac{J_m(\lambda - \lambda^{-5})}{J_m - 2\lambda^2 - \lambda^{-4} + 3} - \lambda^3 V^2 + \lambda^{-5}M^2 - S = 0\right\} \quad \text{(Constant model)} \\ \\ \left\{\dfrac{d^2\lambda}{d\tau^2} + \dfrac{J_m(\lambda - \lambda^{-5})}{J_m - 2\lambda^2 - \lambda^{-4} + 3} - \lambda^3 V^2 + \left(1.106\lambda^{-5} - 0.106\lambda^{-4}\right)M^2 - S = 0\right\} \quad \text{(Linear model)} \\ \\ \left\{\begin{array}{l}\dfrac{d^2\lambda}{d\tau^2} + \dfrac{J_m(\lambda - \lambda^{-5})}{J_m - 2\lambda^2 - \lambda^{-4} + 3} - \lambda^3 V^2 \\ \qquad + \left(\lambda^{-5} - 0.01748\lambda^{-3} + 0.01768\lambda^{-9}\right)M^2 - S = 0\end{array}\right\} \quad \text{(Nonlinear model)}\end{array}\right]. \tag{4.26}$$

The governing equation describing the dynamic behavior of the membrane, taking into account the variation in the magnetic permeability of the material in Eq. (4.26), can be written as:

$$\frac{d^2\lambda}{d\tau^2} + f(\lambda; J_m, V, M, S) = 0. \tag{4.27}$$

where $f(\lambda; J_m, V, M, S) =$

$$\left[\begin{array}{l} \left\{\dfrac{J_m(\lambda-\lambda^{-5})}{J_m-2\lambda^2-\lambda^{-4}+3}-\lambda^3V^2+\lambda^{-5}M^2-S\right\} \qquad \text{(Constant model)} \\ \\ \left\{\dfrac{J_m(\lambda-\lambda^{-5})}{J_m-2\lambda^2-\lambda^{-4}+3}-\lambda^3V^2+\left(1.106\lambda^{-5}-0.106\lambda^{-4}\right)M^2-S\right\} \qquad \text{(Linear model)} \\ \\ \left\{\dfrac{J_m(\lambda-\lambda^{-5})}{J_m-2\lambda^2-\lambda^{-4}+3}-\lambda^3V^2+\left(\lambda^{-5}-0.01748\lambda^{-3}\right.\right. \\ \qquad\qquad \left.\left.+0.01768\lambda^{-9}\right)M^2-S\right\} \qquad \text{(Nonlinear model)} \end{array}\right]. \tag{4.28}$$

Table 4.1: Electromagnetic models with different considered parameters

Property	**Model**	**Relation for equibiaxial stretch**	**Parameters and source**
Permittivity	Constant	$\varepsilon(\lambda) = \bar{\varepsilon}$	$\bar{\varepsilon} = 4.68\varepsilon_0$; [32]
Permittivity	Linear	$\varepsilon(\lambda) = \bar{\varepsilon}[1 + 2c(\lambda - 1)]$	$c = -0.053$ (dimensionless); [67]
Permittivity	Nonlinear	$\varepsilon(\lambda) = \bar{\varepsilon}[1 + \frac{c}{3}(\lambda^2 - \lambda^{-4})]$	$c = -0.053$ (dimensionless); [38]
Permeability	Constant	$\alpha(\lambda) = \bar{\alpha}$	$\bar{\alpha} = 3.45\alpha_0$; [76]
Permeability	Linear	$\alpha(\lambda) = \bar{\alpha}[1 + 2\kappa(\lambda - 1)]$	$\kappa = -0.053$ (dimensionless); assumed in this study
Permeability	Nonlinear	$\alpha(\lambda) = \bar{\alpha}[1 + \frac{\kappa}{3}(\lambda^2 - \lambda^{-4})]$	$\kappa = -0.053$ (dimensionless); assumed in this study

In Table 4.1, ε_0 and α_0 denote the permittivity and magnetic permeability of free space, respectively. The coefficients c and κ are dimensionless; therefore, all three permittivity models have units of $\mathrm{F\,m^{-1}}$, and all three permeability models have units of $\mathrm{H\,m^{-1}}$. The permeability relations adopt the same stretch-dependent forms as the permittivity relations. The value of κ is a modeling assumption in this study and has not been independently calibrated for the same membrane material. These relations are applied only over the stretch range reached in the simulations; extrapolation beyond that range requires material-specific measurements.

4.3.3 Numerical solution procedure

The nonlinear governing equations are solved numerically in MATLAB using the `ode45` solver based on an adaptive Runge–Kutta (4,5) scheme. The numerical simulations are initiated using $\lambda(0) = 1$ and $\dot{\lambda}(0) = 0$. Since `ode45` uses adaptive time stepping, a fixed integration time step is not prescribed. The solutions are evaluated at 10,000 equally spaced time points for plotting and post-processing.

A dimensionless simulation duration of $\tau = 20$ is used for the regular dynamic responses, phase trajectories, whereas $\tau = 400$ is used for AC voltage dynamics by constructing the time history, phase and Poincaré section. For frequency-response calculations, the normalized excitation frequency is varied from 0 to 2.5 in increments of 0.1, and the response amplitude is calculated as:

$$A = \frac{\lambda_{\max} - \lambda_{\min}}{2}. \tag{4.29}$$

For the Poincaré analysis, the response is sampled once per excitation period, $T = 2\pi/\omega$, using the corresponding values of stretch and stretch rate. No separate transient-removal procedure or user-defined solver tolerance is imposed; the adaptive error-control settings of `ode45` are used.

4.4 DC dynamic response of different models of permittivity and permeability

Using the time-independent normalized voltage, V, the membrane's DC dynamic properties are assessed in this section. Specifically, in the governing Eqs. (4.21), there are two state variables λ and $\frac{d\lambda}{d\tau}$ and the corresponding initial conditions of these state variables at $\tau = 0$ are given as: $(\lambda)_{\tau=0} = 1$; $\left(\frac{d\lambda}{d\tau}\right)_{\tau=0} = 0$. A parametric study is specifically conducted to assess the impact of the permittivity (constant, linear, and nonlinear), the impact of the permeability (constant, linear, and nonlinear), normalized pre-stress parameter (S) and strain stiffening parameter (J_m) on the dynamic response of the membrane.

First, to examine the influence of material parameter variations, time-history plots and phase diagrams were generated for constant, linear, and nonlinear models of permittivity and permeability, as shown in Fig. 4.2. The time-history results indicate that, for all considered cases, the membrane exhibits stable oscillations about a steady equilibrium stretch (Figs. 4.2a–b). In the permittivity-controlled case (Fig. 4.2a), the constant model yields slightly higher oscillation amplitudes compared to the linear and nonlinear models, whereas in the permeability-controlled case (Fig. 4.2b), the amplitudes for all three models nearly coincide. The corresponding phase portraits further highlight these trends: for permittivity variation (Fig. 4.2c), the closed-loop trajectories shrink progressively from the constant to the nonlinear model, indicating a reduction in dynamic range. In contrast, for permeability variation (Fig. 4.2d), the trajectories exhibit only minor deviations among the three models, confirming that permeability variation has a comparatively smaller effect on the membrane's oscillatory dynamics under the selected parameter set.

Figure 4.3 presents the DC dynamic responses of the membrane for the case of higher actuation amplitudes, considering three different models of permittivity at $V = 1, M = 0.25$ and permeability at $V = 0.25, M = 1$: constant, linear, and nonlinear. At this elevated actuation level, the induced Maxwell stress is substantially larger than in the low-actuation case ($V = M = 0.25$), resulting in significantly

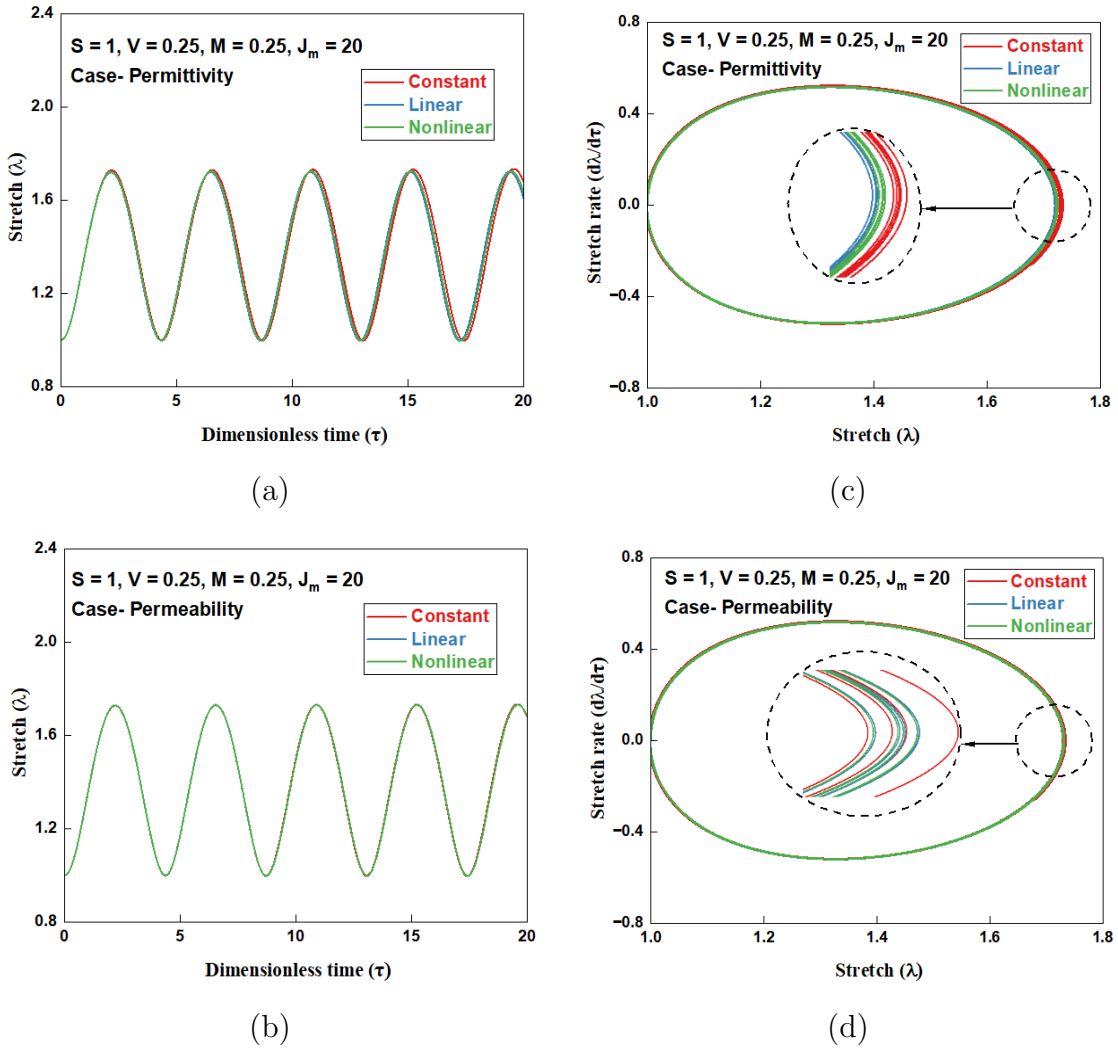


Figure 4.2: DC dynamic responses of the membrane with (a–b) time evolution diagrams, (c-d) phase diagrams for different models (constant, linear, and nonlinear) of permittivity and permeability at $V = M = 0.25$ with $J_m = 20$ and $S = 1$.

greater deformation amplitudes. In the time-evolution plots (Figs. 4.3(a) and 4.3(b)), the stretch (λ) exhibits pronounced divergence between the constant, linear, and nonlinear models. The nonlinear model, in particular, produces distinctly higher peak stretches compared to the other two, indicating the stronger influence of stretch-dependent material properties under large electromechanical loads. In contrast, at $V = M = 0.25$ (previously shown in Fig. 4.2), the oscillation amplitudes for the three models were nearly coincident, reflecting only a marginal effect of stretch-dependence at low actuation levels. The phase diagrams (Figs. 4.3(c) and 4.3(d)) further highlight

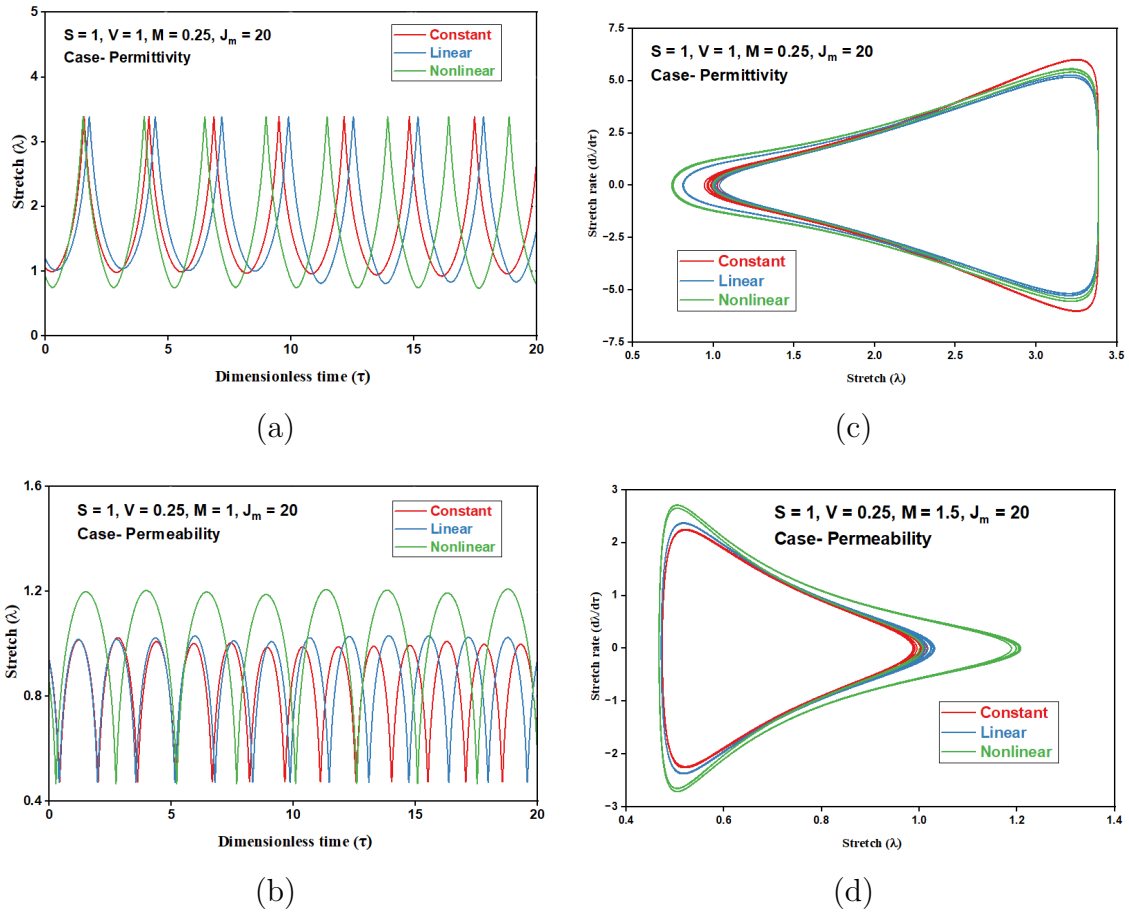


Figure 4.3: DC dynamic responses of the membrane with (a–b) time evolution diagrams, (c-d) phase diagrams for different models (constant, linear, and nonlinear) of permittivity at $V = 1$, $M = 0.25$ and permeability at $V = 0.25$, $M = 1$.

these differences. At higher values of V and M, the trajectories expand significantly in the stretch–stretch-rate (λ, $d\lambda/d\tau$) space, and the loop shapes for the different models become clearly distinguishable. The nonlinear model forms the widest loop, demonstrating the strongest energy exchange between the electrical and mechanical domains, whereas the constant model shows the narrowest trajectory. This contrasts with the low-actuation case, where the loops for all three models were tightly clustered, indicating minimal variation in dynamic response due to stretch-dependence. Overall, the comparison confirms that the effect of stretch-dependent permittivity and permeability is strongly amplitude-dependent. While negligible at low actuation, these effects become increasingly significant at higher electromagnetic loading, where

nonlinear electromechanical coupling dominates the system's dynamic behavior.

4.5 AC dynamic response of different models of permittivity and permeability

Analyzing a circular membrane becomes significantly more complex under time-dependent voltage fluctuations. These dynamic changes can introduce chaotic behavior, prompting a detailed investigation of the membrane's response. Specifically in the present study, the membrane is excited by a harmonic time-dependent AC voltage described as:

$$V(t) = V_a \sin(\omega_0 t), \tag{4.30}$$

where the term V_a denotes the magnitude of the applied AC voltage, ω_0 denotes the excitation frequency of the system. The required governing equations for varying electric permittivity and magnetic permeability models under the applied AC voltage are provided in Appendix A. For consistency, the initial conditions used in this section are the same as those defined in Section 4.4, with $\lambda|_{\tau=0} = 1$ and $\left.\frac{d\lambda}{d\tau}\right|_{\tau=0} = 0$.

First, for the three models considered (constant, linear and nonlinear) of electric permittivity (Figs. 4.4a-b) and magnetic permeability (Figs. 4.4c-d), we evaluate the membrane oscillation amplitude (A) change with the applied dimensionless excitation frequency (ω). Half the difference between the maximum and the minimum values is known as the oscillation's amplitude of the stretch λ, which can be found using the formula: $A = (\lambda_{max} - \lambda_{min})/2$. When the membrane is activated at its natural angular frequency ($\omega = \omega_n$), the oscillation amplitude in all of the situations under consideration (Fig. 4.4a-d) achieves its maximum value. This occurs because the system's energy transmission is most effective at the natural angular frequency, which is its fundamental frequency. At lower actuation parameters ($V = M = 0.25$), shown in Figs. 4.4(a, c), the amplitude-frequency response corresponding to constant, linear, and nonlinear models is almost identical. This indicates that under weak

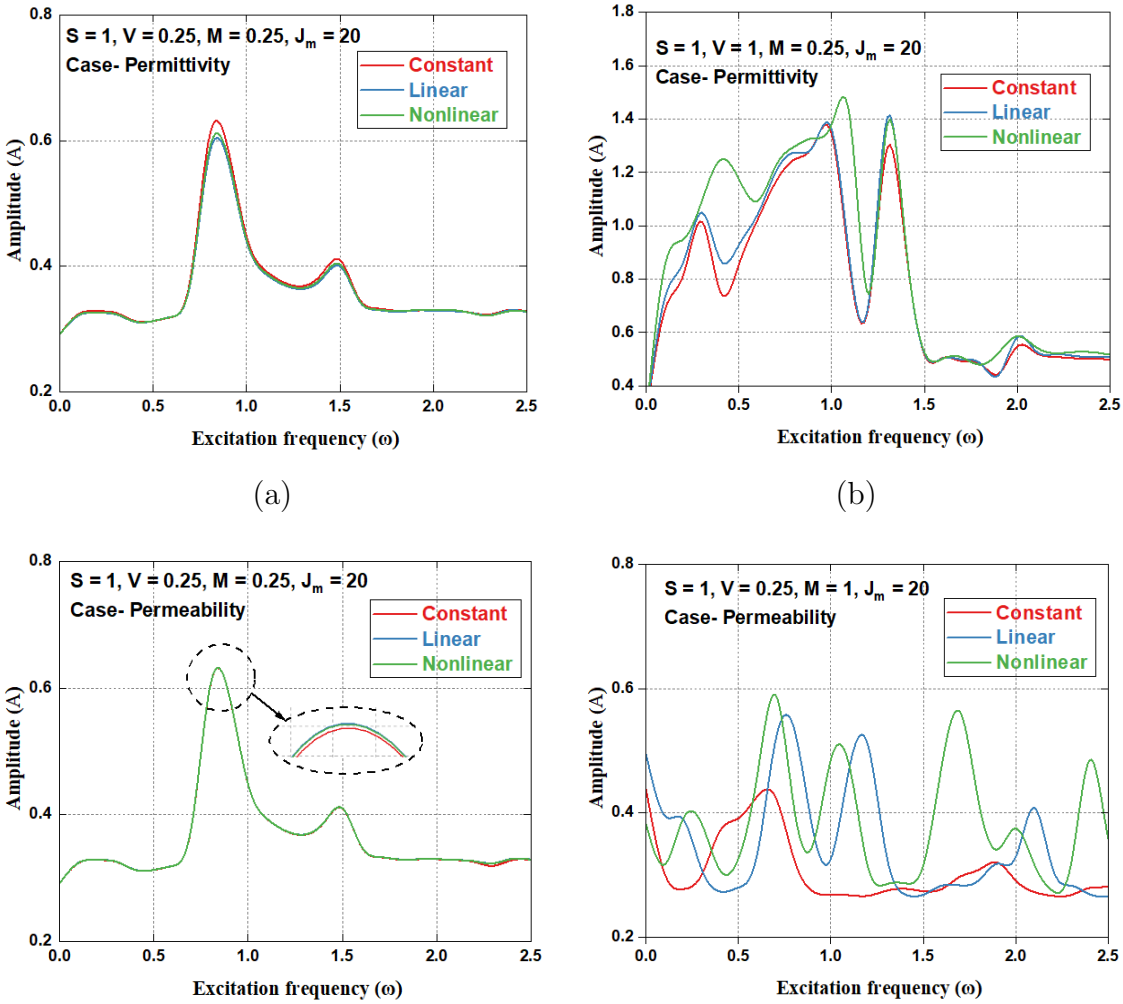


Figure 4.4: Variation of stretch amplitude with the applied excitation frequency for different models of (a, b) electric permittivity at $V = 0.25$ and 1.0 and (c, d) magnetic permeability at $M = 0.25$ and 1.0.

electro-magneto-mechanical coupling, the effect of stretch-dependent permittivity and permeability remains marginal, and the natural frequency is nearly unaffected by the choice of model. In contrast, when the actuation levels are increased, as shown in Figs. 4.4(b, d), a clear influence of the constitutive model can be observed. For the permittivity case ($V = 1.0, M = 0.25$), Fig. 4.4(b) reveals noticeable shifts in the resonance peaks for the nonlinear model compared to the constant and linear ones, particularly around $\omega \approx 0.5$ and $\omega \approx 1.0$. Similarly, in the permeability case

($V = 0.25, M = 1.0$), Fig. 4.4(d) shows significant deviations in amplitude response across multiple frequency bands depending on the selected model. This comparison highlights that the role of stretch dependency in permittivity and permeability becomes more prominent at higher actuation levels due to stronger electro-magneto-mechanical coupling. While at low excitation the influence of nonlinear constitutive effects is negligible, at higher actuation they play a crucial role in governing the resonance characteristics and natural frequency of the smart membrane.

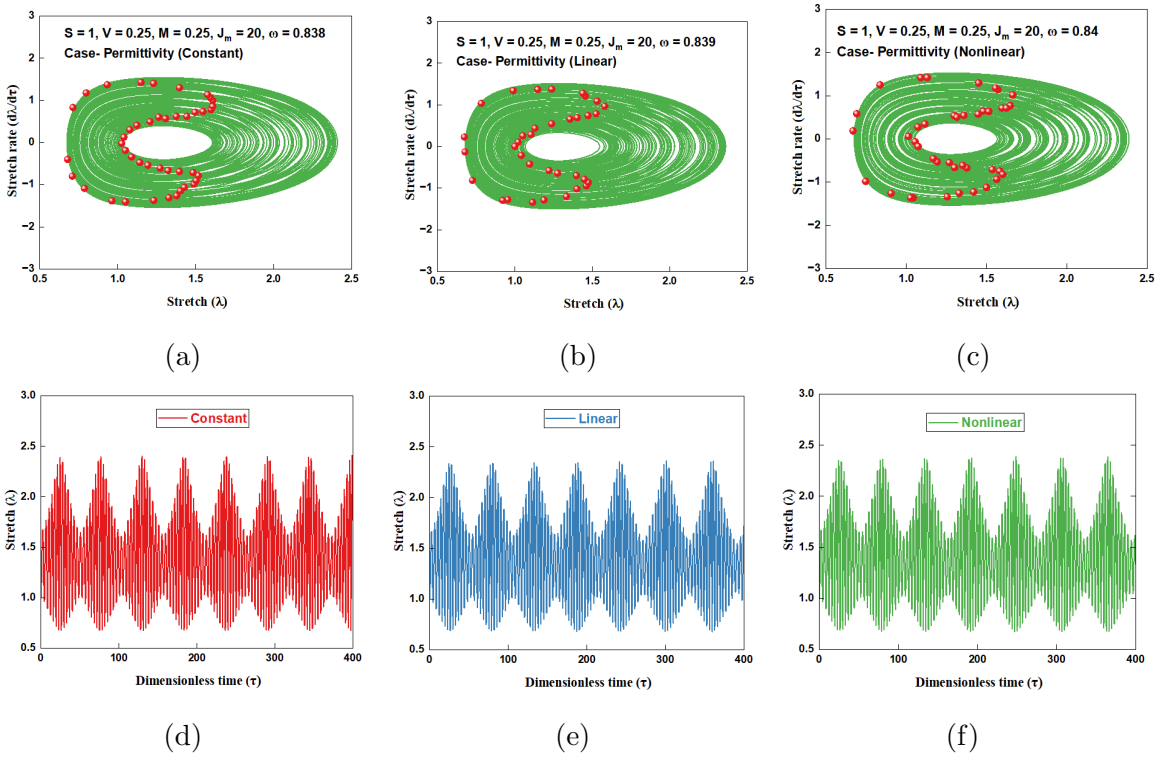


Figure 4.5: AC dynamic responses of the membrane with (a–c) phase diagrams merged with Poincaré plots, (d–f) time evolution diagrams corresponding to the resonant excitation frequencies for different models of electric permittivity.

In the following discussion, a periodic response refers to a response that repeats after a fixed time period, whereas a quasi-periodic response contains multiple interacting frequencies and does not repeat over a single period. A bounded oscillation indicates that the membrane response remains within a finite range and does not necessarily imply periodicity. Static stability refers to the stability of an equilibrium configuration

and is therefore different from the nature of the time-dependent oscillatory response.

We further examine the influence of different models (constant, linear, and nonlinear) of permittivity on the dynamic response of the membrane when it is excited at the resonance frequency (Fig. 4.5). The phase diagram plots (Figs. 4.5a-c) show that on moving from constant to nonlinear model, the envelope represents the magnitude of the maximum and minimum feasible stretch rate ($d\lambda/d\tau$). It is approximately the same for each model with negligible variation. Phase diagrams also show that when activated at resonance frequencies, the membrane shows substantial nonlinear oscillation behavior. Poincaré points may effectively depict complicated dynamical behaviors, such as periodicity, quasi-periodicity, and chaos, in a single visual representation, and hence it is advantageous to display them together in the phase diagram [26, 49, 77]. For every model taken into consideration, the Poincaré plot creates closed loops, indicating the membrane's quasi-periodic stable oscillation nature [78, 79]. Thus, we conclude that the membrane's dynamic stability is unaffected by the different permittivity models. For every model taken into consideration, the membrane is shown to exhibit stable oscillations with time-varying amplitude, according to the time history plot (Figs. 4.5d-f). It is known as the "beating phenomenon" [80, 81]. On the other hand, the amplitude of the steady oscillations is approximately the same for each model with slight variation.

Similarly, we examine the influence of different models (constant, linear, and nonlinear) of permeability on the dynamic response of the membrane when it is excited at the resonance frequency (Fig. 4.6). The phase diagram plots (Figs. 4.6a-c) show that on moving from a constant to a nonlinear model, the envelope size is approximately the same for each model with negligible variation. Phase diagrams also show that when activated at resonance frequencies, the membrane shows substantial nonlinear oscillation behavior. The Poincaré plot creates closed loops for each model indicating the membrane's quasi-periodic stable oscillation nature. Thus, we conclude that the membrane's dynamic stability is unaffected by different permeability models. According to the time history plot (Figs. 4.6d-f), the system exhibits stable oscillations with varying amplitude. The amplitude of the steady oscillations is approximately the same

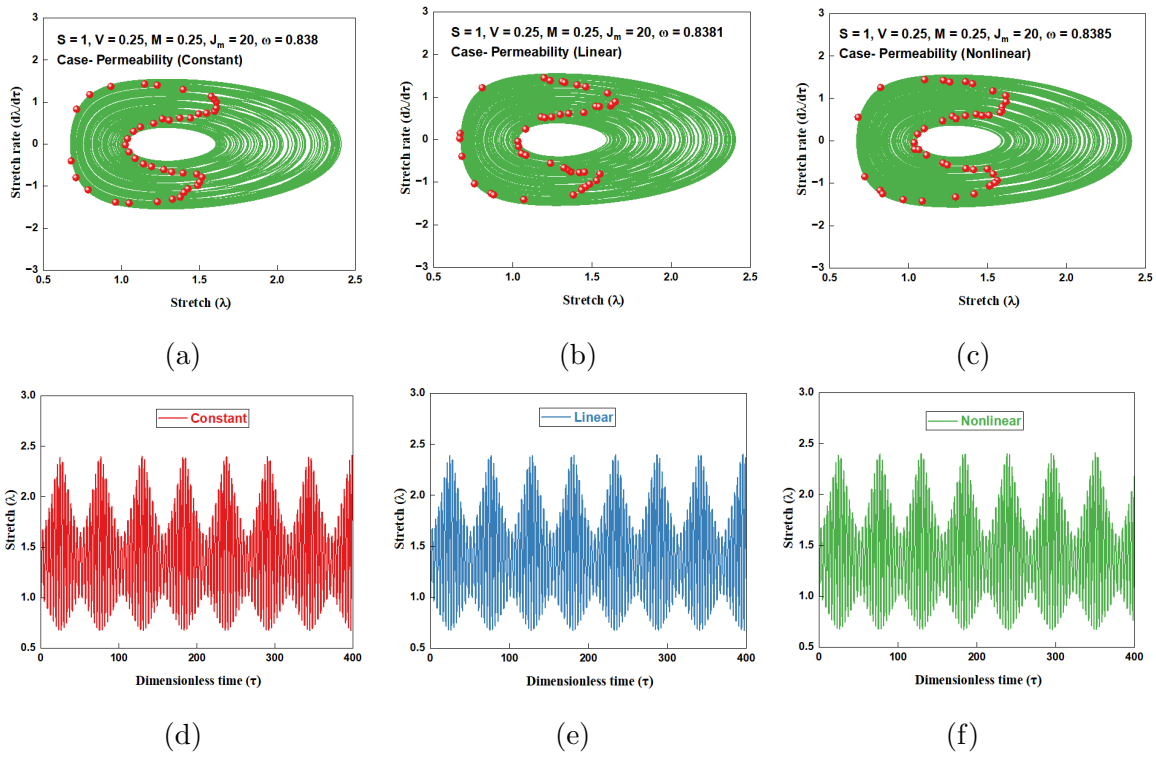


Figure 4.6: AC dynamic responses of the membrane with (a–c) phase diagrams merged with Poincaré plots, (d–f) time evolution diagrams corresponding to the resonant excitation frequencies for different models of magnetic permeability.

for each model of permeability with slight variation.

The obtained results are found to be consistent with the physical behavior reported in the literature for soft active elastomers and electro-magneto-active membranes. The nonlinear stretch-dependent models of electric permittivity and magnetic permeability predict larger deformation amplitudes and stronger resonance behavior compared to constant and linear models, which agrees with experimental and theoretical observations that electromagnetic properties increase with deformation. Similarly, the increase in oscillation amplitude and energy under higher electric and magnetic loading follows the expected softening and field-coupling behavior of smart elastomeric materials. The predicted phase trajectories, resonance characteristics, and nonlinear dynamic responses also show good qualitative agreement with previously reported studies on electroactive and magnetoactive membranes, confirming the validity and

physical consistency of the present model.

4.6 Summary

This chapter presents a comprehensive modeling framework based on continuum physics to explore the intricate nonlinear dynamics of a circular membrane subjected to electro-magneto-mechanical loadings. By replacing conventional transverse pressure with electric and magnetic fields, a qualitative analysis has been conducted to investigate the system's response under varying models of permittivity and permeability. A nonlinear differential equation governing the radial axisymmetric motion of the membrane has been analyzed.

i. In DC dynamics, results confirm that stretch-dependent electromagnetic effects are negligible at low actuation, showing nearly identical responses but become dominant at higher field strengths, where nonlinear coupling governs the system dynamics.

ii. In AC dynamics, from the amplitude-frequency diagram, it is seen that at low actuation levels, all constitutive models yield nearly identical amplitude–frequency responses, indicating a negligible effect of stretch-dependent permittivity and permeability. At higher actuation, the nonlinear model exhibits clear shifts in resonance behavior, demonstrating that stretch-dependent electromagnetic effects become dominant under strong electro–magneto–mechanical coupling.

iii. In AC dynamics, the membrane exhibits subtle variations in amplitude across different permittivity and permeability models at the fundamental natural frequency. The nonlinear model dominates the other models as the envelope size increases, showing that the system contains more energy. The Poincaré map further reveals the presence of quasi-periodic oscillations, demonstrating the complex interplay between different models. These findings highlight the nonlinear and intricate nature of the membrane's oscillatory behavior, with important

implications for the stability and control of such electro-magneto-mechanical systems.

This chapter examined the dynamic behavior of electro-magneto-active circular membranes by considering constant, linear, and nonlinear stretch-dependent models of electric permittivity and magnetic permeability. The results showed that the nonlinear model produced larger deformation amplitudes and stronger resonance responses, particularly at higher electric and magnetic loading conditions ($V = 1$ and $M = 1$), compared to the constant and linear models. Under AC excitation, the nonlinear model also displayed wider resonance regions and more noticeable nonlinear oscillations in the phase and Poincaré responses. Overall, the study demonstrates that stretch-dependent electromagnetic properties play an important role in accurately predicting the dynamic response and stability characteristics of smart membranes.

The next chapter investigates the formation and stability of taut domains in particle-reinforced electro-magneto-active circular membranes under combined electric and magnetic fields. It examines the influence of electromagnetic loading, filler volume fraction, and shear modulus ratio on membrane deformation, stability limits, and field-induced instabilities.

Chapter 5

Taut Domain Formation in Particle-Reinforced EMAMs

Preface

Pull-in and wrinkling are important instability mechanisms that influence the performance of soft active membranes. This chapter develops a taut domain framework to predict these instabilities in particle-reinforced electro-magneto-active membranes. The effects of electrical loading, magnetic loading, and reinforcement parameters on the stability limits and stress-stretch behavior are discussed.

5.1 Introduction

Taut domains are a defining feature of stretched soft membranes and play a key role in controlling their stability and deformation behavior. When a membrane is sufficiently stretched, the resulting tensile stresses help maintain a stable configuration. However, in soft active materials, the application of strong electric and magnetic fields can significantly alter this balance, leading to changes in stress distribution and, in some cases, the onset of instability.

Although several studies have examined wrinkling and instability in electroactive and magnetoactive membranes, limited attention has been given to particle-reinforced electro-magneto-active circular membranes under combined electric and magnetic

loading. In particular, the influence of particle reinforcement on taut domain evolution, attainable deformation states, and stability limits is still not well understood. The novelty of this chapter lies in the development of a continuum-based framework for analyzing taut domain formation in particle-reinforced electro-magneto-active circular membranes. The study investigates the combined effects of electric field, magnetic field, filler volume fraction, and shear modulus ratio on membrane stability and deformation characteristics. The main objectives of this chapter are:

- To formulate the governing equations for taut domain analysis in particle-reinforced electro-magneto-active circular membranes.
- To investigate the influence of electric and magnetic fields on taut domain formation and stability behavior.
- To study the effects of filler volume fraction and shear modulus ratio on membrane deformation and field-induced instabilities.

A theoretical framework is developed to capture the coupled effects of finite deformation, electromagnetic loading, and material reinforcement. The influence of electric and magnetic field strengths, particle volume fraction, and material shear modulus ratio of filler and matrix of membrane is systematically examined to identify the conditions under which taut domains form and lose stability. The results provide insight into how electromagnetic fields can be used to control membrane stability and deformation in soft active systems.

5.2 Mathematical formulation

In the present study, the particle-reinforced electro-magneto-active circular membrane is assumed to behave as a homogeneous, isotropic, and hyperelastic material. The membrane undergoes large elastic deformation and is considered incompressible throughout the analysis. Since the membrane thickness is very small compared to its in-plane dimensions, bending effects are neglected. Uniform electric and magnetic

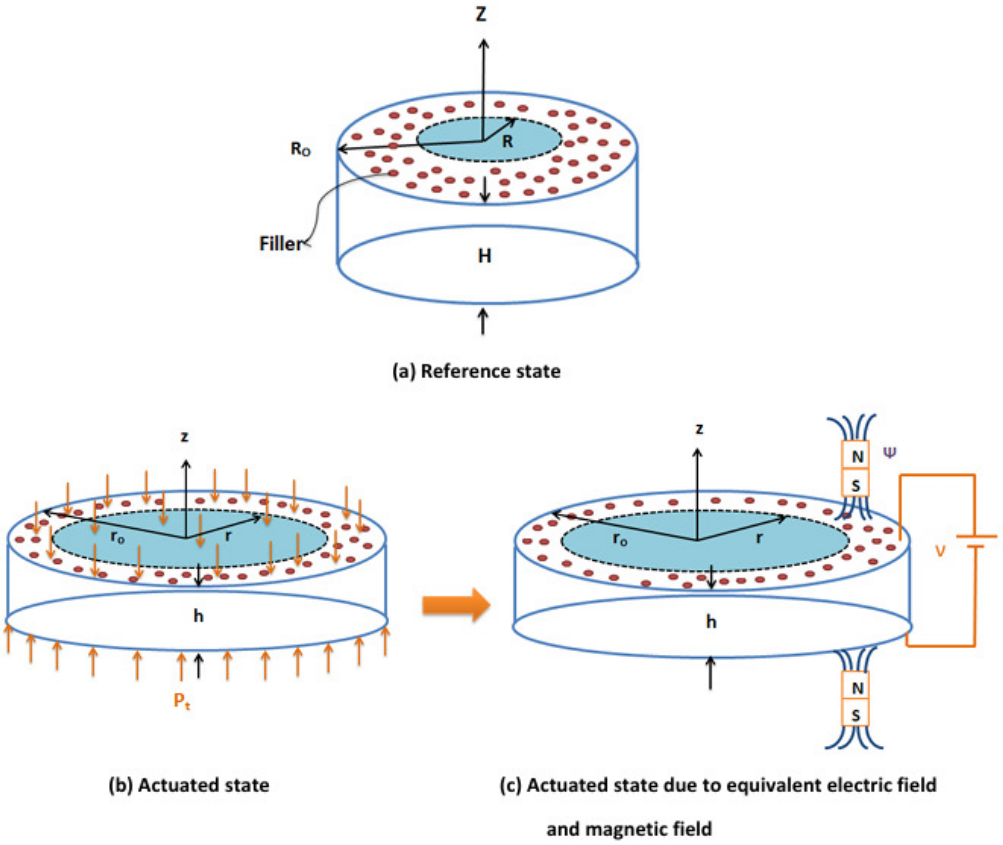


Figure 5.1: Schematic representation of the circular membrane: (a) Initial or reference state, (b) Deformed or actuated state caused by a uniformly applied transverse pressure P_t, and (c) Equivalent deformed state as in (b), achieved due to the transverse electric and magnetic fields.

fields are applied across the membrane, and the deformation is assumed to remain axisymmetric. The reinforcing particles are considered to be uniformly distributed within the elastomer matrix, while thermal effects, body forces, and material damping are not included in the present model.

In the present study, we consider a circular membrane with the coordinate systems (R, Θ, Z) in the reference state β_0 and (r, θ, z) in the current state β, respectively. The membrane has an undeformed radius R_0 with a thickness H, and is assumed to be axisymmetric and incompressible, with reinforcing particles as shown in Fig. 5.1(a). Under the applied load, the membrane undergoes radial expansion and thickness contraction, resulting in a deformed radius r_0 and thickness h, as illustrated in

Fig. 5.1(b). To finalize the framework, we impose a uniform external pressure P_t along the thickness direction. As previously mentioned, transverse pressure is commonly observed in many membranes. This pressure can be effectively substituted with electric and magnetic fields, which simulate a similar outcome by inducing an electro-magneto-static pressure, as depicted in Fig. 5.1(c). The mapping ζ characterizes the electro-magneto-elastic deformation of the membrane, defined as:

$$\mathbf{x} = \zeta(\mathbf{X}), \quad \zeta : \beta_0(R, \Theta, Z) \longrightarrow \beta(r, \theta, z), \tag{5.1}$$

here, the position vectors for the reference configuration β_0 and the current configuration β are denoted by $\mathbf{X}$ and $\mathbf{x}$, respectively. Consequently, the deformation mapping that links the undeformed and deformed states of the membrane can be expressed as follows:

$$r = \zeta(R, t), \quad \theta = \Theta, \quad z = \zeta(Z, t). \tag{5.2}$$

The deformation gradient tensor $\mathbf{F}$, the left Cauchy–Green deformation tensor $\mathbf{B}$, the electric field vector $\mathbf{E}$, and the magnetic field vector $\mathbf{H}$ for the given deformation map (5.1) are defined as:

$$\mathbf{F} = \begin{bmatrix} \lambda_r & 0 & 0 \\ 0 & \lambda_\theta & 0 \\ 0 & 0 & \lambda_z \end{bmatrix}, \quad \mathbf{B} = \mathbf{F}\mathbf{F}^T, \quad \mathbf{E} = \begin{bmatrix} 0 \\ 0 \\ E_0 \end{bmatrix}, \quad \mathbf{H} = \begin{bmatrix} 0 \\ 0 \\ H_0 \end{bmatrix}, \tag{5.3}$$

where λ_r, λ_θ, and λ_z are the principal stretches; E_0 and H_0 are the applied electric and magnetic field intensities on the membrane. The principal stretches of an incompressible ($\lambda_r\lambda_\theta\lambda_z$=1) circular membrane experiencing equi-biaxial deformation are defined as:

$$\lambda_r = \lambda_1 = \lambda, \quad \lambda_\theta = \lambda_2 = \lambda, \quad \lambda_z = \frac{1}{\lambda_1\lambda_2} = \frac{1}{\lambda^2}, \tag{5.4}$$

where $\lambda = \dfrac{r}{R}$ and $\lambda_z = \dfrac{h}{H}$, respectively. The invariants associated with the left Cauchy–Green deformation tensor $\mathbf{B}$, the electrical field-based pseudo structural tensor ($\mathbf{E}^l \otimes \mathbf{E}^l$), and the magnetic field-based pseudo structural tensor ($\mathbf{H}^l \otimes \mathbf{H}^l$) for an

isotropic, incompressible, and electro-magneto-elastic deformation are defined as [70]:

$$I_1 = \text{tr } \mathbf{B} = \lambda_1^2 + \lambda_2^2 + \lambda_1^{-2}\lambda_2^{-2}, \quad I_2 = \frac{1}{2}\left[(\text{tr } \mathbf{B})^2 - \text{tr } \mathbf{B}^2\right] = \lambda_1^2\lambda_2^2 + \lambda_1^{-2} + \lambda_2^{-2},$$
$$I_3 = \det \mathbf{B} = 1, \quad I_4 = \left[\mathbf{E}^l \otimes \mathbf{E}^l\right] : \mathbf{I} = \lambda_1^{-2}\lambda_2^{-2}{E_0}^2, \quad I_5 = \left[\mathbf{E}^l \otimes \mathbf{E}^l\right] : \mathbf{B}^{-1} = {E_0}^2,$$
$$I_6 = \left[\mathbf{E}^l \otimes \mathbf{E}^l\right] : \mathbf{B}^{-2} = \lambda_1^2\lambda_2^2{E_0}^2, \quad I_7 = \left[\mathbf{H}^l \otimes \mathbf{H}^l\right] : \mathbf{I} = \lambda_1^{-2}\lambda_2^{-2}{H_0}^2,$$
$$I_8 = \left[\mathbf{H}^l \otimes \mathbf{H}^l\right] : \mathbf{B}^{-1} = {H_0}^2, \quad I_9 = \left[\mathbf{H}^l \otimes \mathbf{H}^l\right] : \mathbf{B}^{-2} = \lambda_1^2\lambda_2^2{H_0}^2, \tag{5.5}$$

where $\mathbf{E}^l = \mathbf{F}^T\mathbf{E}$, and $\mathbf{H}^l = \mathbf{F}^T\mathbf{H}$ represent the Lagrangian electric and magnetic field vectors in the reference configuration. Smart circular membranes typically demonstrate a finite limit to their stretchability, known as limiting extensibility. Notably, the maximum stretch under biaxial loading is generally lower than that observed under uniaxial conditions. To accurately capture this behavior, phenomenological models have been developed that account for the membrane's restricted deformability. Among these, the Gent model is widely recognized for its effectiveness in representing materials with limiting chain extensibility [71].

5.3 Governing equation

In this study, we adopt a Gent-type strain energy density function W, formulated in terms of the invariants I_1, I_5, and I_8 as [82]:

$$W = -\frac{\mu_e}{2}J_m \log\left(1 - \frac{I_1 - 3}{J_m}\right) - \frac{\varepsilon_0}{2}(C_1 I_5) - \frac{\alpha_0}{2}(C_2 I_8), \tag{5.6}$$

where μ_e is the effective shear modulus defined as [68]: $\mu_e = \mu_m\left[1 + \frac{\Phi(\frac{\mu_f}{\mu_m} - 1)}{1 + \kappa(1-\Phi)(\frac{\mu_f}{\mu_m} - 1)}\right]$, J_m denotes the chain extensibility parameter of the membrane material, while C_1 and C_2 are constant material parameters. The symbols ε_0 and α_0 represent the electric permittivity and magnetic permeability of free space, respectively. In the expression for the effective shear modulus, Φ denotes the amount of fillers, and μ_f and μ_m correspond to the shear moduli of the filler and matrix phases of the membrane. The parameter κ is associated with the membrane's

Poisson's ratio. For incompressible elastomeric membranes, κ is typically taken as 0.4 [20]. Following the theory of electro-magneto-elasticity [1], the total Cauchy stress tensor $\mathbf{T}$ for an incompressible and isotropic circular membrane can be expressed as:

$$\mathbf{T} = -p\mathbf{I} + 2W_1\mathbf{B} + 2W_2[I_1\mathbf{B} - \mathbf{B}^2] - 2W_5\mathbf{E}\otimes\mathbf{E} - 2W_6[\mathbf{B}^{-1}\mathbf{E}\otimes\mathbf{E} + \mathbf{E}\otimes\mathbf{B}^{-1}\mathbf{E}] + 2W_8[\mathbf{BH}\otimes\mathbf{BH}] + 2W_9[\mathbf{BH}\otimes\mathbf{B}^2\mathbf{H} + \mathbf{B}^2\mathbf{H}\otimes\mathbf{BH}], \tag{5.7}$$

where p is a Lagrange multiplier introduced to enforce the incompressibility constraint, and W_i denotes the partial derivative of the strain energy function with respect to the invariant I_i, i.e., $\dfrac{\partial W}{\partial I_i}$ for $i = 1, 2...9$. By substituting Eq. (5.6) into Eq. (5.7), and utilizing Eqs. (5.3), (5.4), and (5.5), we derive the expressions for the principal stress components, electric displacement, and magnetic displacement as follows:

$$T_{rr} = -p + \frac{J_m\mu_e\lambda_1^2}{J_m - I_1 + 3}, \tag{5.8a}$$

$$T_{\theta\theta} = -p + \frac{J_m\mu_e\lambda_2^2}{J_m - I_1 + 3}, \tag{5.8b}$$

$$T_{zz} = -p + \frac{J_m\mu_e\lambda_1^{-2}\lambda_2^{-2}}{J_m - I_1 + 3} + C_1\varepsilon_0E_0^2 - C_2\alpha_0\lambda_1^{-4}\lambda_2^{-4}H_0^2. \tag{5.8c}$$

By implementing the specified traction-free boundary condition $T_{zz} = 0$ (Fig. 5.1(c)) in Eq. 5.8(c), we obtain the radial and hoop stress components from Eq. 5.8(a-b) as:

$$T_{rr} = \frac{\mu_e J_m\left(\lambda_1^2 - \lambda_1^{-2}\lambda_2^{-2}\right)}{J_m - \lambda_1^2 - \lambda_2^2 - \lambda_1^{-2}\lambda_2^{-2} + 3} - \varepsilon_0C_1E_0^2 + \alpha_0C_2\lambda_1^{-4}\lambda_2^{-4}H_0^2, \tag{5.9a}$$

$$T_{\theta\theta} = \frac{\mu_e J_m\left(\lambda_2^2 - \lambda_1^{-2}\lambda_2^{-2}\right)}{J_m - \lambda_1^2 - \lambda_2^2 - \lambda_1^{-2}\lambda_2^{-2} + 3} - \varepsilon_0C_1E_0^2 + \alpha_0C_2\lambda_1^{-4}\lambda_2^{-4}H_0^2. \tag{5.9b}$$

For the sake of convenience, the following non-dimensional electric and magnetic field variables (normalized voltage and normalized flux) and normalized effective shear modulus may be introduced in the above governing Eqs. (5.9), which are defined as:

$$U = \left[1 + \frac{\Phi(\frac{\mu_f}{\mu_m} - 1)}{1 + \kappa(1-\Phi)(\frac{\mu_f}{\mu_m} - 1)}\right], \quad V = E_0\sqrt{\frac{C_1\varepsilon_0}{\mu_m}}, \quad M = H_0\sqrt{\frac{C_2\alpha_0}{\mu_m}}, \tag{5.10}$$

where $E_0 = (\frac{v}{h}) = \lambda_1\lambda_2(\frac{v}{H})$ and $H_0 = (\frac{\Psi}{h}) = \lambda_1\lambda_2(\frac{\Psi}{H})$ represent the electric and magnetic fields, respectively. Invoking the above-defined normalized voltage and normalized flux parameter (Eq. 5.10) in the governing Eqs. (5.9), the normalized principal stress components (T^*_{rr} and $T^*_{\theta\theta}$) are obtained as:

$$T^*_{rr} = \frac{UJ_m\left(\lambda_1^2 - \lambda_1^{-2}\lambda_2^{-2}\right)}{J_m - \lambda_1^2 - \lambda_2^2 - \lambda_1^{-2}\lambda_2^{-2} + 3} - \lambda_1^2\lambda_2^2V^2 + \lambda_1^{-2}\lambda_2^{-2}M^2, \tag{5.11a}$$

$$T^*_{\theta\theta} = \frac{UJ_m\left(\lambda_2^2 - \lambda_1^{-2}\lambda_2^{-2}\right)}{J_m - \lambda_1^2 - \lambda_2^2 - \lambda_1^{-2}\lambda_2^{-2} + 3} - \lambda_1^2\lambda_2^2V^2 + \lambda_1^{-2}\lambda_2^{-2}M^2. \tag{5.11b}$$

It is important to note that when a uniform transverse stress is applied at the boundary, the stress component satisfies $T_{zz} = -P_t$ (see Fig. 5.1(b)). The corresponding expression for the transverse pressure is given by: $P_t = \left|P_{t_{elect.}} + P_{t_{mag.}}\right| = C_1\varepsilon_0E_0^2 - C_2\alpha_0H_0^2$ [82]. This highlights that the transverse pressure effectively captures the combined influence of electric and magnetic fields. Consequently, the interaction of these fields can mimic the mechanical compression of membranes, making electromagnetic loading functionally equivalent to an externally applied transverse stress.

In the analysis of taut regions in elastomers, the first Piola–Kirchhoff (PK-1) stress tensor is preferred due to its formulation in the reference configuration, making it compatible with energy-based methods and deformation-gradient-based models [44]. This stress measure allows for consistent evaluation of mechanical behavior relative to the undeformed geometry, which is crucial during the design and prediction phases. Unlike the Cauchy stress, which requires knowledge of the deformed state, PK-1 stress supports predictive modeling and aligns with variational formulations commonly used in electroactive elastomer studies. Therefore, the first Piola–Kirchhoff (PK-1) stress components S^*_{ii} from the above developed principal stress components (Eq. 5.11) may be obtained based on the following conversion given by:

$$S^*_{ii}(\lambda_1, \lambda_2, V, M, \Phi, \frac{\mu_f}{\mu_m}) = T^*_{ii}(\lambda_1, \lambda_2, V, M, \Phi, \frac{\mu_f}{\mu_m})\lambda_i^{-1} \quad i = 1, 2. \tag{5.12}$$

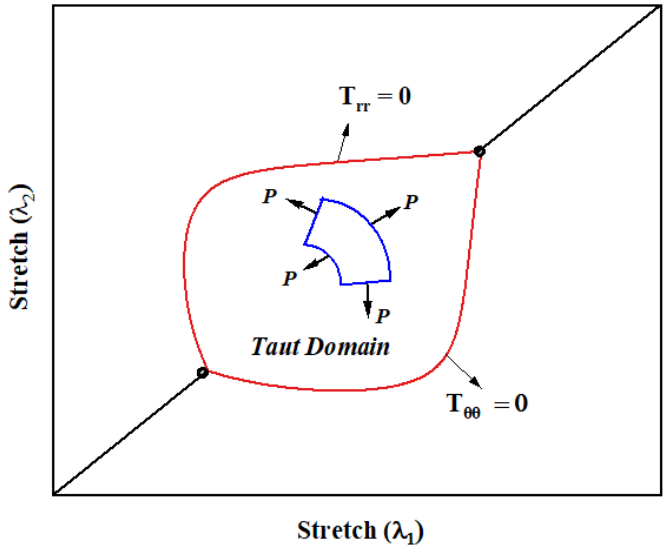


Figure 5.2: A schematic representation of the natural strain curves of the tensile stretch region.

5.4 Taut domains in a smart circular membrane

This subsection presents the concept of taut domains, referring to regions within the smart circular electro-magneto-active membrane that experience purely tensile stretches, as illustrated in Fig. 5.2 and originally introduced by Steigmann [83]. To derive the constitutive behavior within these domains, a state of local uniaxial tension along the θ-direction is considered. Under this condition, the transverse stretch in the r-direction assumes a specific value known as the natural width in tension, which corresponds to a uniaxial stress state where $T^*_{rr} = T^*_{zz} = 0$. As a result, the governing equation for the taut regions of the electro-magneto-active circular membrane, originally given by Eq. 5.11a, is reformulated as follows:

$$\frac{UJ_m\left(\lambda_1^2 - \lambda_1^{-2}\lambda_2^{-2}\right)}{J_m - \lambda_1^2 - \lambda_2^2 - \lambda_1^{-2}\lambda_2^{-2} + 3} - \lambda_1^2\lambda_2^2V^2 + \lambda_1^{-2}\lambda_2^{-2}M^2 = 0. \tag{5.13}$$

The smart thin membrane is taken into consideration in the situation of a basic boundary value problem, where an applied electromagnetic field causes zero traction on the upper and lower faces. Using the concept of equi-biaxial equilibrium configurations, i.e., $\lambda_1 = \lambda_2 = \lambda$ and $P_1 = P_2 = P$ in principal directions, the Piola–Kirchhoff

stress components are derived using Eq. 5.12 as:

$$\begin{aligned} S^*_{rr}(\lambda_1, \lambda_2, V, M, \Phi, \frac{\mu_f}{\mu_m}) = S^*_{\theta\theta}(\lambda_1, \lambda_2, V, M, \Phi, \frac{\mu_f}{\mu_m}) = S^*(\lambda, V, M, \Phi, \frac{\mu_f}{\mu_m}), \\ \Rightarrow \frac{UJ_m(\lambda - \lambda^{-5})}{J_m - 2\lambda^2 - \lambda^{-4} + 3} - \lambda^3 V^2 + \lambda^{-5} M^2. \end{aligned} \tag{5.14}$$

Further, the equibiaxial stretch λ satisfies the boundary condition of zero traction along the membrane edges and corresponds to the following derived solution.

$$\begin{aligned} S^*(\lambda, V, M, \Phi, \frac{\mu_f}{\mu_m}) = 0, \\ \Rightarrow \frac{UJ_m(\lambda - \lambda^{-5})}{J_m - 2\lambda^2 - \lambda^{-4} + 3} - \lambda^3 V^2 + \lambda^{-5} M^2 = 0. \end{aligned} \tag{5.15}$$

In the simplified case of homogeneous equibiaxial deformation, the stability criterion for identifying taut domains is given by:

$$\frac{dS^*(\lambda, \lambda)}{d\lambda} > 0. \tag{5.16}$$

The upcoming section presents a numerical solution of the governing Eq. (5.13) to evaluate the distribution of taut domains in the smart circular thin membrane composed of particle-reinforced electro-magneto-active material.

5.5 Results and discussion

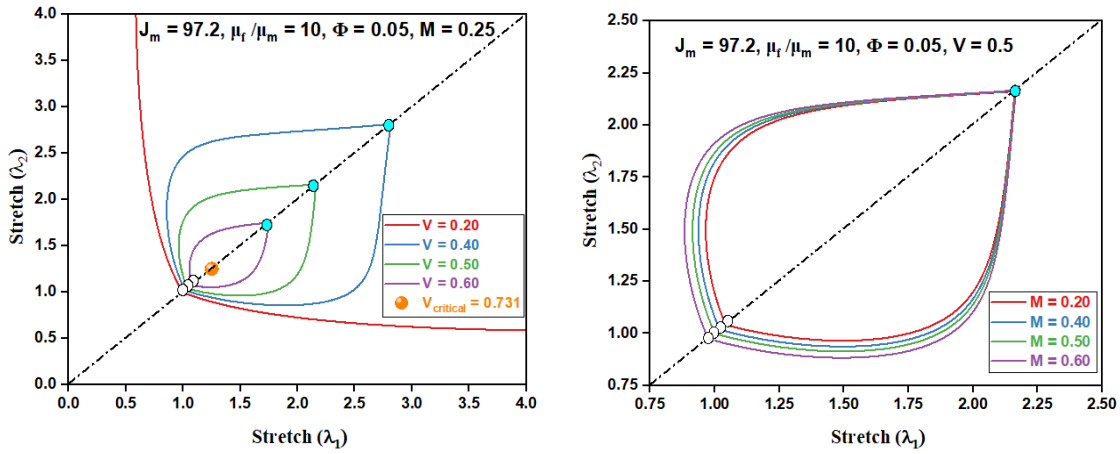
This section begins by examining the influence of varying electric and magnetic fields on the extent of the taut domain. Subsequently, the effects of filler content and the shear modulus ratio under electromagnetic loading conditions are analyzed. To investigate the role of filler content, five volume fractions are considered: $\Phi = 0.01$, 0.05, 0.10, 0.20, and 0.40 [84]. The influence of the shear modulus ratio between the filler and matrix is evaluated using $\mu_f/\mu_m = 1$, 5, and 20 [82].

5.5.1 Effect of electric and magnetic fields on the taut domain

This subsection investigates the influence of electric and magnetic fields on the taut domain behavior of the membrane. The influence of applied electromagnetic loading

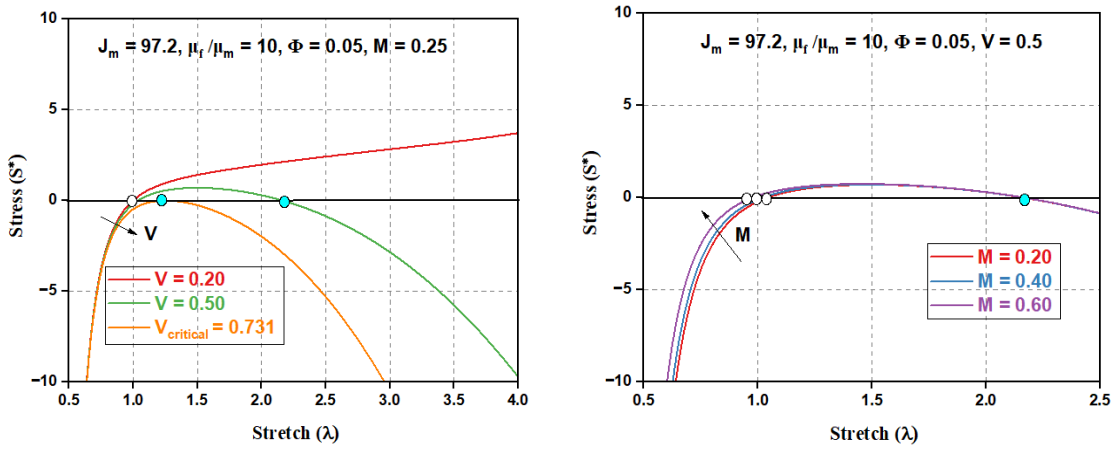
on the taut domain behavior of the smart membrane is analyzed under conditions of significant mechanical reinforcement, characterized by a high shear modulus ratio ($\mu_f/\mu_m = 10$) and moderate filler content ($\Phi = 0.05$), as shown in Fig. 5.3. Initially, the influence of varying electric field levels on the taut domain of the membrane is examined while maintaining a constant magnetic flux density of $M = 0.25$, as shown in Fig. 5.3(a). The results indicate that the taut region progressively contracts with increasing normalized voltage V, eventually collapsing to a point at a critical voltage $V_{\text{critical}} = 0.731$. Beyond this threshold, the membrane no longer exhibits any taut states. In contrast, Fig. 5.3(b) presents the effect of varying magnetic field levels at a constant electric voltage of $V = 0.50$. Here, the taut domain expands with increasing magnetic loading, suggesting that the magnetic field contributes positively to the membrane's mechanical stability. This stabilizing effect is attributed to the magneto-mechanical coupling, which introduces additional tensile forces that counteract the destabilizing influence of the electric field, thereby promoting larger stable deformation regions within the membrane.

Finally, using the stability criterion defined in Eq. 5.16, the stress–stretch curves of the membrane under equibiaxial loading are evaluated for varying levels of applied electromagnetic fields, as shown in Fig. 5.4. To facilitate interpretation, the stress–stretch response corresponding to the conditions in Fig. 5.3a is reproduced in Fig. 5.4a. It is observed that, for a fixed normalized magnetic flux, two equilibrium solutions exist where the stress becomes zero. However, as the normalized electric voltage approaches the critical value $V_{\text{critical}} = 0.731$, these two solutions merge into a single point. Beyond this voltage, no real solution to Eq. 5.15 exists, signifying the onset of pull-in instability—a phenomenon widely reported in experimental studies [85–88]. The critical voltage thus corresponds to the maximum stretch that the membrane can stably attain before experiencing electromechanical failure. Similarly, the stress–stretch response under varying magnetic field strengths is presented in Fig. 5.4b. The results reveal the existence of two distinct equilibrium solutions across all levels of the applied magnetic field. The upper equilibrium branch (denoted by filled circles) remains unaffected by changes in M, indicating that it is primarily governed



(a) (b)

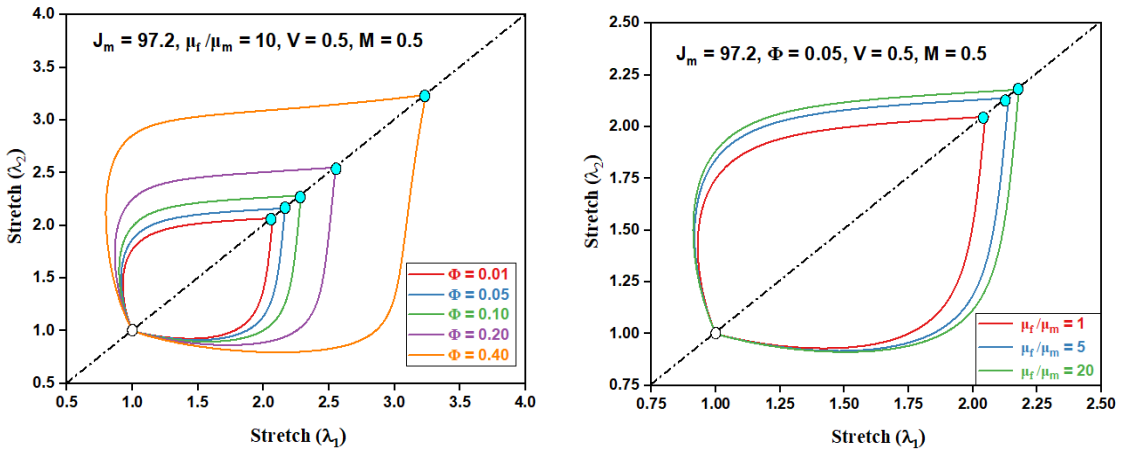
Figure 5.3: Taut domains of the smart circular membrane for (a) varying electric field V at $M = 0.25$, and (b) varying magnetic field M at $V = 0.50$, with $\Phi = 0.05$, $\mu_f/\mu_m = 10$ and $J_m = 97.2$. Empty circles indicate equibiaxial equilibrium solutions that satisfy the stability criterion (Eq. 5.16), while blue-filled circles denote solutions that fail to meet this criterion.



(a) (b)

Figure 5.4: Stress-stretch plots of the smart circular membrane for (a) varying electric field V at $M = 0.25$, and (b) varying magnetic field M at $V = 0.50$, with $\Phi = 0.05$, $\mu_f/\mu_m = 10$ and $J_m = 97.2$.

by the electric field V. In contrast, the lower equilibrium branch (denoted by empty circles) exhibits a strong dependence on M, showing a noticeable reduction in stretch



(a) (b)

Figure 5.5: Taut domains of the smart circular membrane for (a) varying amounts of filler Φ, and (b) varying shear modulus ratio μ_f/μ_m under electromagnetic loading conditions ($V = 0.50$, $M = 0.50$) with $J_m = 97.2$.

with increasing magnetic field intensity. This highlights the magnetic field's influence in modulating the membrane's mechanical stability within the lower equilibrium regime.

5.5.2 Effect of filler volume fraction and shear modulus ratio on the taut domain

This subsection investigates the influence of filler content and shear modulus ratio on the taut domain behavior of a circular membrane under coupled electromagnetic loading. In the first case, we vary the filler volume fraction Φ while keeping $V = 0.50$, $M = 0.50$, and $\mu_f/\mu_m = 10$ constant (see Fig. 5.5a). The results show that increasing Φ significantly expands the taut domain. This can be attributed to the overall stiffening effect introduced by the fillers, which enhances the membrane's resistance to compressive stresses and delays the onset of wrinkling. The improved stiffness redistributes internal stresses more uniformly, thereby stabilizing the membrane under applied loading. In the second case, we assess the effect of the shear modulus ratio μ_f/μ_m while fixing $V = 0.50$, $M = 0.50$, and $\Phi = 0.05$ (see Fig. 5.5b). A similar

expansion of the taut region is observed with increasing modulus ratio. This occurs because a higher stiffness contrast between filler and matrix increases the membrane's effective rigidity, suppressing compressive instabilities. The resulting mechanical reinforcement enables the membrane to maintain a taut configuration over a broader range of deformation, enhancing its wrinkle resistance under electromagnetic actuation.

To achieve effective surface morphology control in wrinkle-tunable materials, it is essential to optimize both the filler volume fraction and the shear modulus ratio. In this context, Fig. 5.6 illustrates the combined effect of varying the filler content Φ and the shear modulus ratio μ_f/μ_m on the critical normalized voltage, V_{critical}, defined as the voltage at which the taut domain collapses to a point, under a constant magnetic flux level of $M = 0.50$. As expected, the figure shows that membranes with higher filler content require a substantially larger V_{critical} to eliminate the taut region, reflecting their enhanced stiffness and resistance to wrinkling. Additionally, increasing the shear modulus ratio also leads to a rise in V_{critical}, indicating improved mechanical stability. However, this increase becomes marginal at higher modulus ratios, suggesting a saturation effect wherein further stiffness contrast yields diminishing influence on the critical voltage. This behavior underscores the need for a balanced design strategy that considers both filler concentration and modulus contrast to fine-tune wrinkle resistance in smart elastomer membranes.

Finally, the stress–stretch response of the membrane under equibiaxial deformation is analyzed for different filler contents and shear modulus ratios, with constant applied electromagnetic loading, as illustrated in Figs. 5.7(a–b). In Fig. 5.7a, the stress-stretch curves for different filler volume fractions Φ are plotted for a fixed shear modulus ratio $\mu_f/\mu_m = 10$, with normalized electric and magnetic loads $V = 0.50$, $M = 0.50$. The system exhibits two equilibrium branches: the lower stretch solutions (empty circles), which satisfy the stability criterion (Eq. 5.16), and the higher stretch solutions (filled circles), which are unstable and do not satisfy this criterion. Increasing Φ leads to unchanged lower stretch responses but higher stretch values in the unstable branch, indicating a stiffening effect. Fig. 5.7b shows the response for varying shear modulus ratios at fixed $\Phi = 0.05$, $V = 0.50$, $M = 0.50$. A similar bifurcation is

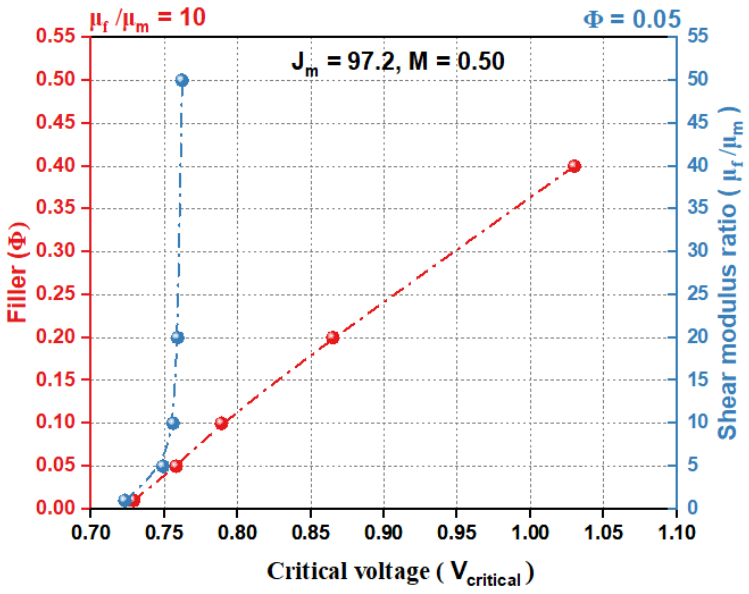
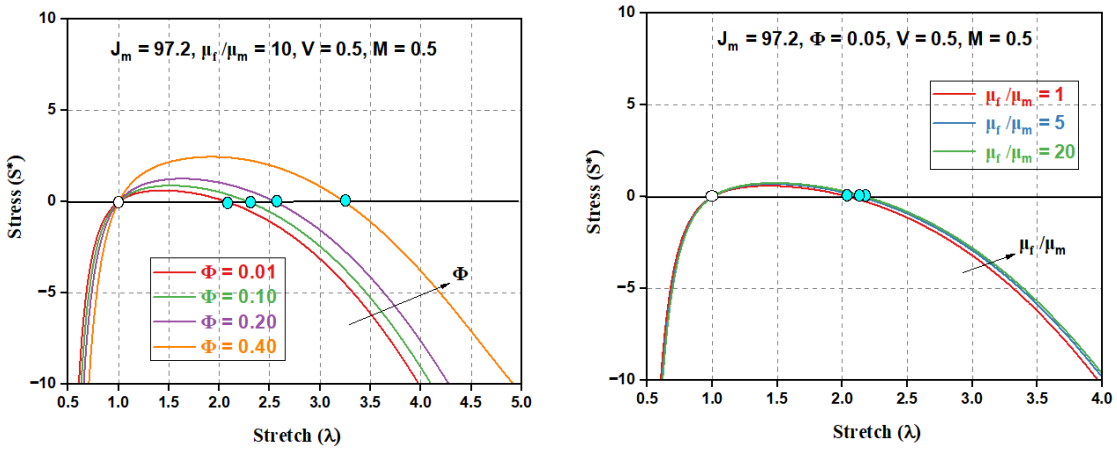


Figure 5.6: Critical normalized voltage $V_{critical}$ of the smart circular membrane for varying amounts of fillers Φ, and varying shear modulus ratio μ_f/μ_m excited by a magnetic flux of $M = 0.50$ with $J_m = 97.2$.



(a) (b)

Figure 5.7: Stress-stretch plots of the smart circular membrane for (a) varying amounts of filler Φ at $\mu_f/\mu_m = 10$, and (b) varying shear modulus ratio μ_f/μ_m at $\Phi = 0.05$ under electromagnetic loading conditions ($V = 0.50$, $M = 0.50$) with $J_m = 97.2$.

observed: stable lower stretch solutions remain consistent, while the unstable higher stretch solutions increase with the modulus ratio. This reflects enhanced stiffness and

delayed onset of instability with greater filler-matrix contrast.

The results show that electric and magnetic loading have different effects on the taut domain for the parameters considered. Increasing the normalized electric voltage contracts the taut region and brings the membrane closer to the critical condition. In contrast, increasing the normalized magnetic loading expands the taut region. Higher filler volume fraction and filler-to-matrix shear modulus ratio also enlarge the taut domain and increase the critical voltage. These trends describe the response predicted by the present constitutive model within the investigated parameter range.

5.6 Summary

This study presents a robust continuum physics-based modeling framework to analyze the intricate nonlinear behavior of a particle-reinforced smart circular membrane subjected to simultaneous electric and magnetic fields. Departing from the conventional application of transverse pressure, the membrane is actuated through tailored electromagnetic loading to better capture its functional response. Central to this approach is the concept of the taut domain, which is employed to derive coupled nonlinear equations that rigorously assess the membrane's stability. The key insights drawn from the present study are summarized as follows:

i. The taut domains of the smart circular membrane under an applied magnetic flux decrease with increasing levels of electrical loading.

ii. In contrast, the taut domains of the smart circular membrane under an applied electric voltage expand with increasing levels of magnetic loading.

iii. An increase in filler content and shear modulus ratio enlarges the taut domains of the smart circular membrane under applied electromagnetic loading conditions.

iv. Thus, it can be concluded that the extent of taut domains in the smart circular membrane can be effectively tuned by adjusting the filler content and shear modulus ratio, in combination with the applied electromagnetic loading conditions.

This chapter focuses on taut domain formation and stability in particle-reinforced electro-magneto-active circular membranes under combined electric and magnetic loading. The results showed that increasing the electric field (V) reduces the stable region, while increasing the magnetic flux (M) enhances the stable taut region. In contrast, higher filler volume fraction (Φ) and shear modulus ratio (μ_f/μ_m) improve membrane stiffness and increase the stable deformation range. The stress–stretch response also confirmed that reinforced membranes can sustain larger stable stretches compared to unreinforced membranes. Overall, the study demonstrates the important role of particle reinforcement in improving membrane stability and controlling taut domain behavior.

The next chapter focuses on the stability behavior of biological membranes by considering the effects of isotropic and anisotropic growth along with fiber reinforcement. It examines how growth parameters, material anisotropy, and fiber orientation influence snap-through instability, bifurcation behavior, and overall membrane deformation under electric loading.

Chapter 6

Stability and Field-Induced Instabilities in Biological Membranes

Preface

Fiber reinforcement and growth significantly influence the mechanical response of soft active membranes. This chapter examines the effects of fiber orientation, isotropic and anisotropic growth, and electric loading on equilibrium, snap-through instability, and bifurcation. The study provides insight into the stability characteristics of fiber-reinforced active membranes.

6.1 Introduction

Biological membranes exhibit rich and complex stability behavior due to the combined effects of large deformation, material anisotropy, and internal growth. Unlike purely passive systems, these membranes may evolve under the influence of growth-induced stresses or external electromagnetic fields, leading to significant changes in their equilibrium configuration. As a result, their response is often characterized by nonlinear deformation patterns and sudden transitions between stable states.

Although the deformation and stability of electroactive membranes have been

widely studied, limited work is available on the combined effects of growth and fiber reinforcement in biological membranes under electric loading. Most previous studies consider growth effects or material anisotropy separately, while the combined influence of growth, fiber orientation, and electric actuation on snap-through instability and bifurcation behavior is still not fully understood. The novelty of this chapter lies in developing a theoretical framework that incorporates isotropic and anisotropic growth together with fiber reinforcement in electroactive membranes. The chapter investigates how growth parameters, material anisotropy, and fiber orientation influence membrane deformation, snap-through instability, and bifurcation behavior under electric loading. The main objectives of this chapter are:

- To develop the governing formulation for electroactive membranes considering growth and fiber reinforcement.
- To study the effects of growth parameters and electric loading on snap-through instability and bifurcation behavior.
- To examine the influence of fiber orientation and material anisotropy on membrane deformation and stability characteristics.

6.2 Mathematical formulation

In the present analysis, the electroactive membrane is assumed to behave as a homogeneous, incompressible, and hyperelastic material undergoing large elastic deformation. Since the membrane thickness is very small compared to its in-plane dimensions, bending effects are neglected. Isotropic and anisotropic growth are incorporated in the formulation, and the reinforcing fibers are assumed to be uniformly distributed within the membrane. The membrane deformation is considered axisymmetric under uniform electric loading, while thermal effects, body forces, and material damping are not included in the present study.

In this study, we consider a circular biological membrane with coordinate systems (R, Θ, Z) in the reference state Ω_0 and (r, θ, z) in the current/deformed state Ω, respec-

tively. The membrane has an undeformed radius R_0 with thickness H in the specified loading situation. It expands radially and compresses in the thickness direction, as illustrated in Fig. 6.1. The membrane is assumed to be axisymmetric and undergoes morpho-elastic growth with anisotropic reinforcement fibers at the micro-structural level. The membrane is stretched by a radially applied mechanical load P and a uniformly generated Pelrine pressure P_t in the thickness direction. This Pelrine pressure P_t is rationally evident in most biological membranes and is expressed as $P_t = \epsilon_0 \epsilon_r \mathbf{E}^2$ in terms of the electric field, where ϵ_0 denotes the electric permittivity of the free space, ϵ_r represents the relative permittivity, and $\mathbf{E}$ is an applied electric field intensity in the current configuration. The mapping χ identifies the electro-morpho-elastic deformation of the membrane, which is defined as:

$$\mathbf{x} = \chi(\mathbf{X}), \quad \chi : \Omega_0(R, \Theta, Z) \longrightarrow \Omega(r, \theta, z), \tag{6.1}$$

where $\mathbf{X}$ and $\mathbf{x}$ represent the position vectors in the reference Ω_0 and current Ω configurations, respectively. As a result, the corresponding deformation map for the membrane connecting the undeformed and deformed variables is given by:

$$r = \chi(R, t), \quad \theta = \Theta, \quad z = \chi(Z, t). \tag{6.2}$$

To characterize morphological tissue growth of the membrane, Rodriguez et al. [89] proposed a multiplicative decomposition of the deformation gradient $\mathbf{F} = \text{Grad } \mathbf{x} = \dfrac{\partial \mathbf{x}}{\partial \mathbf{X}}$ into an elastic part $\mathbf{F}_e$ and a pure volumetric growth part $\mathbf{F}_g$, as follows:

$$\mathbf{F} = \mathbf{F}_e \mathbf{F}_g = \begin{bmatrix} \lambda_r & 0 & 0 \\ 0 & \lambda_\theta & 0 \\ 0 & 0 & \lambda_z \end{bmatrix} \begin{bmatrix} g_r & 0 & 0 \\ 0 & g_\theta & 0 \\ 0 & 0 & g_z \end{bmatrix}, \tag{6.3}$$

where $(\lambda_r, \lambda_\theta, \lambda_z)$ are the principal stretches and (g_r, g_θ, g_z) denote the growth rates in the principal directions. As depicted in Fig. 6.2, the growth tensor $\mathbf{F}_g$ maps the tangent space and physically defines a naturally grown state incompatible with the constraint. For the sake of simplicity, the current work takes into account a homogeneous growth tensor of the form $\mathbf{F}_g = \text{diag } (g_r, g_r, g_z)$. Additionally, elastic deformation is assumed to restore tissue deformation compatibility ($\det \mathbf{F}_e = 1$), including

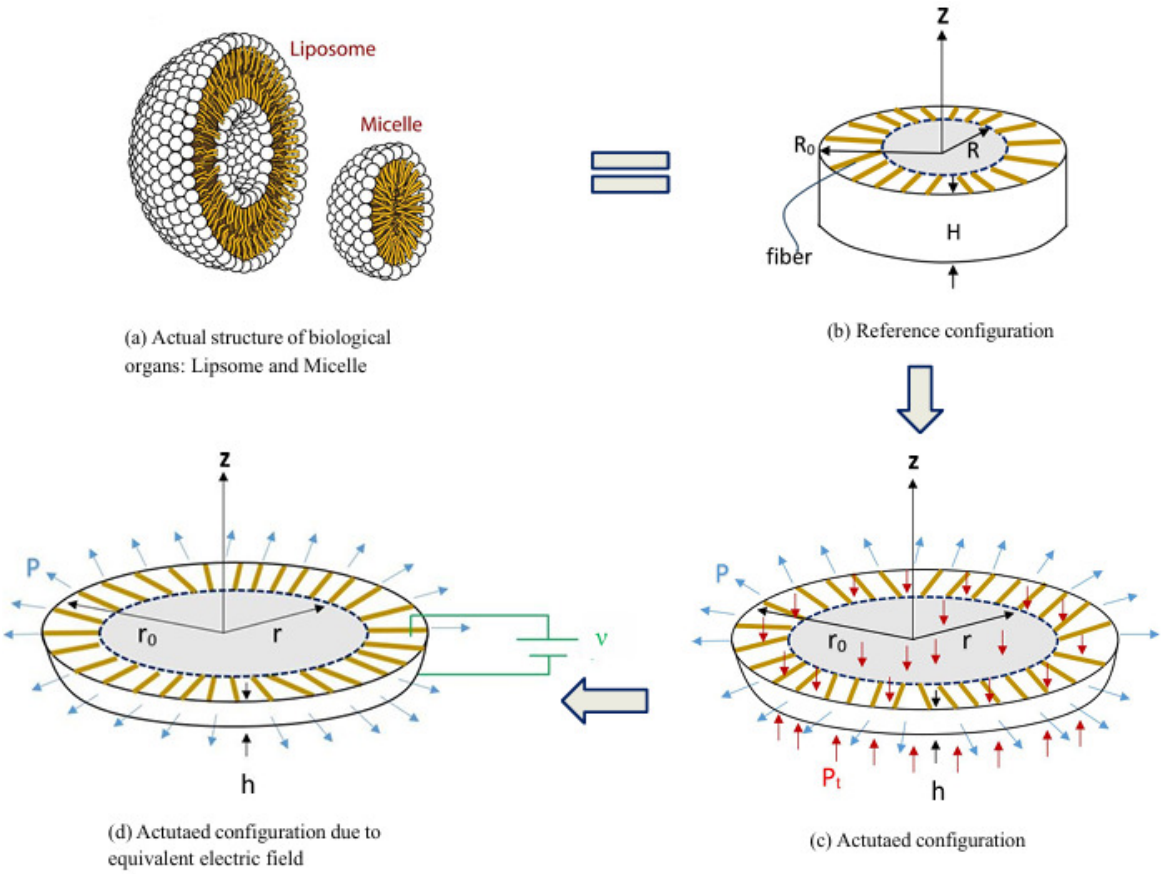


Figure 6.1: (a) Actual structure of the biological organs and schematic representation of the biological membrane: (b) Initial state, (c) Deformed state caused by a radial load P and a uniformly applied transverse pressure P_t, and (d) Equivalent deformed state achieved due to the application of a radial load, along with the transverse electric field.

$g_r^2 g_z = 1$ (det $\mathbf{F}_g = 1$), while residual stresses arise. As previously stated, we model the biological membrane as a homogeneous and incompressible tissue composed of a continuous distribution of fibers (anisotropic) immersed in a homogeneous isotropic parent substance. Also, the membrane is assumed to be vulnerable to an electric field [90]. These membranes partition cells and organelles, keeping ions and molecules apart and preserving electrical potential. For the given deformation map (Eq. 6.2), the electric field vector $\mathbf{E}$, the left Cauchy–Green deformation tensor $\mathbf{B}$ and the deformed fiber vector $\mathbf{a}$ transformed from the undeformed fiber vector $\mathbf{a}_0$ oriented at

angle θ_f with the X-axis are defined as:

$$\mathbf{B} = \mathbf{F}\mathbf{F}^T, \quad \mathbf{E} = \begin{bmatrix} 0 \\ 0 \\ E_0 \end{bmatrix}, \quad \mathbf{a}_0 = \begin{bmatrix} \cos\theta_f \\ \sin\theta_f \\ 0 \end{bmatrix}, \quad \mathbf{a} = \mathbf{F}\mathbf{a}_0. \tag{6.4}$$

For an incompressible and anisotropic biological membrane undergoing an equi-biaxial deformation, the principal stretches are defined as follows:

$$\lambda_r = \lambda, \quad \lambda_\theta = \lambda, \quad \lambda_z = \frac{1}{\lambda^2}, \tag{6.5}$$

where λ and λ_z are represented as $\lambda = \dfrac{r}{R}$ and $\lambda_z = \dfrac{h}{H}$, respectively. The set of invariants of the left Cauchy–Green deformation tensor $\mathbf{B}$, the electrical field-based pseudo structural tensor $(\mathbf{E}^l \otimes \mathbf{E}^l)$, and the structural tensor $(\mathbf{a} \otimes \mathbf{a})$ for an incompressible,

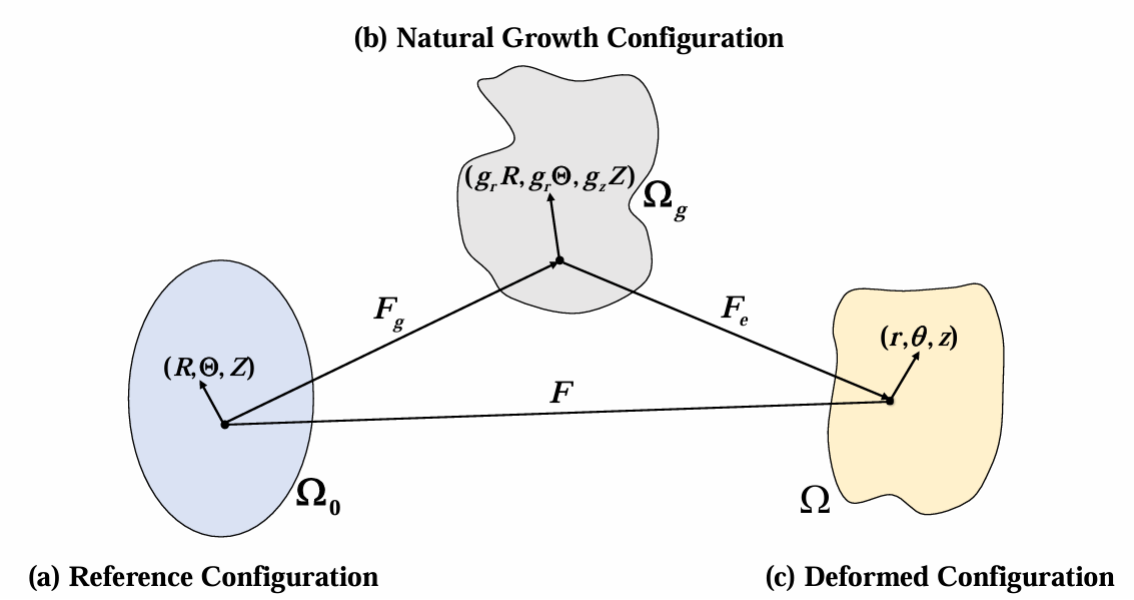


Figure 6.2: Schematic representation of the multiplicative decomposition of the deformation gradient $\mathbf{F}$ into the growth component $\mathbf{F}_g$, which defines a naturally grown state, and the elastic component $\mathbf{F}_e$, which restores the compatibility of the deformation.

anisotropic, and electro-elastic material deformation is given by [1, 72, 91, 92]:

$$I_1 = \text{tr } \mathbf{B}, \quad I_2 = \frac{1}{2}\left[(\text{tr } \mathbf{B})^2 - \text{tr } \mathbf{B}^2\right], \quad I_3 = \det \mathbf{B},$$
$$I_4 = \left[\mathbf{E}^l \otimes \mathbf{E}^l\right] : \mathbf{I}, \quad I_5 = \left[\mathbf{E}^l \otimes \mathbf{E}^l\right] : \mathbf{B}^{-1}, \quad I_6 = \left[\mathbf{E}^l \otimes \mathbf{E}^l\right] : \mathbf{B}^{-2}, \tag{6.6}$$
$$I_7 = \mathbf{a}_0.\mathbf{B}\mathbf{a}_0, \quad I_8 = \mathbf{a}_0.\mathbf{B}^2\mathbf{a}_0,$$

where $\mathbf{E}^l = \mathbf{F}^T\mathbf{E}$ represents the Lagrangian electric field vector defined in the reference configuration. In general, biological membranes exhibit limiting extensibility. In biaxial deformation, for instance, the limiting stretch will be less than in uniaxial deformation. The restricted extensibility of such membranes is the foundation for phenomenological modeling. The Gent material model [71] is the most commonly used model to imitate such biological materials in this domain.

6.3 Governing equation

In the current work, accordingly, we use the following Gent type of total strain energy density W similar to [92, 93], defined in terms of the above invariants I_1, I_5, I_7, and I_8 as:

$$W = -\frac{\mu}{2}J_m \log\left(1 - \frac{I_1 - 3}{J_m}\right) - \frac{\epsilon_0}{2}(C_1 I_5) + \frac{\mu_{f1}}{2}(I_7 - 1)^2 + \frac{\mu_{f2}}{2}(I_8 - 1)^4, \tag{6.7}$$

where μ is the material parameter in the undeformed state, J_m represents the chain extensibility parameter of the membrane material, ϵ_0 denotes the electric permittivity of free space, and μ_{f1} and μ_{f2} are the respective moduli of tensile and shear deformations. These material parameters can be obtained by fitting the above-modified energy function (Eq. 6.7) to a specific dielectric elastomer or biological material test data, as mentioned in [69, 72, 91, 92]. Following the theory of electro-elasticity [94, 95], we may express the total Cauchy stress tensor $\mathbf{T}$ for an incompressible and anisotropic

biological membrane, as follows:

$$\begin{aligned}\mathbf{T} = -p + 2W_1\mathbf{B} + 2W_2[I_1\mathbf{B} - \mathbf{B}^2] - 2W_5\mathbf{E}\otimes\mathbf{E} - 2W_6[\mathbf{B}^{-1}\mathbf{E}\otimes\mathbf{E} + \mathbf{E}\otimes\mathbf{B}^{-1}\mathbf{E}] \\ +2W_7[\mathbf{a}\otimes\mathbf{a}] + 2W_8[\mathbf{a}\otimes\mathbf{Ba} + \mathbf{Ba}\otimes\mathbf{a}], \\ \mathbf{D}_e = -2[W_4\mathbf{B} + W_5\mathbf{I} + W_6\mathbf{B}^{-1}]\mathbf{E},\end{aligned} \tag{6.8}$$

where p is a Lagrange multiplier obtained from the boundary conditions of incompressibility constraint and W_i is defined as $\dfrac{\partial W}{\partial I_i}$ for $i = 1, 2...8$. Substituting Eq. 6.7 in Eq. 6.8 with the use of Eqs. (6.4), (6.5), and (6.6), we obtain the principal stress components given by:

$$\begin{aligned}T_{rr} = & -p + \frac{\mu J_m\left(\lambda^2 g_r^2\right)}{J_m - I_1 + 3} + 2\mu_{f1}(I_7 - 1)\left(\lambda^2 g_r^2\cos^2\theta_f\right) \\ & + 8\mu_{f2}(I_8 - 1)^3\left(\lambda^4 g_r^4\cos^2\theta_f\right),\end{aligned} \tag{6.9a}$$

$$\begin{aligned}T_{\theta\theta} = & -p + \frac{\mu J_m\left(\lambda^2 g_r^2\right)}{J_m - I_1 + 3} + 2\mu_{f1}(I_7 - 1)\left(\lambda^2 g_r^2\sin^2\theta_f\right) \\ & + 8\mu_{f2}(I_8 - 1)^3\left(\lambda^4 g_r^4\sin^2\theta_f\right),\end{aligned} \tag{6.9b}$$

$$T_{zz} = -p + \frac{\mu J_m\left(\lambda^{-4} g_z^2\right)}{J_m - I_1 + 3} + C_1\epsilon_0 E_0^2. \tag{6.9c}$$

In the above Eq. 6.9(c), $C_1 = \epsilon_r$ denotes the relative electric permittivity of the membrane. By applying the given traction-free boundary condition $T_{zz} = 0$ in (6.9 c), we obtain the hydrostatic pressure p as:

$$p = \frac{\mu J_m\left(\lambda^{-4} g_z^2\right)}{J_m - I_1 + 3} + \epsilon_r\epsilon_0 E_0^2. \tag{6.10}$$

Upon invoking the above expression of p in 6.9 (a-b), we obtain the radial and hoop stress components as:

$$\begin{aligned}T_{rr} = & \frac{\mu J_m\left(\lambda^2 g_r^2 - \lambda^{-4} g_z^2\right)}{J_m - I_1 + 3} + 2\mu_{f1}\left(I_7 - 1\right)\left(\lambda^2 g_r^2\cos^2\theta_f\right) \\ & + 8\mu_{f2}\left(I_8 - 1\right)^3\left(\lambda^4 g_r^4\cos^2\theta_f\right) - \epsilon_r\epsilon_0 E_0^2,\end{aligned} \tag{6.11a}$$

$$\begin{aligned}T_{\theta\theta} = & \frac{\mu J_m\left(\lambda^2 g_r^2 - \lambda^{-4} g_z^2\right)}{J_m - I_1 + 3} + 2\mu_{f1}\left(I_7 - 1\right)\left(\lambda^2 g_r^2\sin^2\theta_f\right) \\ & + 8\mu_{f2}\left(I_8 - 1\right)^3\left(\lambda^4 g_r^4\sin^2\theta_f\right) - \epsilon_r\epsilon_0 E_0^2.\end{aligned} \tag{6.11b}$$

In the absence of an electric field, the stress tensor can be derived from relation (6.8) and is given by:

$$\mathbf{T} = -pI + 2W_1\mathbf{B} + 2W_2[I_1\mathbf{B} - \mathbf{B}^2] + 2W_7[\mathbf{a}\otimes\mathbf{a}] + 2W_8[\mathbf{a}\otimes\mathbf{Ba} + \mathbf{Ba}\otimes\mathbf{a}]. \quad (6.12)$$

To express the principal stress components for this case, we can derive them directly from Eq. 6.12 as follows:

$$\begin{aligned} T_{rr} = & -p + \frac{\mu J_m\left(\lambda^2 g_r^2\right)}{J_m - I_1 + 3} + 2\mu_{f1}(I_7 - 1)\left(\lambda^2 g_r^2\cos^2\theta_f\right) \\ & + 8\mu_{f2}(I_8 - 1)^3\left(\lambda^4 g_r^4\cos^2\theta_f\right), \end{aligned} \quad (6.13a)$$

$$\begin{aligned} T_{\theta\theta} = & -p + \frac{\mu J_m\left(\lambda^2 g_r^2\right)}{J_m - I_1 + 3} + 2\mu_{f1}(I_7 - 1)\left(\lambda^2 g_r^2\sin^2\theta_f\right) \\ & + 8\mu_{f2}(I_8 - 1)^3\left(\lambda^4 g_r^4\sin^2\theta_f\right), \end{aligned} \quad (6.13b)$$

$$T_{zz} = -p + \frac{\mu J_m\left(\lambda^{-4} g_z^2\right)}{J_m - I_1 + 3}. \quad (6.13c)$$

It is important to note that $\mathbf{T}$ excludes the electro-mechanical stress. Given the uniform transverse stress at the boundary, $T_{zz} = -P_t$, the Lagrange multiplier p can be determined as:

$$p = P_t + \frac{\mu J_m\left(\lambda^{-4} g_z^2\right)}{J_m - I_1 + 3}. \quad (6.14)$$

Upon invoking the above expression of p in Eq. 6.13(a), we obtain the radial and hoop stress components as:

$$\begin{aligned} T_{rr} = & \frac{\mu J_m\left(\lambda^2 g_r^2 - \lambda^{-4} g_z^2\right)}{J_m - I_1 + 3} + 2\mu_{f1}\left(I_7 - 1\right)\left(\lambda^2 g_r^2\cos^2\theta_f\right) \\ & + 8\mu_{f2}\left(I_8 - 1\right)^3\left(\lambda^4 g_r^4\cos^2\theta_f\right) - P_t, \\ T_{\theta\theta} = & \frac{\mu J_m\left(\lambda^2 g_r^2 - \lambda^{-4} g_z^2\right)}{J_m - I_1 + 3} + 2\mu_{f1}\left(I_7 - 1\right)\left(\lambda^2 g_r^2\sin^2\theta_f\right) \\ & + 8\mu_{f2}\left(I_8 - 1\right)^3\left(\lambda^4 g_r^4\sin^2\theta_f\right) - P_t, \end{aligned} \quad (6.15)$$

where $P_t = \epsilon_r\epsilon_0 E_0^2$ denotes the Pelrine pressure that acts on the membrane in the thickness direction, $E_0 = (\frac{v}{h}) = \lambda^2(\frac{v}{H})$. Therefore, $P_T = \varepsilon_0\varepsilon_r(\frac{v}{H})^2$ and $P_t = \lambda^4 P_T$.

The equilibrium equation of motion for an axisymmetric deformation of an incompressible and anisotropic morpho-elastic biological membrane is given by:

$$\nabla\cdot\mathbf{T} + \rho\mathbf{b}_f = \rho\frac{d^2\mathbf{r}}{dt^2}, \quad (6.16)$$

where $\nabla.(.)$, ρ, and b_f represent the divergence operator, density of the membrane material, and the body force per unit volume. For a given boundary condition $T_{rr}(r = r_0) = \frac{P}{2\pi r_0 h}$ when there is no body force $b_f = 0$, we may radially balance the equilibrium equation (6.16) with the use of (6.15) as:

$$\frac{P}{2\pi r_0 h} - T_{rr} = \int_0^{r_0} \rho \frac{d^2 r}{dt^2}\, dr \Rightarrow \frac{d^2\lambda}{dt^2} + \frac{2T_{rr}}{\lambda\rho R_0^2} - \frac{P}{\pi r_0 h \lambda \rho R_0^2} = 0. \tag{6.17}$$

Substituting T_{rr} from Eq. 6.15 in Eq. 6.17, we obtain the following.

$$\begin{aligned} &\frac{d^2\lambda}{d\tau^2} + \frac{J_m(\lambda^2 g_r^2 - \lambda^{-4} g_z^2)}{\left(J_m - 2\lambda^2 - \frac{1}{\lambda^4} + 3\right)} + 2\xi_1 \left(\lambda^2 g_r^2 \cos^2\theta_f + \lambda^2 g_r^2 \sin^2\theta_f - 1\right) \lambda^2 g_r^2 \cos^2\theta_f \\ &+8\xi_2 \left(\lambda^4 g_r^4 \cos^2\theta_f + \lambda^4 g_r^4 \sin^2\theta_f - 1\right)^3 \lambda^4 g_r^4 \cos^2\theta_f - \lambda^3 V^2 - S = 0, \end{aligned} \tag{6.18}$$

where $\tau = \dfrac{\sqrt{2}t}{R_0\sqrt{\dfrac{\rho}{\mu}}}$ is the dimensionless time, $S = \dfrac{P}{2\Pi\mu R_0 H}$ is the nominal equal-biaxial normalized stress at the boundary, $V = \dfrac{\upsilon}{H\sqrt{\dfrac{\mu}{\epsilon_0\epsilon_r}}} = \sqrt{\dfrac{P_T}{\mu}}$ is the normalized voltage, respectively. The ensuing governing equation elucidates the dynamical behavior of a circular biological membrane undergoing equi-biaxial electro-elastic deformation:

$$\frac{d^2\lambda}{d\tau^2} + g(\lambda; \xi_1, \theta_f, S, V) = 0, \tag{6.19}$$

where

$$\begin{aligned} g(\lambda; \xi_1, \theta_f, S, V) = &\frac{J_m(\lambda^2 g_r^2 - \lambda^{-4} g_z^2)}{J_m - 2\lambda^2 - \frac{1}{\lambda^4} + 3} \\ &+ 2\xi_1 \left(\lambda^2 g_r^2 \cos^2\theta_f + \lambda^2 g_r^2 \sin^2\theta_f - 1\right) \lambda^2 g_r^2 \cos^2\theta_f \\ &+ 8\xi_2 \left(\lambda^4 g_r^4 \cos^2\theta_f + \lambda^4 g_r^4 \sin^2\theta_f - 1\right)^3 \lambda^4 g_r^4 \cos^2\theta_f \\ &- \lambda^3 V^2 - S. \end{aligned}$$

6.4 Snap-through instability and bifurcation criterion for isotropic and anisotropic growth

When radial force (P) and applied voltage (υ) or transverse pressure (P_t) remain constant, the circular biological membrane reaches a state of equilibrium. The equa-

tion governing this equilibrium state is expressed by Eq. 6.19 as follows:

$$g(\lambda; \xi_1, \theta_f, S, V) = 0, \tag{6.20}$$

Several real positive roots exist for the equilibrium stretch λ_{eq}. However, only one or two of these roots hold relevance for the present problem. By utilizing the aforementioned Eq. (6.20), the connection between equilibrium stretch (λ_{eq}) and normalized voltage (V) can be articulated as:

$$\begin{aligned} V = \Bigg\{ \lambda_{eq}^{-3} \Bigg[& \frac{J_m(\lambda_{eq}^2 g_r^2 - \lambda_{eq}^{-4} g_z^2)}{J_m - 2\lambda_{eq}^2 - \lambda_{eq}^{-4} + 3} \\ & + 2\xi_1 \left(\lambda_{eq}^2 g_r^2 \cos^2\theta_f + \lambda_{eq}^2 g_r^2 \sin^2\theta_f - 1\right) \lambda_{eq}^2 g_r^2 \cos^2\theta_f \\ & + 8\xi_2 \left(\lambda_{eq}^4 g_r^4 \cos^2\theta_f + \lambda_{eq}^4 g_r^4 \sin^2\theta_f - 1\right)^3 \lambda_{eq}^4 g_r^4 \cos^2\theta_f - S \Bigg] \Bigg\}^{1/2}. \end{aligned} \tag{6.21}$$

As seen in Fig. 6.1(d), the actuation phenomena appear when an electric field is applied to the biological membrane. However, the durability of electrically activated biological membranes depends critically on the level of pre-strain or normalized static pressure. Figs. 6.3(a) and (b) showcase the membrane response to normalized voltages under a consistent, normalized static pressure. Biological elements like tissue, lipid layers, and red blood cells (RBC) showcase electro-mechanical instability [65, 66]. This phenomenon is often accompanied by strain stiffening in these materials. Notably, bio-inspired sensors have demonstrated snap-through instability under external pressure, as evidenced in the existing findings [96]. This analysis showcases the feasibility of achieving snap-through instability in biological membranes at lower pressures by applying electrical actuation.

In Figs. 6.3(a) and (b), the bifurcation diagram depicts the membrane behavior under constant isotropic growth ($g_r = g_z = 1$) at normalized stresses of 1 and 5, respectively. The crucial parameters under consideration in these instances include $\theta_f = 0^\circ$ and $\xi_1 = \xi_2 = 0$. Based on the observations in Fig. 6.3(a), it may be concluded that snap-through instability occurs by exposing the membrane to a static electric field at a lower static strain. As the normalized voltage gradually rises from zero, the

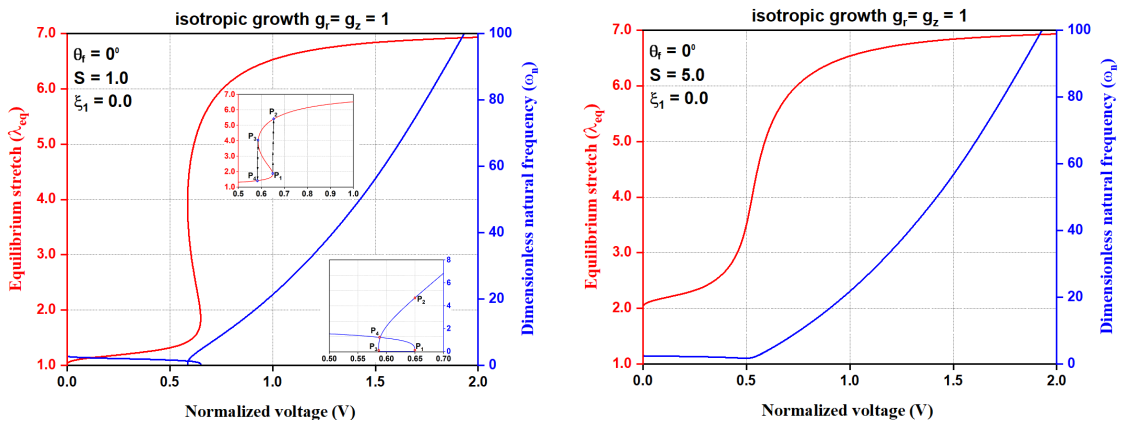


Figure 6.3: Variation of equilibrium stretch (λ_{eq}) and dimensionless natural frequency (ω_n) as a function of normalized voltage (V) for (a) $S = 1$ and (b) $S = 5$.

equilibrium stretch experiences an increment. At the bifurcation point P_1, the curve features a vertical tangent, resulting in a sudden jump in equilibrium stretch from P_1 to a higher value P_2. Beyond this point, the equilibrium stretch increases with the rising voltage. A comparable jump-up occurs reversely during the backward path, moving from P_3 to P_4. The numerical calculation yields bifurcation voltages of $V = 0.649$ and $V = 0.581$, obtained by setting the first derivative of voltage concerning the parameter, $\left(\frac{\partial V}{\partial \lambda}\right)_{\lambda_{eq}} = 0$. The stability of the equilibrium curve branches is verified through the condition that the second derivative of voltage concerning the parameter, $\left(\frac{\partial^2 V}{\partial \lambda^2}\right)_{\lambda_{eq}} > 0$. In Fig. 6.3(a), a stable equilibrium stretch is indicated by the solid line, whereas an unstable one is indicated by the dotted line. The equilibrium curve becomes singular with increased static pressure, eliminating the bi-stable behavior of the membrane. Notably, for a high normalized pressure S = 5 (Fig. 6.3b), the equilibrium curve demonstrates single stability. Electrical actuation becomes prominent at elevated potentials for higher normalized pressure, contributing to the strain-stiffening effect observed in the biological membrane.

The preceding inquiry is centered on the bi-stability phenomenon, characterized by the existence of two potential wells. Additionally, the examination explores the dynamics associated with a double-well oscillation. When subjected to a perturbation

from a static equilibrium stretch λ_{eq}, the temporal evolution of the membrane in the stretch is formulated as follows

$$\lambda(\tau) = \lambda_{eq} + \delta(\tau), \tag{6.22}$$

where $\delta(\tau)$ represents an infinitesimal perturbation. The expression from Eq. (6.22) is introduced into the governing Eq. (6.19) through a first-order Taylor series approximation, yielding

$$\frac{d^2\delta}{d\tau^2} + \delta \left(\frac{\partial g(\lambda; \xi_1, \theta_f, V, S)}{\partial \lambda} \right)_{\lambda=\lambda_{eq}} = 0. \tag{6.23}$$

The dimensionless natural frequency, denoted as ω_n, is derived by employing Eq. (6.23) and expressed as

$$\omega_n^2 = J_m \left[\frac{\left(J_m - 2\lambda_{eq}^2 - \frac{1}{\lambda_{eq}^4} + 3 \right) (2\lambda_{eq} g_r^2 + 4\lambda_{eq}^{-5} g_z^2) - (\lambda_{eq}^2 g_r^2 - \lambda_{eq}^{-4} g_z^2)(4\lambda_{eq}^{-5} - 4\lambda_{eq})}{\left(J_m - 2\lambda_{eq}^2 - \frac{1}{\lambda_{eq}^4} + 3 \right)^2} \right]$$
$$+4\xi_1 \lambda_{eq} g_r^2 \cos^2\theta_f \left(2\lambda_{eq}^2 g_r^2 \cos^2\theta_f + 2\lambda_{eq}^2 g_r^2 \sin^2\theta_f - 1 \right) - 3\lambda_{eq}^2 V^2. \tag{6.24}$$

Eqs. (6.19), (6.23), and (6.24) are subsequently employed to ascertain the correlation between the natural frequency of oscillation and the normalized voltage. This relationship is graphically depicted in Figs. 6.3(a-b) for $S = 1$ and $S = 5$, respectively. The analysis is conducted when the system experiences a slight perturbation from its equilibrium state. In Fig. 6.3(a), three equilibrium stretches are depicted, corresponding to a specified voltage within the range delineated by the bifurcation points. Each equilibrium stretch is found to correspond with a certain natural frequency, whereas the unstable equilibrium stretch lacks the natural frequency. As shown in Fig. 6.3(a), this phenomenon may be explained by the existence of two natural frequencies when three equilibrium points coincide. The transition from P_1 to P_2 in the inset of Fig. 6.3(a) triggers a subsequent reverse transition from P_3 to P_4, owing to the strong dependence of the linearized natural frequency on λ_{eq}. Consequently, each voltage value corresponds to a singular natural frequency, exemplified in Fig. 6.3(b), where the curve exhibits a monotonically increasing trend.

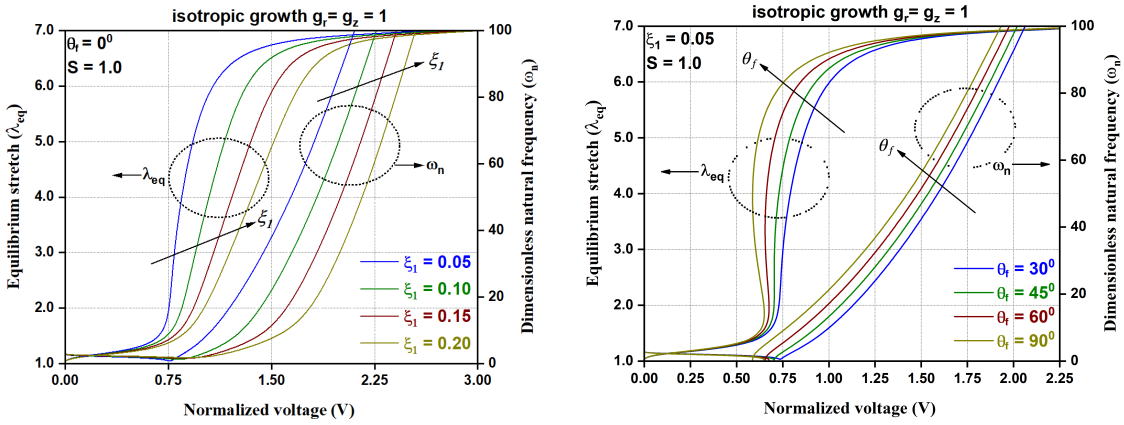
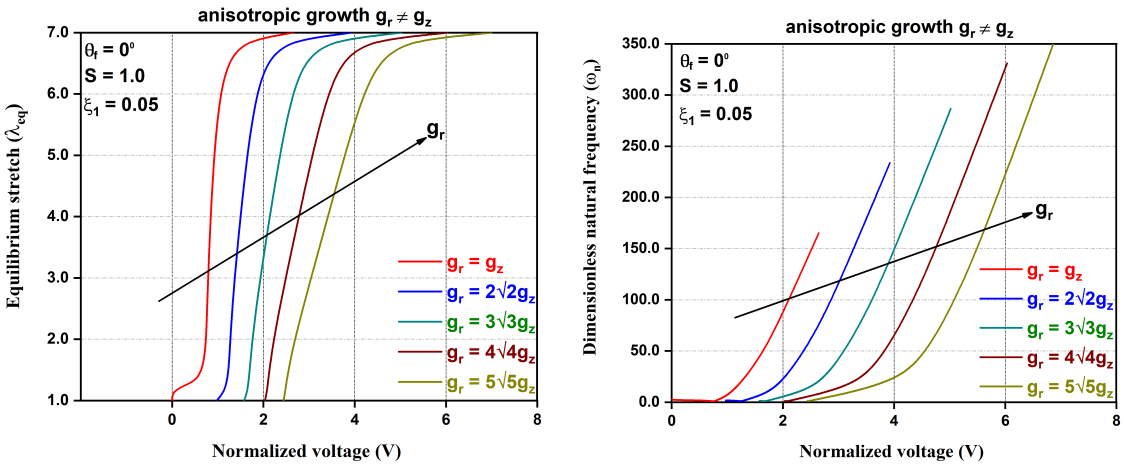


Figure 6.4: Variation of equilibrium stretch (λ_{eq}) and dimensionless natural frequency (ω_n) as a function of normalized voltage (V) for different (a) levels of the anisotropy parameter (ξ_1) and (b) fiber orientation angle (θ_f) for isotropic growth ($g_r = g_z = 1$).

Next, we evaluate the effect of the anisotropy parameter ξ_1 (see Fig. 6.4a) and the fiber orientation angle θ_f (see Fig. 6.4b) on the correlation between the normalized voltage, the equilibrium stretch, and the natural frequency of oscillation. The crucial parameters under consideration in these instances include the constant isotropic growth ($g_r = g_z = 1$) at a normalized stress of 1. Specifically, in Case 1 (Fig. 6.4a), to showcase the effect of anisotropy, we consider four different values of $\xi_1 = 0.05$, 0.10, 0.15 and 0.20 [19] with $\theta_f = 0°$. In Case 2 (Fig. 6.4b), to examine the impact of fiber orientation, we consider the values of $\theta_f = 30°, 45°, 60°$, and $90°$ with $\xi_1 = 0.05$. Notably, in the context of a high anisotropy parameter ($\xi_1 > 0.05$, as illustrated in Fig. 6.4a), the equilibrium curve manifests a distinctive single stability. This observation implies that as membrane anisotropy increases, the equilibrium curve transforms, leading to the elimination of the bi-stable behavior of the membrane. In essence, the enhanced anisotropy unifies stability states, resulting in a singular equilibrium configuration. The response of the natural frequency mirrors that of the equilibrium curve, thereby establishing a direct correspondence between each voltage value and a unique natural frequency in instances characterized by a high anisotropy parameter ($\xi_1 > 0.05$). This relationship is exemplified in Fig. 6.4(a), where the curve shows a



(a) (b)

Figure 6.5: Variation of (a) equilibrium stretch (λ_{eq}) and (b) dimensionless natural frequency (ω_n) as a function of normalized voltage (V) for different levels of anisotropic growth.

monotonically increasing trend for higher values of ξ_1, indicating a one-to-one mapping between voltage values and singular natural frequencies. In Case 2 (Fig. 6.4b), it is observed that the membrane exhibits bi-stable behavior for all the considered degrees of fiber orientation. It is also observed that the normalized voltage required to initiate snap-through instability decreases with the increase in fiber orientation angle. The same trends are observed for the natural frequency of the membrane. The required level of normalized voltage for attaining the natural oscillation frequency decreases with the increase in fiber orientation angle. This implies that fiber orientation significantly governs the normalized voltage required for attaining the natural frequency of oscillations of the membrane.

Finally, we evaluate the effect of anisotropic growth of the membrane ($g_r \neq g_z$) on the correlation between the normalized voltage and the equilibrium stretch (see Fig. 6.5a) and natural frequency of oscillation (see Fig. 6.5b). To analyze these, we consider five different values as $g_r = g_z, 2\sqrt{2}g_z, 3\sqrt{3}g_z, 4\sqrt{4}g_z$ and $5\sqrt{5}g_z$. The other parameters under consideration in these instances include $\theta_f = 0^\circ$, $\xi_1 = 0.05$ and $S = 1$. In the specific cases of anisotropic growth (denoted by $g_r \neq g_z$, as depicted in Fig. 6.5a), the equilibrium curve exhibits a unique type of singular stability. Essentially, the intensified anisotropic growth consolidates stability states, yielding a single equilibrium

configuration. Additionally, it is noted that the normalized voltage needed to initiate snap-through instability rises with the augmentation of membrane anisotropic growth. The natural frequency response is the same as that of the equilibrium curve (see Fig. 6.5b), thereby establishing a direct correspondence between each voltage value and a unique natural frequency. This relationship is exemplified in Fig. 6.5(b), where the curve showcases a monotonically increasing trend for all the considered levels of membrane anisotropic growth, indicating a one-to-one mapping between voltage values and singular natural frequencies. Moreover, the natural frequency of oscillation of the membrane, along with the normalized voltage, increases with the enhancement in the anisotropic growth of the membrane. This indicates that the anisotropic growth of the membrane significantly governs the required normalized voltage and natural frequency of oscillations of the membrane.

The obtained results agree well with the physical behavior reported in the literature on electroactive biological membranes. Increasing the growth parameters enhances membrane deformation and promotes snap-through instability due to growth-induced softening effects. In contrast, fiber reinforcement and material anisotropy improve membrane stiffness and influence the bifurcation response, resulting in better stability under electric loading. The predicted deformation and instability behavior are also consistent with previously reported theoretical and experimental studies, confirming the reliability of the present model.

6.5 Limitations of the biological membrane model

This chapter uses a simplified model to study how electric loading, growth, and fiber orientation affect a biological or bio-inspired membrane. The membrane is treated as thin, uniform, incompressible, and hyperelastic, with axisymmetric deformation. These assumptions make the main mechanical effects easier to examine, although real tissues are generally more complex.

The applied electric field is represented by an equivalent pressure. This captures its mechanical effect within the model, but it does not include biological processes such as

ion transport or active cellular responses. The Gent model describes nonlinear elastic behavior, while effects such as viscoelastic relaxation, fluid transport, damage, and active contraction are not included. The model also assumes a single fiber orientation, whereas fiber directions can vary within a tissue.

The condition $g_r^2 g_z = 1$ means that growth preserves local volume in this analysis. It is therefore used to represent changes in the direction of growth, rather than growth caused by the addition of mass. Biological growth that changes local volume would require a different growth formulation.

The results show how the selected model responds when its parameters change. To predict the behavior of a specific tissue, its geometry and material properties would need to be measured, and the model would need to be checked against experiments.

6.6 Summary

This chapter provides a modeling framework based on continuum physics to investigate the complex nonlinear dynamics of a biological circular membrane with different models of the membrane's anisotropy parameter, anisotropic growth, and fiber orientation under electro-mechanical loadings. The conventional method of exerting transverse pressure on the membrane is replaced with a comparable electric field to enable a qualitative analysis of this biological system. The analysis focuses on the nonlinear differential equation governing the axisymmetric radial motion of a circular biological membrane. The present study enhances our understanding of the overall behavior of the membrane system when it is subjected to changes in the membrane's anisotropy parameter, anisotropic growth, and fiber orientation. The following are the salient inferences drawn from the present analysis:

i. A bifurcation diagram, which plots the effects of changing normalized voltage while keeping the normalized static pressure constant, shows that under specific applied stress conditions, the biological membrane displays bi-stability. When the normalized pressure rises and the equilibrium curve displays a single value or single stability, the bi-stability disappears.

ii. It is observed that the bi-stable characteristics vanish with an increase in the anisotropy parameter, whereas there is no change with an increase in fiber orientation angle.

iii. It is observed that the normalized voltage required for the initiation of snap-through instability decreases with the increase in fiber orientation angle, but increases with increasing anisotropic growth of the membrane.

This chapter examined the deformation and stability behavior of electroactive membranes considering isotropic and anisotropic growth together with fiber reinforcement. The results showed that increasing the growth parameter increased membrane deformation and promoted snap-through instability at higher electric loading. In contrast, fiber reinforcement and material anisotropy enhanced membrane stiffness and improved stability behavior. The study also showed that fiber orientation significantly affects the bifurcation response and overall membrane deformation under electric loading.

The next chapter presents the overall conclusions of the thesis by summarizing the major findings related to the deformation, dynamic response, stability, and instability behavior of electro-magneto-active and biological membranes. It also highlights the key contributions of the present work and discusses possible directions for future research in smart soft material systems.

Chapter 7

Conclusion and Future Scope

Preface

This chapter summarizes the major findings and contributions of the thesis. It highlights the significance of the proposed continuum models in understanding the nonlinear dynamics and stability of electro-magneto-active membranes and discusses possible directions for future research.

7.1 Conclusion

This thesis contributes to the understanding of how circular active membranes respond to mechanical, electric and magnetic loading. The work examines four related aspects of their behavior: particle reinforcement, stretch-dependent electromagnetic properties, taut domain formation, and the effects of growth and fiber orientation. Together, these studies show how material properties and applied fields influence membrane deformation, oscillation and stability.

The first part of the thesis investigates the dynamics of particle-reinforced electro-magneto-active circular membranes. Increasing the filler volume fraction and the filler-to-matrix shear modulus ratio reduces the oscillation amplitude for the parameters considered. A higher applied voltage increases the deformation response, whereas higher magnetic loading reduces the oscillation amplitude. Under AC excitation, changes in voltage and filler content also produce more complex, aperiodic responses in

the investigated cases. These findings show that reinforcement offers a way to control the membrane's dynamic response.

The second part examines how stretch-dependent electric permittivity and magnetic permeability affect membrane dynamics. At low actuation levels, the constant, linear and nonlinear property models predict similar responses. Their differences become more noticeable at higher loading, particularly in the oscillation amplitude and frequency response. This indicates that changes in electromagnetic properties with deformation should be considered when predicting the response of a highly actuated membrane.

The third part focuses on taut domain formation in particle-reinforced membranes. Increasing electric loading contracts the taut domain and eventually leads to a critical condition at which the equilibrium solutions merge. In contrast, increasing magnetic loading expands the taut domain for the parameters investigated. Higher filler volume fraction and filler-to-matrix shear modulus ratio also enlarge the taut region and increase the critical normalized voltage. These results show how reinforcement and electromagnetic loading can change the range of attainable taut configurations.

The final part extends the analysis to electrically active membranes with growth and fiber reinforcement. Applied stress, material anisotropy, fiber orientation and anisotropic growth all influence the equilibrium response and natural frequency. In the cases examined, increasing the anisotropy parameter removes bistability, while changing fiber orientation alters the voltage required for snap-through. The anisotropic growth cases show an increase in the voltage associated with instability as directional growth increases. This study provides insight into the separate roles of growth and fiber direction in membrane stability.

Taken together, the results provide a theoretical basis for examining the dynamics and stability of reinforced soft active membranes. The present study is primarily theoretical and numerical, and the conclusions are drawn from idealized continuum models. Comprehensive experimental validation has not been performed for all the considered loading conditions. Therefore, experimental measurements and material-specific calibration are needed to assess the quantitative predictions for individual

actuators or biological tissues.

7.2 Future scope

The present study opens several promising directions for further research:

- Conducting controlled experiments to measure deformation-dependent permittivity and permeability in reinforced elastomers would help validate the theoretical framework and improve model reliability.

- Extending the current hyperelastic formulation to include viscoelasticity and rate-dependent behavior would allow a more realistic description of dynamic response, especially under cyclic or long-term loading.

- Future models may incorporate thermal effects and other coupled phenomena, enabling the study of thermo-electro-magneto-mechanical interactions relevant to high-field applications.

- Expanding the analysis beyond circular membranes to shells, multilayer systems, and fully three-dimensional configurations would enhance applicability to soft robotic components and adaptive structures.

- The growth and anisotropy framework developed here can be further extended to study morphogenesis, tissue growth, and stability phenomena in biological membranes.

Appendix A

A.1 AC dynamic response

The governing Eqs. (4.21) for varying electric permittivity models under the applied AC voltage (Eq. (4.30)) may be rearticulated as:

$$\left[\begin{array}{ll}
\left\{\begin{array}{l}\dfrac{d^2\lambda}{d\tau^2}+\dfrac{J_m(\lambda-\lambda^{-5})}{J_m-2\lambda^2-\lambda^{-4}+3}-\lambda^3\left[V_a\sin(\omega\tau)\right]^2 \\ \qquad +\lambda^{-5}M^2-S=0\end{array}\right\} & \text{Constant} \\
\left\{\begin{array}{l}\dfrac{d^2\lambda}{d\tau^2}+\dfrac{J_m(\lambda-\lambda^{-5})}{J_m-2\lambda^2-\lambda^{-4}+3} \\ \qquad -(1.106\lambda^3-0.106\lambda^4)\left[V_a\sin(\omega\tau)\right]^2+\lambda^{-5}M^2-S=0\end{array}\right\} & \text{Linear} \\
\left\{\begin{array}{l}\dfrac{d^2\lambda}{d\tau^2}+\dfrac{J_m(\lambda-\lambda^{-5})}{J_m-2\lambda^2-\lambda^{-4}+3} \\ \qquad -(\lambda^3-0.01748\lambda^5+0.01768\lambda^{-1})\left[V_a\sin(\omega\tau)\right]^2 \\ \qquad +\lambda^{-5}M^2-S=0\end{array}\right\} & \text{Nonlinear}
\end{array}\right]. \tag{A.1}$$

In the above equation, the dimensionless excitation frequency, denoted by ω, is defined as: $\omega = \frac{1}{2}\omega_0 R_0\sqrt{\frac{\varepsilon}{\mu}}$. Likewise, the governing Eqs. (4.26) for varying magnetic

permeability models under the applied AC voltage (Eq. (4.30)) are rewritten as:

$$\left[\begin{array}{ll} \left\{\begin{array}{l} \dfrac{d^2\lambda}{d\tau^2} + \dfrac{J_m(\lambda-\lambda^{-5})}{J_m-2\lambda^2-\lambda^{-4}+3} - \lambda^3[V_a\sin(\omega\tau)]^2 \\ \qquad + \lambda^{-5}M^2 - S = 0 \end{array}\right\} & \text{Constant} \\ \left\{\begin{array}{l} \dfrac{d^2\lambda}{d\tau^2} + \dfrac{J_m(\lambda-\lambda^{-5})}{J_m-2\lambda^2-\lambda^{-4}+3} - \lambda^3[V_a\sin(\omega\tau)]^2 \\ \qquad + (1.106\lambda^{-5}-0.106\lambda^{-4})M^2 - S = 0 \end{array}\right\} & \text{Linear} \\ \left\{\begin{array}{l} \dfrac{d^2\lambda}{d\tau^2} + \dfrac{J_m(\lambda-\lambda^{-5})}{J_m-2\lambda^2-\lambda^{-4}+3} - \lambda^3[V_a\sin(\omega\tau)]^2 \\ \qquad + (\lambda^{-5}-0.01748\lambda^{-3}+0.01768\lambda^{-9})M^2 - S = 0 \end{array}\right\} & \text{Nonlinear} \end{array}\right]. \quad \text{(A.2)}$$

References

[1] A. Khurana, D. Kumar, A. K. Sharma, G. Zurlo, and M. Joglekar, "Taut domains in transversely isotropic electro-magneto-active thin membranes," *International Journal of Non-Linear Mechanics*, vol. 147, p. 104228, 2022.

[2] R. Bustamante, A. Dorfmann, and R. W. Ogden, "On electric body forces and maxwell stresses in nonlinearly electroelastic solids," *International Journal of Engineering Science*, vol. 47, no. 11-12, pp. 1131–1141, 2009.

[3] L. Dorfmann and R. W. Ogden, "Instabilities of an electroelastic plate," *International Journal of Engineering Science*, vol. 77, pp. 79–101, 2014.

[4] G. Zurlo, M. Destrade, and T. Lu, "Fine tuning the electro-mechanical response of dielectric elastomers," *Applied physics letters*, vol. 113, no. 16, 2018.

[5] A. Alibakhshi and H. Heidari, "Nonlinear dynamics of dielectric elastomer balloons based on the gent-gent hyperelastic model," *European Journal of Mechanics-A/Solids*, vol. 82, p. 103986, 2020.

[6] C. O. Horgan and G. Saccomandi, "A molecular-statistical basis for the gent constitutive model of rubber elasticity," *Journal of Elasticity*, vol. 68, no. 1, pp. 167–176, 2002.

[7] A. Khurana, M. M. Joglekar, and G. Zurlo, "Electromechanical stability of wrinkled dielectric elastomers," *International Journal of Solids and Structures*, p. 111613, 2022.

[8] G. Puglisi and G. Saccomandi, "Multi-scale modelling of rubber-like materials and soft tissues: an appraisal," *Proceedings of the Royal Society A: Mathematical, Physical and Engineering Sciences*, vol. 472, no. 2187, p. 20160060, 2016.

[9] Y. Nakabo, T. Mukai, and K. Asaka, "Biomimetic soft robots using IPMC," in *Electroactive Polymers for Robotic Applications: Artificial Muscles and Sensors*, K. J. Kim and S. Tadokoro, Eds. London: Springer, 2007, pp. 165–198.

[10] A. Kumar, A. Khurana, A. K. Patra, Y. Agrawal, and M. Joglekar, "Electromechanical performance of dielectric elastomer composites: Modeling and experimental characterization," *Composite Structures*, vol. 320, p. 117130, 2023.

[11] A. Alibakhshi and H. Heidari, "Analytical approximation solutions of a dielectric elastomer balloon using the multiple scales method," *European Journal of Mechanics-A/Solids*, vol. 74, pp. 485–496, 2019.

[12] A. K. Bastola and M. Hossain, "A review on magneto-mechanical characterizations of magnetorheological elastomers," *Composites Part B: Engineering*, vol. 200, p. 108348, 2020.

[13] P. Saxena, M. Hossain, and P. Steinmann, "A theory of finite deformation magneto-viscoelasticity," *International Journal of Solids and Structures*, vol. 50, no. 24, pp. 3886–3897, 2013.

[14] M. Hossain, P. Saxena, and P. Steinmann, "Modelling the curing process in magneto-sensitive polymers: rate-dependence and shrinkage," *International Journal of Non-Linear Mechanics*, vol. 74, pp. 108–121, 2015.

[15] C. Cao, X. Gao, and A. T. Conn, "A magnetically coupled dielectric elastomer pump for soft robotics," *Advanced Materials Technologies*, vol. 4, no. 8, p. 1900128, 2019.

[16] A. K. Patra, A. Khurana, D. Kumar, and P. Saxena, "Impact of compliant electrodes on the dynamics of electromagnetoactive membranes," *International Journal of Non-Linear Mechanics*, vol. 167, p. 104906, 2024.

[17] E. Yarali, M. Baniasadi, A. Zolfagharian, M. Chavoshi, F. Arefi, M. Hossain, A. Bastola, M. Ansari, A. Foyouzat, A. Dabbagh *et al.*, "Magneto-/electro-responsive polymers toward manufacturing, characterization, and biomedical/soft robotic applications," *Applied Materials Today*, vol. 26, p. 101306, 2022.

[18] C. O. Horgan and G. Saccomandi, "A new constitutive theory for fiber-reinforced incompressible nonlinearly elastic solids," *Journal of the Mechanics and Physics of Solids*, vol. 53, no. 9, pp. 1985–2015, 2005.

[19] S. Gour, D. Kumar, and V. Yadav, "Constitutive modeling for the tear fracture of rubber with filler particles," *Sādhanā*, vol. 47, no. 2, pp. 1–9, 2022.

[20] T. Mori and K. Tanaka, "Average stress in matrix and average elastic energy of materials with misfitting inclusions," *Acta metallurgica*, vol. 21, no. 5, pp. 571–574, 1973.

[21] Y. Long and R. A. Shanks, "Pp–elastomer–filler hybrids. i. processing, microstructure, and mechanical properties," *Journal of Applied Polymer Science*, vol. 61, no. 11, pp. 1877–1885, 1996.

[22] M. Sangerano, E. Pallaro, I. Roppolo, and G. Rizza, "Uv-cured epoxy coating reinforced with sepiolite as inorganic filler," *Journal of materials science*, vol. 44, no. 12, pp. 3165–3171, 2009.

[23] A. Alibakhshi, A. Imam, and S. E. Haghighi, "Effect of the second invariant of the cauchy–green deformation tensor on the local dynamics of dielectric elastomers," *International Journal of Non-Linear Mechanics*, vol. 137, p. 103807, 2021.

[24] A. Khurana, D. Kumar, A. K. Sharma, and M. Joglekar, "Static and dynamic instability modeling of electro-magneto-active polymers with various entanglements and crosslinks," *International Journal of Non-Linear Mechanics*, vol. 139, p. 103865, 2022.

[25] H. Heidari, A. Alibakhshi, and H. R. Azarboni, "Chaotic motion of a parametrically excited dielectric elastomer," *International Journal of Applied Mechanics*, vol. 12, no. 03, p. 2050033, 2020.

[26] S. K. Behera, R. A. Ranjan, D. Kumar, S. Sarangi, and R. Bhattacharyya, "Dynamic modelling and analysis of a biological circular membrane," *International Journal of Engineering Science*, vol. 188, p. 103864, 2023.

[27] A. Agrawal, A. Khurana, and D. Kumar, "Dynamics of an electric field vulnerable morpho-elastic biological membranes," *Journal of Applied Mechanics*, pp. 1–20, 2025.

[28] R. M. Soares, P. F. Amaral, F. M. Silva, and P. B. Gonçalves, "Nonlinear breathing motions and instabilities of a pressure-loaded spherical hyperelastic membrane," *Nonlinear Dynamics*, vol. 99, pp. 351–372, 2020.

[29] S. Son and N. Goulbourne, "Dynamic response of tubular dielectric elastomer transducers," *International Journal of Solids and Structures*, vol. 47, no. 20, pp. 2672–2679, 2010.

[30] J. Fox and N. Goulbourne, "On the dynamic electromechanical loading of dielectric elastomer membranes," *Journal of the Mechanics and Physics of Solids*, vol. 56, no. 8, pp. 2669–2686, 2008.

[31] E. M. Mockensturm and N. Goulbourne, "Dynamic response of dielectric elastomers," *International Journal of Non-Linear Mechanics*, vol. 41, no. 3, pp. 388–395, 2006.

[32] M. Wissler and E. Mazza, "Electromechanical coupling in dielectric elastomer actuators," *Sensors and Actuators A: Physical*, vol. 138, no. 2, pp. 384–393, 2007.

[33] X. Zhao and Z. Suo, "Method to analyze electromechanical stability of dielectric elastomers," *Applied Physics Letters*, vol. 91, no. 6, 2007.

[34] A. Dorfmann and R. Ogden, "Nonlinear magnetoelastic deformations," *Quarterly Journal of Mechanics and Applied Mathematics*, vol. 57, no. 4, pp. 599–622, 2004.

[35] R. Bustamante, A. Dorfmann, and R. Ogden, "Universal relations in isotropic nonlinear magnetoelasticity," *The Quarterly Journal of Mechanics & Applied Mathematics*, vol. 59, no. 3, pp. 435–450, 2006.

[36] A. Dorfmann and R. Ogden, "Nonlinear electroelasticity," *Acta Mechanica*, vol. 174, no. 3-4, pp. 167–183, 2005.

[37] X. Zhao and Z. Suo, "Electrostriction in elastic dielectrics undergoing large deformation," *Journal of Applied Physics*, vol. 104, no. 12, 2008.

[38] S. M. Jiménez and R. M. McMeeking, "Deformation dependent dielectric permittivity and its effect on actuator performance and stability," *International Journal of Non-Linear Mechanics*, vol. 57, pp. 183–191, 2013.

[39] A. K. Srivastava and S. Basu, "Modelling the performance of devices based on thin dielectric elastomer membranes," *Mechanics of Materials*, vol. 137, p. 103136, 2019.

[40] R. Moucka, M. Sedlacik, and M. Cvek, "Dielectric properties of magnetorheological elastomers with different microstructure," *Applied Physics Letters*, vol. 112, no. 12, 2018.

[41] D. Isaev, A. Semisalova, Y. Alekhina, L. Makarova, and N. Perov, "Simulation of magnetodielectric effect in magnetorheological elastomers," *International Journal of Molecular Sciences*, vol. 20, no. 6, p. 1457, 2019.

[42] A. A. Snarskii, M. Shamonin, and P. Yuskevich, "Effect of magnetic-field-induced restructuring on the elastic properties of magnetoactive elastomers," *Journal of Magnetism and Magnetic Materials*, vol. 517, p. 167392, 2021.

[43] D. De Tommasi, G. Puglisi, and G. Zurlo, "Compression-induced failure of electroactive polymeric thin films," *Applied Physics Letters*, vol. 98, no. 12, 2011.

[44] ——, "Taut states of dielectric elastomer membranes," *International Journal of Non-Linear Mechanics*, vol. 47, no. 2, pp. 355–361, 2012.

[45] S. Gour, D. Kumar, and A. Khurana, "Unequal-biaxial taut states of functionally graded dielectric elastomers," *International Journal of Engineering Science*, vol. 214, p. 104291, 2025.

[46] A. S. Gangwar, A. Khurana, and A. K. Sharma, "Wrinkling stability in soft dielectric elastomers: The role of strain stiffening and stretch-dependent permittivity," *International Journal of Solids and Structures*, p. 113429, 2025.

[47] A. Khurana, G. Zurlo, and M. Joglekar, "Taut domain analysis of transversely isotropic dielectric elastomer membranes," in *ECCOMAS congress*, 2022.

[48] D. De Tommasi, G. Puglisi, and G. Zurlo, "Hysteresis in electroactive polymers," *European Journal of Mechanics-A/Solids*, vol. 48, pp. 16–22, 2014.

[49] A. Khurana, A. Kumar, S. K. Raut, A. K. Sharma, and M. Joglekar, "Effect of viscoelasticity on the nonlinear dynamic behavior of dielectric elastomer minimum energy structures," *International Journal of Solids and Structures*, vol. 208, pp. 141–153, 2021.

[50] A. Kumar, A. Khurana, A. K. Sharma, and M. Joglekar, "Dynamics of pneumatically coupled visco-hyperelastic dielectric elastomer actuators: Theoretical modeling and experimental investigation," *European Journal of Mechanics-A/Solids*, vol. 95, p. 104636, 2022.

[51] J. Zhang, H. Chen, and D. Li, "Pinnacle elimination and stability analyses in nonlinear oscillation of soft dielectric elastomer slide actuators," *Nonlinear Dynamics*, vol. 94, no. 3, pp. 1907–1920, 2018.

[52] S. Rudykh, K. Bhattacharya, and G. Debotton, "Snap-through actuation of thick-wall electroactive balloons," *International Journal of Non-Linear Mechanics*, vol. 47, no. 2, pp. 206–209, 2012.

[53] M. Eskandari and E. Kuhl, "Systems biology and mechanics of growth," *Wiley Interdisciplinary Reviews: Systems Biology and Medicine*, vol. 7, no. 6, pp. 401–412, 2015.

[54] A. Goriely, *The mathematics and mechanics of biological growth*. Springer, 2017, vol. 45.

[55] M. K. Rausch and E. Kuhl, "On the mechanics of growing thin biological membranes," *Journal of the Mechanics and Physics of Solids*, vol. 63, pp. 128–140, 2014.

[56] D. Khalipina, Y. Kaga, N. Dacher, and N. R. Chevalier, "Smooth muscle contractility causes the gut to grow anisotropically," *Journal of the Royal Society Interface*, vol. 16, no. 159, p. 20190484, 2019.

[57] V. Balbi and P. Ciarletta, "Morpho-elasticity of intestinal villi," *Journal of the Royal Society Interface*, vol. 10, no. 82, p. 20130109, 2013.

[58] J. F. Durel and N. L. Nerurkar, "Mechanobiology of vertebrate gut morphogenesis," *Current opinion in genetics & development*, vol. 63, pp. 45–52, 2020.

[59] J. Ackermann, P. J. Cohen, K. Alessandri, A. Leonard, P. Nassoy, J.-F. Joanny, and M. B. Amar, "Morpho-elasticity of human pluripotent stem cell cysts," *Journal of the Mechanics and Physics of Solids*, vol. 160, p. 104778, 2022.

[60] Y.-P. Chen, Y. Shao, P.-C. Chen, K. Li, J.-Y. Li, J. Meng, C.-L. Lv, H.-Y. Liu, C. Lv, X.-Q. Feng *et al.*, "Substrate nesting guides cyst morphogenesis of human pluripotent stem cells without 3d extracellular matrix overlay," *Acta Biomaterialia*, vol. 170, pp. 519–531, 2023.

[61] J. Kirk, "A theoretical analysis of the contribution of algal cells to the attenuation of light within natural waters i. general treatment of suspensions of pigmented cells," *New phytologist*, vol. 75, no. 1, pp. 11–20, 1975.

[62] O. Alvarez and R. Latorre, "Voltage-dependent capacitance in lipid bilayers made from monolayers," *Biophysical journal*, vol. 21, no. 1, pp. 1–17, 1978.

[63] F. Blatt, "Elastic energy stored in a membrane due to electrostriction," *Journal of Biological Physics*, vol. 10, no. 4, pp. 219–222, 1982.

[64] T. Heimburg, "The capacitance and electromechanical coupling of lipid membranes close to transitions: the effect of electrostriction," *Biophysical journal*, vol. 103, no. 5, pp. 918–929, 2012.

[65] J. Akinlaja and F. Sachs, "The breakdown of cell membranes by electrical and mechanical stress," *Biophysical journal*, vol. 75, no. 1, pp. 247–254, 1998.

[66] U. Zimmermann, G. Pilwat, and F. Riemann, "Dielectric breakdown of cell membranes," *Biophysical journal*, vol. 14, no. 11, pp. 881–899, 1974.

[67] H. Li, L. Chen, C. Zhao, and S. Yang, "Evoking or suppressing electromechanical instabilities in soft dielectrics with deformation-dependent dielectric permittivity," *International Journal of Mechanical Sciences*, vol. 202, p. 106507, 2021.

[68] A. Khurana, D. Kumar, A. K. Sharma, and M. M. Joglekar, "Nonlinear oscillations of particle-reinforced electro-magneto-viscoelastomer actuators," *Journal of Applied Mechanics*, vol. 88, no. 12, 2021.

[69] D. Kumar and S. Sarangi, "Electro-magnetostriction under large deformation: modeling with experimental validation," *Mechanics of Materials*, vol. 128, pp. 1–10, 2019.

[70] A. K. Patra, A. Khurana, and D. Kumar, "Modeling and analysis of a thermo-electro-magneto-viscoelastic actuator," *International Journal of Applied Mechanics*, vol. 16, no. 02, p. 2450015, 2024.

[71] C. O. Horgan, "The remarkable gent constitutive model for hyperelastic materials," *International Journal of Non-Linear Mechanics*, vol. 68, pp. 9–16, 2015.

[72] D. Kumar, S. Sarangi, and R. Bhattacharyya, "Universal relations in nonlinear electro-magneto-elasticity," *Archive of Applied Mechanics*, vol. 90, pp. 1643–1657, 2020.

[73] R. E. Pelrine, R. D. Kornbluh, and J. P. Joseph, "Electrostriction of polymer dielectrics with compliant electrodes as a means of actuation," *Sensors and Actuators A: Physical*, vol. 64, no. 1, pp. 77–85, 1998.

[74] A. Kumar, A. Khurana, A. K. Sharma, and M. Joglekar, "Dynamic analysis of anisotropic dielectric viscoelastomers incorporating humidity effect," *Journal of the Brazilian Society of Mechanical Sciences and Engineering*, vol. 44, no. 8, p. 348, 2022.

[75] J. Zhang, H. Chen, and D. Li, "Method to control dynamic snap-through instability of dielectric elastomers," *Physical Review Applied*, vol. 6, no. 6, p. 064012, 2016.

[76] H. Vatandoost, R. Sedaghati, and S. Rakheja, "A novel methodology for accurate estimation of magnetic permeability of magnetorheological elastomers," *Journal of Magnetism and Magnetic Materials*, vol. 560, p. 169669, 2022.

[77] A. K. Pandey, A. Khurana, and A. K. Sharma, "Thermo-electro-mechanical effects on nonlinear dynamics of smart dielectric elastomer minimum energy structures," *European Journal of Mechanics-A/Solids*, vol. 105, p. 105222, 2024.

[78] H. Vatanjou, Y. Hojjat, and M. Karafi, "Nonlinear dynamic analysis of dielectric elastomer minimum energy structures," *Applied Physics A*, vol. 125, pp. 1–11, 2019.

[79] B.-X. Xu, R. Mueller, A. Theis, M. Klassen, and D. Gross, "Dynamic analysis of dielectric elastomer actuators," *Applied Physics Letters*, vol. 100, no. 11, 2012.

[80] J. Zhang, H. Chen, B. Li, D. McCoul, and Q. Pei, "Coupled nonlinear oscillation and stability evolution of viscoelastic dielectric elastomers," *Soft Matter*, vol. 11, no. 38, pp. 7483–7493, 2015.

[81] J. Zhang, L. Tang, B. Li, Y. Wang, and H. Chen, "Modeling of the dynamic characteristic of viscoelastic dielectric elastomer actuators subject to different conditions of mechanical load," *Journal of Applied Physics*, vol. 117, no. 8, 2015.

[82] A. Agrawal and A. Khurana, "Unveiling the dynamics of particle-reinforced electro-magneto-active circular membrane," *International Journal of Non-Linear Mechanics*, p. 105064, 2025.

[83] D. Steigmann and A. Pipkin, "Finite deformations of wrinkled membranes," *The Quarterly Journal of Mechanics and Applied Mathematics*, vol. 42, no. 3, pp. 427–440, 1989.

[84] B. Li, H. Chen, and J. Zhou, "Electromechanical stability of dielectric elastomer composites with enhanced permittivity," *Composites Part A: Applied Science and Manufacturing*, vol. 52, pp. 55–61, 2013.

[85] R. Díaz-Calleja, E. Riande, and M. Sanchis, "On electromechanical stability of dielectric elastomers," *Applied Physics Letters*, vol. 93, no. 10, 2008.

[86] J. Blok and D. LeGrand, "Dielectric breakdown of polymer films," *Journal of Applied Physics*, vol. 40, no. 1, pp. 288–293, 1969.

[87] R. Pelrine, R. Kornbluh, Q. Pei, and J. Joseph, "High-speed electrically actuated elastomers with strain greater than 100%," *Science*, vol. 287, no. 5454, pp. 836–839, 2000.

[88] X. Zhao and Z. Suo, "Electromechanical instability in semicrystalline polymers," *Applied physics letters*, vol. 95, no. 3, 2009.

[89] E. K. Rodriguez, A. Hoger, and A. D. McCulloch, "Stress-dependent finite growth in soft elastic tissues," *Journal of biomechanics*, vol. 27, no. 4, pp. 455–467, 1994.

[90] L. D. Mosgaard, K. A. Zecchi, and T. Heimburg, "Mechano-capacitive properties of polarized membranes," *Soft Matter*, vol. 11, no. 40, pp. 7899–7910, 2015.

[91] R. W. Ogden, *Non-linear elastic deformations*. Courier Corporation, 1997.

[92] D. Kumar, S. Ghosh, S. Roy, and S. Santapuri, "Modeling and analysis of an electro-pneumatic braided muscle actuator," *Journal of Intelligent Material Systems and Structures*, vol. 32, no. 4, pp. 399–409, 2021.

[93] K. Arya, D. Kumar, and S. Sarangi, "Free radial oscillations of an actuated cylindrical tube," *Mechanics of Advanced Materials and Structures*, pp. 1–11, 2022.

[94] Z.-B. Kuang, *Theory of electroelasticity*. Springer, 2014.

[95] D. Kumar, S. K. Behera, K. Arya, and S. Sarangi, "An alternative form of energy density function demonstrating the electro-elastic deformation of a dielectric cylindrical actuator," *Mechanics of Soft Materials*, vol. 4, no. 1, p. 3, 2022.

[96] H. Li, Y. Zheng, Y. L. Han, S. Cai, and M. Guo, "Nonlinear elasticity of biological basement membrane revealed by rapid inflation and deflation," *Proceedings of the National Academy of Sciences*, vol. 118, no. 11, p. e2022422118, 2021.